Novel Nano/Micro-materials for Visible-light-driven Photocatalysis: Syntheses, Characterizations and Applications

ZHANG, Lisha

A Thesis Submitted in Partial Fulfillment

of the Requirements for the Degree of

Doctor of Philosophy

in

Biology

The Chinese University of Hong Kong

June 2010

UMI Number: 3446009

UMI®

Dissertation Publishing

ProQuest®

Thesis Committee

Prof. S.W. Chiu (Chair)

Prof. P.K. Wong (Thesis Supervisor)

Prof. J.C. Yu (Internal Examiner)

Prof. J.G. Yu (External Examiner)

Prof. J.D. Gu (External Examiner)

Acknowledgements

Abstract of thesis entitled:

Novel nano/micro-materials for visible-light-driven photocatalysis: Syntheses, characterizations and applications

Submitted by   **Zhang, Lisha**

for the degree of   **Doctor of Philosophy**

at the Chinese University of Hong Kong in May 2010

The work in this dissertation has been published in the *Applied Catalysis A:*

General and *Environmental Science & Technology.*

Abstract

Recent years, environmental problems related to organic pollutants and pathogenic microorganisms have emerged as a high national and international priority. To address these significant problems, photocatalysis causes increasing interest as a kind of green and energy-saving technology. However, the traditional photocatalyst TiO_2 can only be excited by ultraviolet or near-ultraviolet radiation, which merely occupies about 4% of the solar light spectrum. Notably, the visible region covers the largest proportion of the solar spectrum (about 48%). In order to efficiently utilize solar light, the development of visible-light-driven (VLD) photocatalysts with excellent performances has been urged.

In this study, two kinds of effective VLD photocatalysts, $AgBr-Ag-Bi_2WO_6$ nanojunction and $Zn:In(OH)_yS_z$ solid solution nanoplates have been synthesized and characterized. $Zn:In(OH)_yS_z$ solid solution nanoplates (Synthesis conditions: 45 mmol L^{-1} thiourea, 26 mmol L^{-1} SDS, $0.4 \leq X \leq 0.7$) have high VLD photocatalytic activities on the degradation of Rhodamine B (RhB), which is due to their suitable band gap and potentials of conduction band and valence band as well as their uniform and small diameter sizes (about 10 nm in width and about 15 nm in length). $AgBr-Ag-Bi_2WO_6$ nanojunction exhibits excellent VLD photocatalytic performance both on the degradation of Procion Red MX-5B and pentachlorophenol, and on the disinfection of various bacteria including *Escherichia coli*, *Pseudomonas fluorescens* and *Alteromonas macleodii*. Its excellent performance results from the broadened

visible-light response and the synergic effect among the three components under the visible light irradiation, namely the vectorial electron transfer of $Bi_2WO_6 \rightarrow Ag \rightarrow AgBr$.

Moreover, a novel and versatile partition setup has been first constructed to investigate the fundamental mechanism of photocatalytic process. The results indicate that the functional reactive species produced by VLD $Zn:In(OH)_yS_z$ solid solution nanoplates mainly remain on the surface, thus the direct contact between $Zn:In(OH)_yS_z$ solid solution nanoplates and RhB is a prerequisite for the degradation of RhB during the photocatalytic process. However, the functional reactive species produced by $AgBr-Ag-Bi_2WO_6$ nanojunction can diffuse into the bulk, thus the direct contact between the $AgBr-Ag-Bi_2WO_6$ nanojunction and bacteria is unnecessary for the photocatalytic disinfection of bacteria.

Therefore, in this work, the exploration of VLD photocatalyst gives us the opportunities to utilize solar energy to solve the environmental problems and energy crisis, and the investigation of fundamental mechanism provides us more deep understanding for photocatalytic process.

摘要

　　近年來，環境污染問題，尤其是由有機物染物和有害微生物造成的環境污染問題已經成為國內和國際上迫切需要解決的問題。光催化技術是在光照條件下去除污染物，由於其綠色節能的特點，引起了人們的廣泛關注。但是以二氧化鈦為催化劑的傳統光催化技術只能利用占太陽光 4%的紫外光，極大地限制了光催化技術在環保中的實際應用。而可見光占太陽能 48%的能量，因此開發新型高效的可見光光催化劑是同時緩解環境污染和能源短缺兩大難題的有效途徑。

　　我在這項研究工作中製備了兩種新型高效的可見光光催化劑：AgBr-Ag-Bi$_2$WO$_6$ 納米節和 Zn:In(OH)$_y$S$_z$ 固溶體納米片。由於具有適合的禁帶寬度和價帶導帶電位，以及均勻的納米尺寸的粒徑（長約 15nm，寬約 10nm），Zn:In(OH)$_y$S$_z$ 固溶體納米片對降解羅丹明展現了優秀的可見光光催化活性。而可見光激發下的 AgBr-Ag-Bi$_2$WO$_6$ 納米節不僅對偶氮染料 Procion Red MX-5B 和五氯苯酚具有優良的光催化降解性能，而且對各種細菌，如大腸桿菌菌、假單胞細菌和交替單胞菌也具有高效的殺滅和去處性能。AgBr-Ag-Bi$_2$WO$_6$ 納米節優異的可見光光催化性能源於其寬化的可見光響應和納米節中三種組分的協同效應，即電子從 Bi$_2$WO$_6$ 到 Ag 再到 AgBr 的矢向轉移。

　　更為重要的是，我還首次構建了一種新型簡單的分離裝置用於光催化降解有機物和滅菌的機理方面的研究。結果發現由可見光激發 Zn:In(OH)$_y$S$_z$ 固溶體納米片產生的活性成分如空穴和羥自由基主要分佈在催化劑的表面，因此羅丹明和 Zn:In(OH)$_y$S$_z$ 固溶體的直接接觸是光催化降解羅丹明的前提條件。而可見光

v

激發 AgBr-Ag-Bi$_2$WO$_6$ 納米節產生的活性成分如羥自由基則可以擴散到溶液中，因此在 AgBr-Ag-Bi$_2$WO$_6$ 納米節爲催化劑的光催化滅菌過程中，細菌即使沒有和催化劑直接接觸，也可以得到滅活。

因此，這項研究工作不僅製備出了新型優異的可見光光催化劑，爲利用太陽能光催化治理環境污染打下了堅實的基礎，而且對光催化機理的研究也爲深入瞭解光催化過程提供了依據。

Table of Contents

List of Figures

List of Plates

List of Equations

2.1   RE(%)=[(C_0- C_t)/ C_0]×100%   40

List of Tables

Abbreviations

AAS	Atomic absorption spectrometry
AOPs	Advanced oxidation processes
$AgBr-Ag-TiO_2$	Silver bromide-silver-titanium oxide
$AgBr-Ag-Bi_2WO_6$	Silver bromide-silver-bismuth tungstate
AgBr	Silver bromide
Ag	Silver
Ag^+	Silver ion
Au	Gold
A. macleodii	*Alteromonas macleodii*
Bi	Bismuth
Bi_2WO_6	Bismuth tungstate
Bi_2O_3	Bismuth oxide
BET	The Brunauer-Emmett-Teller
$Cu:In(OH)_yS_z-SS$	Copper indium hydroxyl sulfide solid solution
Cr	Chromium
CP	Chlorophenol
CB	Conduction band
CTAB	Cetylmethylammonium bromide
ClO_2	Chlorine dioxide
Cl_2	Chlorine
CO_2	Carbon dioxide
CdS	Cadmium sulfide
Cu_2O	Cuprous oxide
$CaBi_2O_4$	Calcium bismuthate
DBPs	Disinfection byproducts
DMSO	Dimethyl sulfoxide
DMPO	5, 5-Dimethyl-1-pyrroline-*N*-oxide
DDT	Dichlorodiphenyltrichloroethane

DCM	Dichloromethane
DRS	Diffuse reflectance spectra
E. coli K 12	*Escherichia coli* K 12
E. coli BW 25113	*Escherichia coli* BW 25113
E_g	Band gap
e^-	Electron
e_{cb}^-	Electrons in the CB
E^0	The standard electrode potential
EDXA	Energy-dispersive X-ray analysis
EPR	Electron paramagnetic resonance
ESCA	Electron spectroscopy for chemical analysis
Fe(II)	Iron (II)
GC-MS	Gas chromatography-mass spectroscopy
HPLC	High performance liquid chromatography
H_2O_2	Hydrogen peroxide
$HO_2\bullet$	Perhydroxyl radical
NHE	Normal hydrogen electrode
H^+	Hydrogen ion
h^+	Hole
h_{vb}^+	Holes in the VB
HOBr	Hypobromous acids
HClO	Hypochlorous acid
HNO_3	Nitric acid
HCl	Hydrochloric acid
HRTEM	High revolutionary transmission electron microscopy
$In(OH)_3$	Indium oxide
$In(OH)_yS_z$-SS	Indium hydroxyl sulfide solid solution
$In(NO_3)_3 \cdot xH_2O$	Indium nitrate hydrate
In_2S_3	Indium sulfide

IC	Inorganic carbon
$In(OH)_yS_z$-SS	$In(OH)_yS_z$ solid solution
K^+	Potassium ion
KNO_3	Potassium nitrate
$K_2Cr_2O_6$	potassium dichromate
KI	Potassium iodide
LUMO	The lowest unoccupied molecular orbital
M	mol L^{-1}
MX-5B	Procion Red MX-5B
MWCO	The molecular weight cutoff
MB	Marine broth
MA	Marine agar
MnO_4^-	Permanganate
NaOH	Sodium hydroxide
Na_2WO_4	Sodium tungstate
NA	Nutrient agar
NB	Nutrient broth
NaCl	Sodium chloride
Na_2EDTA	Ethylenediaminetetraacetic disodium salt
$\cdot OH$	Hydroxyl radical
$\cdot O_2^-$	Superoxide radical
$\cdot OH_b$	Hydroxyl radical in the bulk
$\cdot OH_s$	$\cdot OH$ on the surface of photocatalyst
OH^-	Hydroxyl ion
O_3	Ozone
O_2	Oxygen
PCO	The photocatalytic oxidation
PCP	Pentachlorophenol
PBS	Phosphate buffer saline

P. fluorescens 85070	*Pseudomonas fluorescens* 85070
RhB	Rhodamine B
RH	Organic pollutants
RH_{ads}	Adsorbed organic pollutants
ROSs	Reactive oxygen species
RE	Removal efficiency
R-Zn:In(OH)$_y$S$_z$-SS	Zn:In(OH)$_y$S$_z$ solid solution prepared according to reference (Lei et al., 2006)
SEM	Scanning electron microscope
SDS	Sodium dodecyl sulfate
S	Sulfur
TiO$_2$	Titanium dioxide
TOC	Total organic carbon
TC	Total carbon
TEM	Transmission electron microscopy
UV	Ultraviolet light
VB	The valence band
VLD	visible-light-driven
WO$_3$	Tungsten (VI) oxide
XPS	X-ray photoelectron spectroscopy
XRD	X-ray diffraction
X	The atomic ratio of Zn^{2+} to In^{3+} in the synthesis solution
Zn: In(OH)$_y$S$_z$	Zinc indium hydroxyl sulfide
Zn(NO$_3$)$_2$	Zinc nitrate
ZnS	Zinc sulfide
Zn:In(OH)$_y$S$_z$-SS	Zn:In(OH)$_y$S$_z$ solid solution
Zn:In(OH)$_y$S$_z$-SSN	Zn:In(OH)$_y$S$_z$ solid solution nanoplate

1. General introduction

1.1 Environmental problems

Recent years, increasing population, accelerating industrialization and urbanization as well as technological innovation impose great pressures on the natural environment, where mankind depends for survival. Especially, environmental problems related to organic pollutants and pathogenic microorganisms have emerged as a high national and international priority (Hoffmann et al., 1995; Shannon et al., 2008).

It is well known that environmental problems result mainly from different kinds of organic pollutants, such as the colorant and pesticide. On the one hand, as the typical colorants, Rhodamine B (RhB) (The chemical structure is shown in Fig. 1.1) and azo dyes with amounts exceeding 1 million tons have been produced and utilized in the world every year (Stolz, 2001). Azo dyes are the aromatic compounds which contain azo group(s) (-N=N-) such as Procion Red MX-5B (MX-5B) (The chemical structure is shown in Fig. 1.2). They are xenobiotic in nature and usually recalcitrant to common chemical and biological degradation process due to the stability of their molecular structures (So et al., 2002; Pandey et al., 2007). Once the untreated effluents containing colorants from textile and dyestuff industries are discharged into the water bodies, unacceptable aesthetic effects can be rendered in the presence of these dyes even at ppm level (Banat et al., 1996; Pandey et al., 2007). The transfer of oxygen and light can also be inhibited, which destroy the living environment of

aquatic biology (Pandey et al., 2007). Even worse, parts of azo dyes show carcinogenic and mutagenic responses (Banat et al., 1996; Umbuzeiro et al., 2005), and the aromatic amine generated during the degradation of azo dyes are also usually mutagenic, cytotoxic and carcinogenic (Platzek et al., 1998; Pinheiro et al., 2004). On the other hand, pesticides have serious adverse effects on the environment. For example, Pentachlorophenol (PCP) (The chemical structure is shown in Fig. 1.3), a colorless organic fungicide, was, and still is, one of the most frequently used pesticides for a wood preservative. The toxicity of PCP comes from its interference with oxidative phosphorylation (Jorens and Schepens, 1993). Studies show that the exposure to PCP may be at risk of malignant disorders such as nasal carcinoma and soft tissue sarcoma (Jorens and Schepens, 1993), and the direct contact with PCP can irritate the skin, eyes, and mouth (United Stated Environmental Protection Agency (USEPA), 2006).
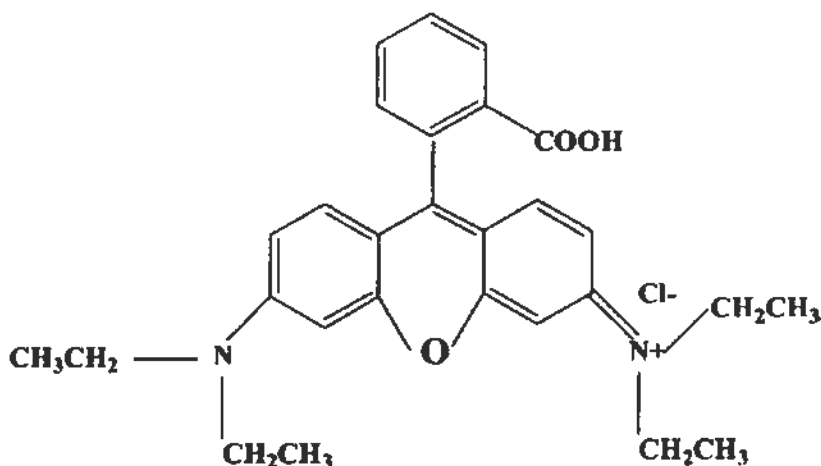
Fig. 1.1 The chemical structure of RhB (Fu et al., 2005).
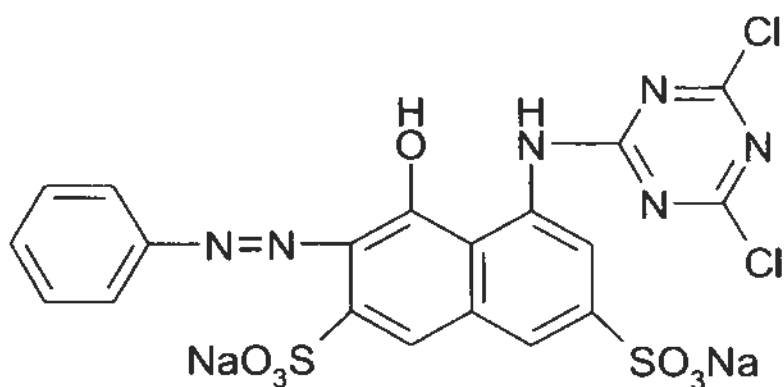
Fig.1.2 The chemical structure of an azo dye, MX-5B (So et al., 2002).
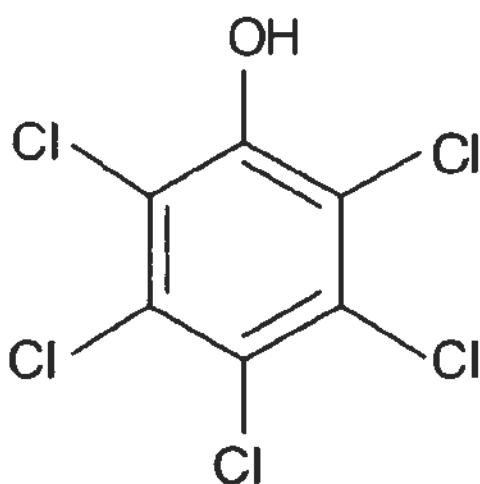
Fig. 1.3 The chemical structure of PCP (Ray et al., 2002).

In addition, millions of deaths and many millions of cases of disease and disability are caused by the contamination of harmful microorganisms every year (Shannon et al., 2005). Contaminated water is the major source for many outbreaks of diseases including cholera, dysentery, guinea worm, typhoid fever and intestinal worms. These diseases are generally related waterborne pathogens such as *Escherichia*, *Salmonella*, *Campylobacter*, and *Shigella*, etc. (Centers for Disease Control and

Prevention, 2005). For example, from 1991 to 2000, 155 outbreaks of diseases occurred in U.S. water systems and caused 431,846 cases of illness basing on the statistics from Morbidity and Mortality Weekly Report of Center for Disease Control and Prevention (Chlorine Chemistry Division of the American Chemistry Council, 2003). Worldwide, about 1.1 billion people, i.e. one-sixth of the world population lack access to safe drinking water according to the 2004 WHO report (WHO, 2004). The diarrhea in the unclean water kills about 1.8 million people each year, 1.6 million of whom are children under 5 years old (WHO, 2004). Besides, with the accelerating progress of urbanization, the air especially in the closed system contaminated by the pathogens transmitted via air such as SARS and swine influenza, recently also becomes the most pervasive public health problems throughout the world.

Therefore, these environmental problems bring severe threats to sustainable development of human. As a response, the development of low cost, effective and practical methods to destruct these pollutants becomes an imperative task.

1.2 Advanced oxidation processes (AOPs)

In order to address above environmental problems, extensive research has been undertaken to develop advanced biochemical and physicochemical technologies to eliminate hazardous chemical compounds and harmful microorganisms from our environment (Hoffmann et al., 1995).

Among these current technologies, the AOPs appear to be a promising approach, which have been reported to be effective for the destruction of organic pollutants and harmful microorganisms, even that resistant to conventional methods (Shannon et al., 2006; Saritha et al., 2007). AOPs rely on the generation of highly reactive oxygen species (ROSs) mainly including hydroxyl radical ($\cdot$OH), superoxide radicals ($\cdot O_2^-$) and hydrogen peroxide (H_2O_2) by using the energy of solar, chemicals or other forms (Ollis et al., 1993; Saritha et al., 2007). Table 1.1 shows the oxidation potentials of some ROSs and common oxidative species (Titus et al., 2004). The oxidation potential of $\cdot$OH is 2.80 V which is next below that of the fluorine, the strongest oxidative chemical. Thus, the oxidative ability of $\cdot$OH is more powerful than chlorine, ozone and permanganate. Apart from $\cdot$OH, other ROSs such as H_2O_2, $HO_2\cdot$ also have the strong oxidative abilities as shown in Table 1.1. Thanks to the powerful oxidative and non-selective nature of these radicals, AOPs are widely applied in the wastewater treatment, disinfection and air cleaning (Ollis et al., 1993; Shannon et al., 2006; Saritha et al., 2007).

The free radicals of ROSs are clusters of atoms with unpaired electron, making them very unstable and reactive. So they should be produced continuously "*in situ*" through chemical or photochemical reactions. The following sections will focus on the introduction about the main approaches to obtain these radicals.

Table 1.1 The oxidation potentials of common oxidative species in acidic media (Titus et al., 2004)

Species	Oxidation potential (V vs NHE)
Fluorine (F_2)	3.03
Hydroxyl radical ($\cdot OH$)	2.8
Atomic Oxygen	2.42
Ozone (O_3)	2.07
Hydrogen peroxide (H_2O_2)	1.78
Perhydroxyl radical ($HO_2\cdot$)	1.7
Permanganate (MnO_4^-)	1.68
Hypobromous acids (HOBr)	1.59
Chlorine dioxide (ClO_2)	1.57
Hypochlorous acid (HClO)	1.49
Chlorine (Cl_2)	1.36

1.2.1 Wet air oxidation

Wet air oxidation is an approach to elevating the temperature and pressure of the compressed air and the organics in a waste water stream to about 300°C and 13 MPa, respectively, to oxidize or finely divide the organics, as shown in Equations 1.1–1.7 (Alaton et al., 2003).

The high temperature and pressure firstly activate the dissolve oxygen to disintegrate the organic pollutants (RH) during this process. Beside the generation of ROSs, these reactions also generate organic radicals, which can initiate the further organic degradation with assistance of the dissolved oxygen as shown in Equations 1.2 and 1.3. Thus during this process, many operating parameters such as

temperature, pressure and the oxygen supply affect the formation of the free radicals and therefore the pollutants degradation rate (Zhou et al., 2007).

$RH + O_2 \rightarrow R\bullet + HO_2\bullet$ (initiation) (Equation 1.1)

$R\bullet + O_2 \rightarrow RO_2\bullet$ (propagation) (Equation 1.2)

$RO_2\bullet + RH \rightarrow ROOH + R\bullet$ (propagation) (Equation 1.3)

$ROOH \rightarrow RO\bullet + \bullet OH$ (autocatalytic decomposition) (Equation 1.4)

$RO\bullet + RH \rightarrow ROH + R\bullet$ (propagation) (Equation 1.5)

$\bullet OH + RH \rightarrow R\bullet + H_2O$ (propagation) (Equation 1.6)

$2ROO\bullet \rightarrow ROOR + O_2$ (termination) (Equation 1.7)
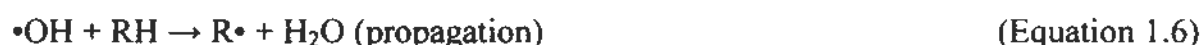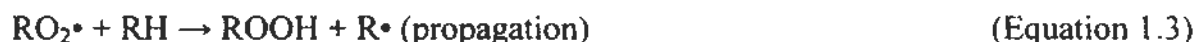
1.2.2 Ozonation based oxidation

Ozonation is a kind of AOPs based on the generation of ROSs via the decomposition of ozone. In fact, ozone itself is a powerful oxidant even more powerful than chlorine (Table 1.1), thus it can directly degrade organic pollutant and disinfect bacteria. However, it is easily decomposed into oxygen atom and oxygen molecule, which results in a low utilization efficiency and short-term effect (Hoigéne et al., 1983). As a result, the ozonation is usually combined with other approaches such as H_2O_2 and ultraviolet light (UV) to enhance the degradation/inactivation efficiency and extend the residual effect. In the system of O_3/H_2O_2, $\bullet OH$ are generated by a radical-chain mechanism by interaction between O_3 and H_2O_2 (Adams et al., 1994). The global reaction is as follows:

$$H_2O_2 + O_3 \rightarrow \bullet OH + 3O_2 \qquad\qquad \text{(Equation 1.8)}$$

1.2.3 Photolysis based oxidation

UV, especially UV-C with wavelength ranged from 200-280 nm, have powerful energy. Irradiated by UV-C, some organic pollutants such as chlorophenol (CP) could be dissociated into fragments and further degraded into carbon dioxide, water and chloride as shown in Equations 1.9 and 1.10 (Titus et al., 2004):

$$CP + h\nu \rightarrow \text{Intermediates} \qquad\qquad \text{(Equation 1.9)}$$

$$\text{Intermediates} + h\nu \rightarrow CO_2 + H_2O + Cl^- \qquad\qquad \text{(Equation 1.10)}$$

Besides, UV-C irradiation can inactivate the microorganisms by damaging their deoxyribonucleic acid and ribonucleic acids (Wolfe, 1990). However, it appears to be less effective than other processes, and thus the radiation is usually combined with O_3 or H_2O_2 to form UV/O_3 or UV/H_2O_2, respectively. Regarding the mechanistic pathways, for example, in the system of UV/H_2O_2, UV radiation could dissociate one H_2O_2 molecule into two •OHs with the input of one quantum of radiation according to the following reaction (Esplugas et al., 2002):

$$H_2O_2 + h\nu \rightarrow 2\bullet OH \qquad\qquad \text{(Equation 1.11)}$$

1.2.4 The Fenton process

The Fenton reaction is a catalytic process based on the generation of •OH by an electron transfer between H_2O_2 and a metal salt (Titus et al., 2004). During this process, the metal salt actually acts as a catalyst, and the most common one used by far is iron (II) salt (Safarzadeh-Amiri et al., 1996). Thus, the typical Fenton reaction occurs at acidic condition in homogeneous aqueous system as follows:

$$H_2O_2 + Fe^{2+} \rightarrow Fe^{3+} + •OH + OH^-$$
(Equation 1.12)

It should be noted that the behavior of the Fenton system cannot be completely interpreted only based on Equation 1.12. In fact, the adoption of a proper value of pH at about 2.7 subsequently favors the reduction of Fe^{3+} to Fe^{2+}, generating other ROSs such as perhydroxyl radical ($HO_2•$) and recovering the catalyst Fe^{2+} as indicated by Equations 1.13 and 1.14 (Pignatello et al., 1992).

$$Fe^{3+} + H_2O_2 \rightarrow H^+ + FeOOH^{2+}$$
(Equation 1.13)

$$FeOOH^{2+} \rightarrow HO_2• + Fe^{2+}$$
(Equation 1.14)

An extension of Fenton process including photo-Fenton or electro-Fenton process is also explored to improve the efficiency of dark-Fenton or Fenton-like reagent, respectively, by means of the interaction of light radiation or electronic current with Fenton's reagent (Pignatello et al., 1992; Andreozzi et al., 1999).

The main problems of the above mentioned AOPs such as wet air oxidation, ozonation based oxidation, UV/H$_2$O$_2$ and Fenton's reagent lie in the high cost of reagents such as hydrogen peroxide or energy sources like electricity. Besides, UV-C light can damage the skin's DNA and the direct use of UV light has potential dangers to human. Therefore, another efficient and cheap AOP, photocatalysis has become to be of real interest for eliminating both aquatic and atmospheric contaminants (Hoffmann et al., 1995; Saritha et al., 2007).

1.3 Photocatalysis

1.3.1 Basic principles of photocatalysis

Photocatalysis is defined as the acceleration of a photoreaction in the presence of a catalyst, which implies that both light and photocatalyst are required to realize the conversions of light energy to chemical energy in more than one homogeneous medium, so it is also called "heterogeneous photocatalysis" (Fox and Dulay, 1993; Hoffmann et al., 1995).

The basic physical and photochemical principles of photocatalysis are widely investigated in the previous studies (Hoffmann et al., 1995; Bhatkhande et al., 2001; Zhao and Yang, 2003). The basic mechanism of photocatalysis can be represented by the schematic diagram of Fig. 1.4.
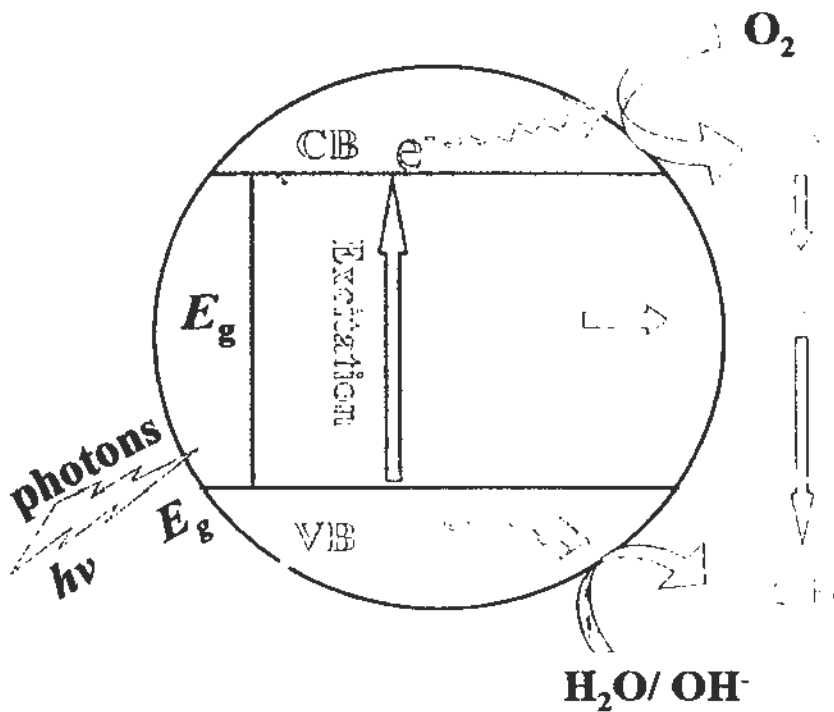
Fig. 1.4 A schematic diagram showing the mechanism of photocatalysis with semiconductor coupled with light irradiation (Hoffmann et al., 1995; Bhatkhande et al., 2001; Zhao and Yang, 2003).

Generally, most of semiconductors with small but nonzero band gap (E_g) are potential materials to initiate photocatalytic reactions, serving as a photocatalyst. E_g refers to the energy interval between the top of the valence band (VB) and the bottom of the conduction band (CB). VB is the highest energy band where electrons normally occupy all electronic levels at absolute zero temperature, while CB is defined as the lowest energy band without electrons at normal state. The small E_g allows excitation of electrons from VB to CB by the input of energy at certain level, and the excited electrons can move freely within the atomic lattice of semiconductors.

As illustrated in the schematic diagram (Fig. 1.4), when the semiconductor is irradiated by photon with energy (hv) equal to or exceeding E_g, an excitonic transition occurs to promote a VB electron to CB. The electron vacancy at the VB results in a positive hole, forming electron (e^-) and hole (h^+) pairs. The electron-hole pairs can migrate to the semiconductor surface to induce the redox reactions with the surrounding medium if the conditions such as the potentials of the charges and the reactants are satisfied. On the one hand, reductive reactions can be initiated by the photogenerated CB electrons if its redox potential is sufficiently negative to allow the reduction of the adsorbed species. The absorbed oxygen is the most common electron acceptor and can be reduced by the photogenerated electrons into $\cdot O_2^-$. The $\cdot O_2^-$ is extremely unstable, and part of them can be transferred into H_2O_2. Portions of resulting H_2O_2 also may undergo the reactions to generate the $\cdot OH$. On the other hand, if the redox potential of the VB is more positive than that of H_2O/OH^-; the photogenerated holes in VB will oxidize the absorbed H_2O or hydroxyl ion (OH^-) to generate $\cdot OH$. Of course, photogenerated holes in VB can also degrade the adsorbed organic compounds if its oxidative ability is powerful enough. Based on highly oxidative activities of the photogenerated holes in VB and ROSs, the various contaminants including the organic pollutant and the microorganisms can be destructed during the photocatalytic process.

However, during the photocatalytic process, the electron–hole pairs readily recombine and dissipate the stored energy as heat or luminescence (Fig. 1.4). This recombination process is the most significant competing reaction to inhibit the

generation of the ROSs. It can be determined by various factors including the rate and pathway of carrier transfer, interfacial carrier trapping and the rates of induced redox reactions (Hoffmann et al., 1995; Bhatkhande et al., 2001). Moreover, these factors are closely associated with the properties of the semiconductor and the absorbents on the surface of the semiconductors.

1.3.2 Titanium dioxide (TiO_2) photocatalysis

1.3.2.1 The overall of TiO_2 photocatalysis

Photocatalysis was first discovered in 1972, when Fujishima and Honda (1972) used a TiO_2 anode to photochemically split water into oxygen and hydrogen gas under the UV light illumination. TiO_2 photocatalysis was first extended to environmental protection till 1977 when Frank and Bard (1977) reported the photocatalytic oxidation of cyanide and sulfite in aqueous medium by TiO_2 under sunlight illumination. Subsequently, the reports on the photocatalytic reduction of carbon dioxide (CO_2) by the light-irradiated TiO_2 pushed the application of photocatalysis forward to the environmental frontiers (Inoue et al., 1979). Moreover, these studies also sparked much interest in the photocatalysis as a possible approach to inexpensively convert solar radiation to chemical energy.

Till now, many the semiconductors such as metal oxides (e.g., TiO_2 and WO_3) and chalcogenides (e.g., CdS and ZnS) (Hoffmann et al., 1995; Prousek, 1996) have been used as photocatalysts. Among these photocatalysts, TiO_2 is by far the most widely investigated photocatalyst because it is highly photoactive, biologically and

chemically inert, nontoxic, and inexpensive (Ollis et al., 1989; O'Regan and Grätzel, 1991; Hoffmann et al., 1995). It has also been proved that the TiO_2 photocatalysis is an effective method to decompose or degrade a variety of hazardous contaminates including (1) organics such as azo dye, dichlorodiphenyltrichloroethane (DDT), and chlorinated volatile organic compounds (Ollis et al., 1989; Hoffmann, et al., 1995; So et al., 2002; Zhao and Yang, 2003), (2) kinds of microorganisms such as bacteria, viruses, and fungi (Blake et al., 1999) and (3) some inorganics such as cyanides, sulfites and heavy metals (Frank and Bard, 1977; Prairie et al., 1993).

1.3.2.2 TiO₂ mediated photocatalytic reactions

Due to the relatively wide TiO_2 band gap of 3.2 eV, only UV photons with $\lambda \leq 388$ nm can result in the formation of charge carriers (electrons in the CB (e_{cb}^-) and holes in the VB (h_{vb}^+)) (Equation 1.15):

$$h\upsilon \xrightarrow{\quad TiO_2 \quad} e_{cb}^- + h_{vb}^+ \qquad \text{(Equation 1.15)}$$

After transfer to the surface of the TiO_2, e_{cb}^- - h_{vb}^+ pair will be trapped by the absorbates, initiating the redox reactions. Given that the redox potential of the h_{vb}^+ is much positive, two possible oxidative pathways can be mediated (Hagfeldtt and Grätzel, 1995; Prousek, 1996; Li et al., 2007). Due to the strong oxidative ability of the h_{vb}^+, it can directly degrade the adsorbed organic pollutants (RH_{ads}), producing cationic radicals $RH^+\bullet$ (Equation 1.16). Or, the h_{vb}^+ can oxidize the adsorbed water

and/or hydroxyl (H_2O_{ads}/ OH^-_{ads}) groups to produce •OH (Equations 1.17 and 1.18), which can subsequently degrade RH both on the surface and in the bulk.

$$h_{vb}^+ + RH_{ads} \rightarrow RH•^+ \qquad \text{(Equation 1.16)}$$

$$h_{vb}^+ + H_2O_{ads} \rightarrow •OH + H^+ \qquad \text{(Equation 1.17)}$$

$$h_{vb}^+ + OH^-_{ads} \rightarrow •OH \qquad \text{(Equation 1.18)}$$

For the reductive pathways involved in the degradation of pollutant, it is generally accepted that the e_{cb}^- can reduce the absorbed O_2 to generate $•O_2^-$ (Equation 1.19). Due to the instability of $•O_2^-$ in the water, major part of $•O_2^-$ will further react with e_{cb}^- and hydrogen ion to form H_2O_2 (Equation 1.20), which may participate in the degradation of RH or give rise to additional •OH formation (Equations 1.21 and 1.22) (Hoffmann et al., 1995).

$$e_{cb}^- + O_{2,ads} \rightarrow •O_2^- \qquad \text{(Equation 1.19)}$$

$$•O_2^- + 2H^+ + e_{cb}^- \rightarrow H_2O_2 \qquad \text{(Equation 1.20)}$$

$$H_2O_2 + e_{cb}^- \rightarrow •OH + OH^- \qquad \text{(Equation 1.21)}$$

$$H_2O_2 + •O_2^- \rightarrow •OH + OH^- + O_2 \qquad \text{(Equation 1.22)}$$

An overall reaction for the heterogeneously photocatalytic oxidation of organic molecules or microorganisms to complete mineralization by TiO_2 can be written as follows (Hoffmann et al., 1995; Fujishima et al., 2000; Leung et al., 2008):

RH or microorganisms + O_2 + hv $\xrightarrow{TiO_2}$ CO_2 + H_2O + Mineral acids   (Equation 1.23)
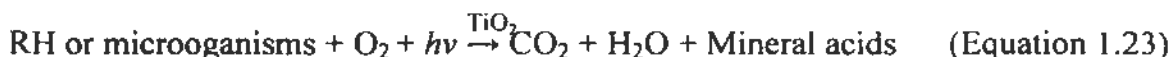
Moreover, in the environmental application, the e_{cb}^- also can be utilized to directly degrade the toxic heavy metal ions to less toxic species such as the reduction of Chromium (Cr) (VI) to Cr(III) as Equation 1.24 (Prairie et al., 1993):

$3e_{cb}^- + Cr(VI)_{ads} \longrightarrow Cr(III)$ (Equation 1.24)

Recombination of charge carries also frequently happens in the TiO_2 photocatalytic process (Hoffmann et al., 1995):

$e_{cb}^- + h_{vb}^+ \longrightarrow$ heat or luminescence   (Equation 1.25)

1.3.3 The advantages and the applications of photocatalysis

Compared with other advanced oxidation processes, photocatalysis shows great potentials in the application of the environmental protection due to the following major advantages (Hoffmann et al., 1995; Kabra et al., 2004):

(i)   Energy saving: it can utilize solar light, a kind of renewable and pollution-free energy, as energy input,

(ii)   Environmental friendlily: The highly active ROSs generated during photocatalytic process can completely mineralize the pollutants, generating

minimum byproduct,

(iii) Non-selective: The ROSs with powerful oxidative ability can degrade a variety of pollutants, and

(iv) Simple and mild: The photocatalytic reactions occur at room temperature and no additional apparatus and chemicals are required.

Besides the environmental protection, interest in other applications such as the production of hydrogen gas, cancer therapy and so on also arouses much attention over the past several years (Fujishima et al., 2000).

However, the commercialization of photocatalytic processes is still in its infancy; and the photocatalytic efficiency and the utilization of solar light should be improved to satisfy the higher requirement. Due to its wide band-gap of 3.2 eV, TiO_2 can only be excited by ultraviolet or near-ultraviolet radiation, which merely occupies about 4% of the solar light spectrum. This significantly limits the application of TiO_2 photocatalysis in the environmental protection. Noticeably, the visible region (400-700 m) covers the largest proportion of the solar spectrum (about 48%). In order to efficiently utilize solar light, the development of visible-light-driven (VLD) photocatalysts has been urged.

1.3.4 The development of VLD photocatalyst

The traditional VLD photocatalysts such as cadmium sulfide (CdS), cuprous oxide (Cu_2O) and WO_3, have their intrinsic disadvantages such as instable, toxic or ineffective when they were applied in the photocatalysis (Kim et al., 2004). Except

for the preparation of these traditional VLD photocatalysts, generally, two main synthesis strategies have been explored for the preparation of VLD photocatalysts. One strategy is to extend the photo-response of TiO_2 to the visible region. The other strategy involves exploiting novel VLD photocatalysts such as complex oxides ($BiVO_4$ (Kudo et al., 1999), $In_{1-x}Ni_xTaO_4$ (Zou et al., 2001) and $PbBi_2Nb_2O_9$ (Kim et al., 2004)) and ternary sulfides (Kale et al., 2006).

1.3.4.1 TiO₂ based VLD photocatalysts

(i) The doped TiO_2 for VLD photocatalysis

Till now, great efforts have been undertaken to prolong the light adsorption of TiO_2 to visible region. The most widely investigated approach is to narrow the band gap of TiO_2 by using dopants. The visible-light response for doped TiO_2 was first discovered in 1986, where a nitrogen doping was attributed for enhancing the photoactivity in the visible spectral range (Sato, 1986). Subsequently, many different elemental components have been employed to tune the electronic structure of TiO_2 including metals such as Fe^{3+}, Ru^{3+}, Os^{3+} and so on (Li et al., 2004; Chen and Mao, 2007), and nonmetals such as C, S, F and so on (Asahi et al., 2001; Yu et al., 2002; Chen and Mao, 2007). Although, the doped TiO_2 can absorb visible light, they also suffer from the photo-instability and charge recombination (Chen and Mao, 2007). The photocatalytic activity of doped TiO_2 largely depends on the dopants, including the dopant concentration, the energy level pattern of the dopants within the TiO_2

lattice, and the distribution of the dopants (Chen and Mao, 2007). Thus, the accurate synthesis process is usually required to achieve the high quality of doped TiO_2 materials (Asahi et al., 2001; Chen and Mao, 2007).

(ii) Sensitization of TiO_2 for VLD photocatalysis

The photosensitization process also can expand the photo-response range of TiO_2 through using a sensitizer. Any material with a narrower band gap or absorption in the visible or infrared regime can be used as sensitizer. These sensitizers include inorganic semiconductors with narrow band gaps such as CdS (Gopidas et al., 1990) and organic dyes such as Erythrosin B (Kamat et al., 1983) and $Ru(bpy)_3^{2+}$ (Vlachopoulos et al., 1988). For example, for CdS-sensitized TiO_2 photocatalyst, the visible light can not directly initiate the excitation of electron from VB to CB in TiO_2 portion of the photocatalyst, but it is powerful enough to excite an electron from the VB across the band gap of CdS ($E_g = 2.5$ eV) to its CB. Since the CB energy level of CdS is more negative than that of TiO_2, the electron in CdS transfers to the CB of the TiO_2 while the hole remains in the CdS, realizing the effective separation of electron-hole pairs (Gopidas et al., 1990). These charges are then free to initiate the subsequent redox reactions with the absorbed acceptors. Therefore, it is also an effective way to construct a more efficient VLD photocatalyst via better charge separation (Chen and Mao, 2007). However, the match between the electronic structures of the sensitizer and TiO_2 as well as the grain boundaries and bonding between the sensitizer and TiO_2 should be carefully considered to avoid the charge

trapping and recombination during the construction of sensitized TiO_2 VLD photocatalysts (Chen and Mao, 2007).

1.3.4.2 The new type of VLD photocatalysts

Beginning in the second half of the 1980s, new photocatalyst materials, other than TiO_2 based photocatalysts, were found (Kudo et al., 1989). In terms of the crystalline structure, these new type of photocatalysts generally possess unique structures such as $K_4Nb_6O_{17}$ (Kudo et al., 1989) with layered structures, and $BaTi_4O_9$ (Kohno et al., 1998) with a tunnel structure. Concerning the elemental components, these photocatalysts are consisted by the metal cations with d^{10} configuration such as Bi^{3+}, Sn^{4+} and In^{3+} (Kudo, 2007). Due to the wide band gaps of these oxide photocatalysts, most of them only respond to UV light (Kudo, 2007). The construction of complex oxides such as $CaBi_2O_4$ (Tang et al., 2004), Bi_2WO_6 (Tang et al., 2004) and $BiFeO_3$ (Gao et al., 2007), and sulfides solid solutions such as $ZnInS_2$ solid solution (Yu et al., 2008) provides an effective way to prepare the new type of VLD photocatalysts. However, it should be noted, the physicochemical factors of these VLD photocatalyst such as the structures, the particle size, and the components have to be further taken into account to improve their VLD photocatalytic performance.

1.4 Nanotechnology

1.4.1 Nanotechnology and nanomaterials

Nanotechnology, the coming ability to build materials and product with atomic

precision, has become one of the most active areas of scientific research in the past few years. One area of nanotechnology receiving much attention is materials research, especially the synthesis, characterization and application of nanomaterials (Siegel et al., 1999).

Nanomaterial refers to a crystalline material with a particle size in the nanometer range, representing a state of matter in the transition between molecules and bulk structures (Siegel et al., 1999). Synonyms for the "nanomaterials" were commonly found in literature including nanostructures, nanocrystals, nanoparticles, quantum dots, colloidal particles, and nanoclusters. Due to the strong correlation between the physical/chemical properties and the shape, size, and structure of materials, designing and preparing novel nano/micro-structured materials has been intensively pursued not only for fundamental scientific interest but also for their various applications in fields such as biological labeling and imaging, catalysis, drug delivery, sensing, and surface-enhanced Raman scattering (Zhang et al., 2007).

1.4.2 The advantages of nanotechnology attribute to photocatalysis

The overall photocatalytic activities of photocatalyst are governed by complex factors such as light absorption and surface properties, redox potentials of CB and VB, rate of charge-carriers recombination, rate of charge carriers induced reactions and so on (Hoffmann et al., 1995; Kabra et al., 2004; Zhang et al., 2007). In addition, the stability of photocatalysts is another important factor for their application (Hoffmann et al., 1995; Hu et al., 2006). These factors bring many difficulties in the

improvement of the VLD photocatalytic activity. Fortunately, the novel phenomena of nanomaterials such as quantum size effect, BET surface effect and carries diffusion effect attributed by the nanotechnology give us opportunities to prepare more effective VLD photocatalysts (Hagfeldt and Gräetzel, 1995; Wang et al., 2005; Zhang et al., 2006).

During the transition from a molecule to bulk particle, the physicochemical properties of materials gradually change from molecular to solid-state behavior with increasing particle size (Hagfeldt and Gräetzel, 1995; Kamat and Meisel, 1997). As shown in Fig.1.5, for the electronic energy states, the nanocrystals bridge the gap between small molecules and bulk particle, and this bulk-to-molecule transition is continuous (Andrew and Nie, 2009). Thus the 'band gaps' of the nanocrystals can be 'tuned' to a desired energy by controlling their particle size, which is called quantum size effects (Hagfeldtt and Grätzel, 1995; Andrew and Nie, 2009). This effect is manifested optically as a change in color, as evidenced by a gradual red-shifting of absorption spectra with increasing particle size (Andrew and Nie, 2009). Apart from tuning the effective band gap, the effect of local confinement of the charge carriers is to produce discrete electronic states in the valence band. As a result, researchers can control the size and shape of these "artificial materials" to widely and precisely tune the energy of discrete electronic energy states and optical transitions (Kamat and Meisel, 1997).
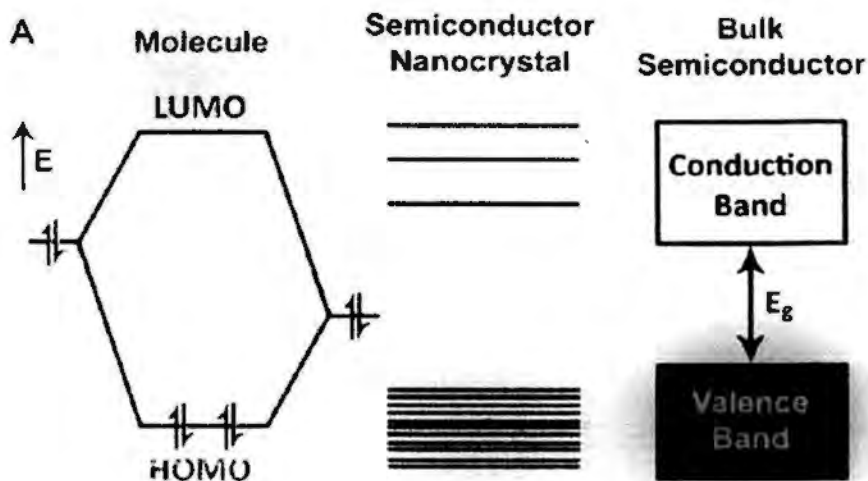
Fig.1.5 Electronic energy states of a semiconductor in the transition from discrete molecules to nanosized crystals and bulk crystals. Blue shading denotes ground state electron occupation (Andrew and Nie, 2009).

With the size of a semiconductor reduced to nano-range, both the fraction of atoms located at the surface and the surface area to volume ratio are increased, which is called the BET surface effect (Hagfeldt and Gräetzel, 1995). This effect may enhance the available surface-active sites and interfacial charge-carrier transfer rates, thus leading to higher photocatalytic activities (Wang et al., 2005). However, some cases suggests that the lower photocatalytic activity is induced by BET surface effect of nanoparticles (Chhabra et al., 1995), which can be explained by the increase in the number of surface defects and electron-hole recombination rates (Hu et al., 2010).

Another main bottleneck of photocatalysis is a high recombination rate of the excited electron–hole pairs in semiconductors. Nanotechnology offers the opportunities to minimize the distances which charges have to transport over after excitation (Zhang et al., 2006). In a bulk semiconductor, recombination occurs if the

excited electrons are located at larger depths than the typical inelastic mean free path of electrons, resulting in the low photocatalytic activity (Hagfeldtt and Grätzel, 1995; Zhang et al., 2006). On the contrary, if the particle size is comparable to or smaller than this distance, a majority of the charge carriers could interact with the absorbed acceptors to initiate the photocatalytic degradation (Hagfeldt and Gräetzel, 1995).

Therefore, the design and construction of new type of VLD photocatalysts with novel components and structures on the micro/nano-scale promise significantly enhanced functions for environmental and energy applications. Meanwhile, the development of synthesis and characterization of these photocatalyst materials can facilitate a fundamental understanding of structure-performance relationships.

2. Objectives

The objectives involved in this project are:

(1) To prepare and characterize the VLD photocatalysts with novel nanostructure and components by liquid-state reaction,

(2) To study the effects of major parameters on the formation and growth mechanism of these novel nano/micro-structured materials,

(3) To use these photocatalysts to degrade organic pollutants and disinfect bacteria and select the photocatalysts with excellent VLD photocatalytic performance, realizing the effective VL-energy-conversion in photocatalytic process,

(4) To investigate the relationship between components and structures of photocatalysts and their photocatalytic efficiencies as well as some important experimental factors that can significantly influence the photocatalytic efficiency, and

(5) To investigate the dye degradation and disinfection mechanism during the PCO and provide more fundamental understanding of VLD photocatalytic oxidation chemistry.

3. AgBr-Ag-Bi₂WO₆ nanojunction: Synthesis, characterizations and photocatalytic degradation of organics

3.1 Introduction

Tungsten (VI) oxide (WO₃) is a kind of traditional visible-light-driven (VLD) photocatalyst (Kim et al., 2004), which has good chemical stability, but still demonstrates low photocatalytic activity in visible light region (Finlayson et al., 2006). On the other hand, since bismuth (Bi) is a kind of p-block metal with a d^{10} configuration, it is found that the Bi 6s can hybridize O 2p levels to form a preferable hybridized VB, which favors the mobility of photoholes in the VB and benefits the enhancement of the photocatalytic performance of the Bi^{3+}-based oxides (Tang et al., 2004). Previous studies have already demonstrated that Bi_6WO_{12} possesses significantly higher optical absorption in the wavelength region above 440 nm than either bismuth oxide (Bi_2O_3) or WO_3, raising the possibility of enhanced photocatalytic activity under solar illumination (Tang et al., 2004). A variety of intermediate oxides exhibiting different but related crystal structures exist in the Bi_2O_3-WO_3 psuedobinary phase system such as $Bi_2W_2O_9$, Bi_2WO_6, Bi_4WO_9, Bi_6WO_{12} and the sillenite, $Bi_{14}WO_{24}$ (Tang et al., 2004). Among them, bismuth tungstate (Bi_2WO_6), a kind of Aurivillius oxides, is one of the simplest Bi_2O_3-WO_3 psuedobinary phase possessing layered structure with the perovskite like slab of WO_6 (Baux et al., 1996; Kim et al., 2005). Due to excellent intrinsic physical and chemical properties such as ferroelectric piezoelectricity, catalytic behavior, and nonlinear dielectric susceptibility, Bi_2WO_6 has attracted extensive attentions (Baux et al., 1996; Kim et al., 2005). In addition to the above properties, it was also reported that Bi_2WO_6 can photocatalytically produce oxygen from water (Kudo and Hijii, 1999)

and decompose both chloroform and aldehyde contaminants (Tang et al., 2004) under visible light irradiation.

It is well known that the photocatalytic activity closely interrelates with the diameter size, morphology and structure of photocatalysts (Kamat, 1993; Zhang et al., 2006; Zhang et al., 2007). In order to improve the photocatalytic activity of Bi_2WO_6, Yu et al. (Yu et al., 2005; Zhang and Zhu, 2005) have reported the preparation of Bi_2WO_6 nanoparticles and nanoplates, respectively, and investigated their VLD photocatalytic activities on the degradation of organics. As stimulated by the promising applications and the novel properties of nanostructures/superstructures, Zhang et al. (2007) and Wu et al. (2007) report the synthesis of hierarchical Bi_2WO_6 superstructure constructed by ordered nano-substructures. Up to date, although efforts have been made to prepare kinds of single-component VLD photocatalysts, there are still some drawbacks hindering their practical application, such as short photogenerated electron-hole pair lifetimes and the limited region of visible light photo-response. To meet the requirements of the future environmental and energy technologies, it is still necessary to design novel VLD photocatalyst systems to further improve photocatalytic efficiencies.

Recently, the coupling of semiconductors with other semiconductors and/or metals on the nanoscale has been reported to greatly improve their photocatalytic performances (Liu et al., 2004; Kim et al., 2005; Tada et al., 2006). For example, the deposition of a metal, such as Ag, on the surface of TiO_2 highly improved its photocatalytic efficiency through the Schottky barrier conduction band electron trapping (Liu et al., 2004). Also, a novel p-$CaFe_2O_4/n$-$PbBi_2Nb_{1.9}W_{0.1}O_9$ nanodiode has shown greatly enhanced photocatalytic activity because of the good separation of photoexcited electrons and holes (Kim et al., 2005). Tada et al. (2006) have revealed

that CdS-Au-TiO$_2$ three-component nanojunction system exhibits a high photocatalytic activity, far exceeding those of the single-and two-component systems, as a result of vectorial electron transfer driven by the two-step excitation of TiO$_2$ and CdS. Hu et al. (2006) also prepared silver bromide-silver-titanium oxide (AgBr-Ag-TiO$_2$) as VLD photocatalyst for the destruction of the organic pollutant and bacteria, where AgBr is the only VLD component and the metal Ag specie on the surface is probably contributing to the enhancement of the electron-hole separation and interfacial charge transfer. These studies demonstrate that the development of better VLD photocatalysts depends on a wide range of visible light photo-response and highly effective interfacial charge transfer.

In order to broaden the range of visible light photo-response and improve the separation of photogenerated electron-hole pairs simultaneously, herein we construct the silver bromide-silver-bismuth tungstate (AgBr-Ag-Bi$_2$WO$_6$) nanojunction system, where both silver bromide (AgBr) and bismuth tungstate (Bi$_2$WO$_6$) are the photochemical systems that can be excited by visible light, while Ag is used as an electron-transfer system. This all-solid-state AgBr-Ag-Bi$_2$WO$_6$ nanojunction system with double visible-light active component exhibits much higher VLD photocatalytic activity than the photocatalyst with single visible-light active component such as Bi$_2$WO$_6$ superstructures, Ag-Bi$_2$WO$_6$ and AgBr-Ag-TiO$_2$, for the degradation of an azo dye, Procion Red MX-5B (MX-5B), and a colorless pollutant, pentachlorophenol (PCP).

3.2 Materials and methods

3.2.1 Preparation of catalysts

1 M sodium tungstate (Na_2WO_4) stock solution was prepared by dissolving 65.972 g of sodium tungstate dehydrate (99%, Sigma-Aldrich, St. Louis, USA) in 200 mL milli-Q® water. And 1 M sodium hydroxide (NaOH) solution was prepared by dissolving 0.4 g NaOH (Riedel-de Haën®, Seelze, Germany) in 100 mL milli-Q® water. The 500 mL 3.65 M nitric acid (HNO_3) solution and 100 mL 1 M hydrochloric acid (HCl) solution stocks were prepared by respectively diluting 124 mL concentrated nitric acid (65%, Merck KGaA, Darmstadt, Germany) with 376 mL milli-Q® water and 8.4 mL concentrated HCl (37%, Merck KGaA, Darmstadt, Germany) with 91.6 mL milli-Q® water.

The flower-like Bi_2WO_6 superstructures were prepared by the hydrothermal method. In the hydrothermal process, water in a sealed vessel such as Teflon-lined autoclave as shown in plate 3.1, can be brought to temperatures well above their boiling points by the increase in autogenerated pressures resulting from heating, which allows the formation of highly crystallized inorganic materials at temperatures substantially below those required by the traditional solid-state reactions. The 50 mL autoclave was purchased from Ri De apparatus and equipment LTD. (Zhengzhou, China). Teflon-lined autoclave is consisted by the outer stainless steel shell and the internal bladder made from polytetrafluoroethylene as shown in Plate 3.2.

Plate 3.1 The sealed Teflon-lined steel autoclave with the volume of 50 mL (Ri De apparatus and equipment LTD., Zhengzhou, China).

Plate 3.2 The components of 50 mL Teflon-lined autoclave (Ri De apparatus and equipment LTD., Zhengzhou, China).

The flower-like Bi_2WO_6 superstructures were prepared by the hydrothermal method according to our previous report (Zhang et al., 2007). As in a typical hydrothermal reaction, 0.98 g Bismuth nitrate pentahydrate (>98%, Sigma-Aldrich, St. Louis, USA) was first dissolved in a 30 mL 3.65 M nitric acid solution. Then, a 20 mL of 0.05 M Na_2WO_4 solution was added dropwise into the above solution to form the suspension. The pH value of the resulting suspension was tuned approximately 1. After being stirred for 12 h, the suspension was added into a 50 mL internal bladder of Teflon-lined autoclave (Plate 3.2) to reach 80% of its total volume. The autoclave was then sealed in a stainless steel tank and heated at 160°C for 24 h

in an oven (1350 FX, Sheldon Manufacturing, Inc., Cornelius, USA) as shown in Plate 3.3. Subsequently, the Teflon-lined autoclave was cooled to room temperature, and the precipitation was collected and washed with milli-Q$^{®}$ water for three times by centrifugation at 18000×g for 3 min using a hermle Z323 centrifuge (hermle, Labortechnik, Germany). Finally, the product of flower-like Bi_2WO_6 superstructures was obtained after dried at 65 °C in an oven (1380 FX, Sheldon Manufacturing, Inc., Cornelius, USA). The obtained sample is shown in Plate 3.4.
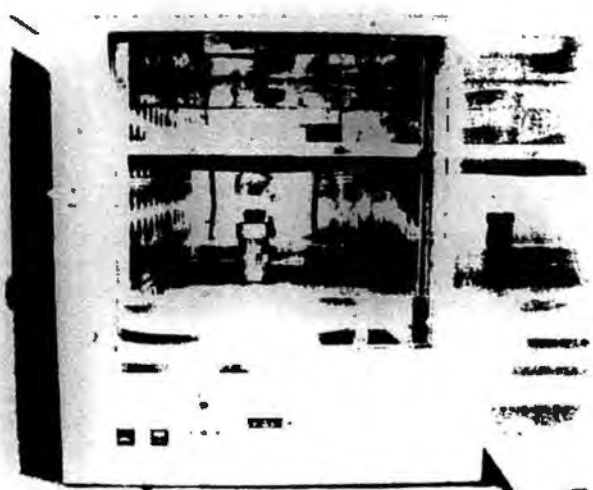
Plate 3.3 The sealed Teflon-lined autoclave containing precursor suspension heated in an oven (1350 FX, Sheldon Manufacturing, Inc., Cornelius, USA).

Plate 3.4 The obtained flower-like Bi_2WO_6 superstructures powder.

The AgBr-Ag-Bi$_2$WO$_6$ nanojunction was then prepared using the modified deposition-precipitation method. Firstly, 0.9 g Bi$_2$WO$_6$ superstructure powder (Plate 3.4) as the substrate was added to 20 mL of milli-Q$^®$ water, and was sonicated with a Branson 2510 sonicator (Branson Ultrasonics B. V., Soest, NL, USA) (Plate 3.5) at 35 kHz for 10 min. Then, 0.45 g of cetylmethylammonium bromide (CTAB) (>98%, Sigma-Aldrich, St. Louis, USA) was added to the above suspension, and the mixture was stirred magnetically for 30 min. In the next step, 0.105 g of silver nitrate (>99.9%, BDH chemicals Ltd., Poole England) in 2 mL of aqueous ammonia (32%, Merck KGaA, Darmstadt, Germany) was quickly added to the mixture, and the resulting suspensions were stirred at room temperature for 24 h. The precipitation product was collected and washed with milli-Q$^®$ water by centrifugation at 18,000×g for 3 min, and dried at 65°C for 24 h. Finally, the powder was calcined in air at 500°C for 3 h using the Bench-top muffle furnace (Barnstead F 48020-80, Kou Hing Hong Ltd., Hong Kong) to obtain the AgBr-Ag-Bi$_2$WO$_6$ nanojunction as shown in Plate 3.6. For comparison, the Ag-Bi$_2$WO$_6$ sample was prepared without the addition of CTAB, the Bi$_2$WO$_6$ sample used in this project was prepared by directly calcining flower-like Bi$_2$WO$_6$ superstructure at 500°C for 3 h, and the AgBr-Ag-TiO$_2$ sample was prepared using same weight of titania P-25 (Degussa Corporation, Frankfurt, Germany) as a substrate instead of Bi$_2$WO$_6$ with other identical conditions.
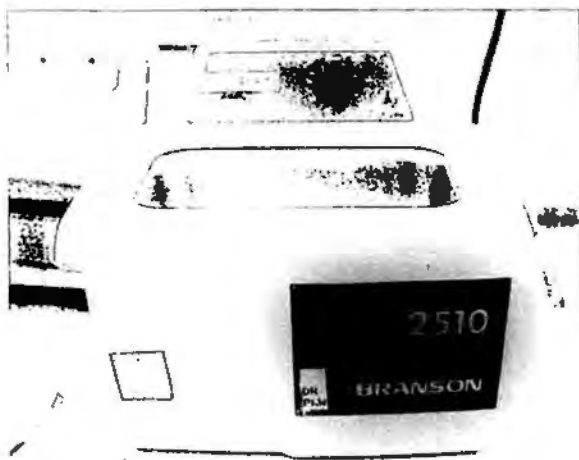
Plate 3.5 A Branson 2510 sonicator (Branson Ultrasonics B.V., Soest, NL, USA).

Plate 3.6 The obtained AgBr-Ag-Bi$_2$WO$_6$ nanojunction powder.

3.2.2 Characterizations of photocatalysts

To investigate the morphology, structure and the elemental composition of AgBr-Ag-Bi$_2$WO$_6$ nanojunction, the as prepared sample was observed and analyzed by the scanning electron microscope (SEM) using an FEI QUANTA-400F field emission scanning electron microscope (Holland) (Plate 3.7) and the transmission electron microscope (TEM) and high revolution TEM (HRTEM) using a FEI TECNAI F20 field emission electron microscope (Holland) equipped with and the energy-dispersive X-ray analysis (EDXA) (Plate 3.8). The sample was first dispersed in milli-Q® water by sonication and spread on a carbon coated-copper grid for the

TEM characterization, while the held sample was coated with an ultrathin coating of gold by Ion Sputter Coater E-1010/1020 (Hitachi Company, Japan) before the SEM observation. The contents of each element were identified by EDXA and were calculated by TECANI G^2 EDAX analysis software (FEI Company, Holland).

Plate 3.7 A SEM using an FEI QUANTA-400F field emission scanning electron microscope (Holland).

Plate 3.8 A TEM/HRTEM using a FEI TECNAI F20 field emission electron microscope (Holland) equipped with the EDXA.

The X-ray photoelectron spectroscopy (XPS) data were recorded to analyze the valence states of elements on the surface with a Quantum 2000 scanning Electron

Spectroscopy for Chemical Analysis (ESCA) microprobe instrument (Φ Physical Electronics, USA) (Plate 3.9) using monochromatic Al Kα radiation (225 W, 15 mA, 15 kV) with the spot size of 100 μm and low-energy electron flooding for charge compensation. To compensate for surface charges effects, binding energies were calibrated using the C 1s hydrocarbon peak at 284.6 eV.

Plate 3.9 ESCA microprobe instrument (Φ Physical Electronics, USA).

To study the crystal phase of the AgBr-Ag-Bi$_2$WO$_6$ nanojunction, the sample powder was fixed on the glass powder sample holder, which was placed on a Huber diffractometer (V612365, Japan) that was equipped with a rotating anode using Cu Kα radiation (Rigaku, Ru-300) (Plate 3.10) to record the X-ray diffraction (XRD) patterns of this fixed sample. The accelerating voltage and the applied current were 40 kV and 60 mA, respectively. Data were recorded at a scan rate of 0.02 deg (2θ) s^{-1} in the 2θ range of 20° to 80°.

Plate 3.10 A Huber diffractometer (V612365, Japan) that was equipped with a rotating anode using Cu Kα radiation (Rigaku, Ru-300).

The powder sample was also fixed on the powder-sample-holder, which was placed into a UV-VIS spectrophotometer (Varian®, Palo Alto, USA) with an integrating sphere attachment (Plate 3.11) to record the UV-visible absorption spectra. The recorded wavelength was set from 270 to 900 nm.
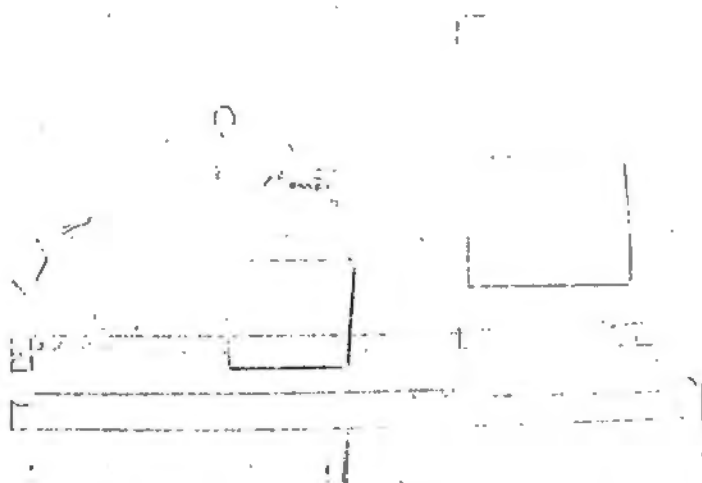
Plate 3.11 A UV-VIS spectrophotometer (Varian®, Palo Alto, USA).

Finally, the zeta-potential of catalysts was measured by a zeta potential analyzer equipped with a data system of ZetaPlus 3.57 version and Model ZetaPlus

(Brookhaven Instruments Corporation, NY, USA) (Plate 3.12). The suspension for the Zeta potential analysis contained 0.05 g L^{-1} of AgBr-Ag-Bi$_2$WO$_6$ nanojunction in the presence of 0.1 mM potassium nitrate (KNO$_3$) (Analytical reagent, ATAX Chemicals, Sydney, Australian) at different pH value. The pH value of the suspension was adjusted by 0.1 M HCl and NaOH solutions.

Plate 3.12 Zeta potential analyzer equipped with a data system of ZetaPlus 3.57 version and Model ZetaPlus (Brookhaven Instruments Corporation, NY, USA).

3.2.3 Preparation of MX-5B and PCP aqueous solutions

MX-5B and PCP were purchased from Sigma-Aldrich Chemical Company Ltd. (St. Louis, USA) in 50 and 98% purity, respectively. Stock MX-5B solution of 1,000 mg L^{-1} was prepared by dissolving 0.5 g of MX-5B powder into 250 mL milli-Q$^{®}$ water. Stock of PCP solution of 1,000 mg L^{-1} was prepared by dissolving 0.1 g of solid PCP into 100 mL of 0.1 M NaOH solution. The stock of MX-5B and PCP solutions were wrapped with aluminum foil and kept at 4 °C.
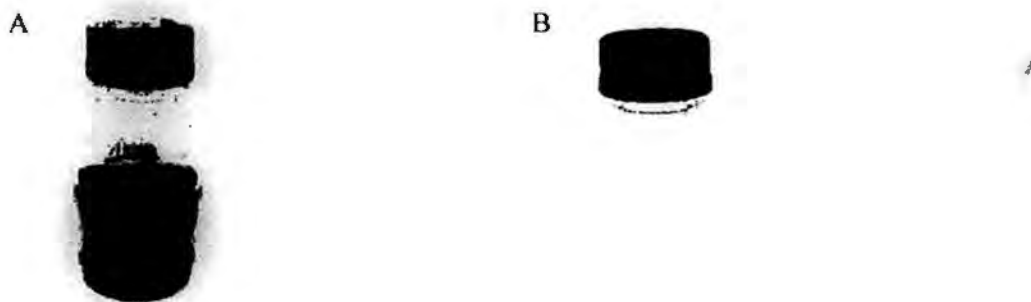
Plate 3.13 Stocks of 1,000 mg L^{-1} MX-5B (A) and PCP (B).

3.2.4 The photoreactor and light source

The light source used here is a 300 W xenon lamp (Beijing Bofeilai Technology Co. Ltd., Beijing) equipped inside of PLS-SXE-300 (Beijing Perfect Light Co. Ltd., Beijing). The photo of the photoreactor and light source was shown in Plate 3.14. Light was passed through a UV cut-off filter ($\lambda \geqq 400$ nm) (Beijing Bofeilai Technology Co., Ltd. Beijing) to cut off the UV light, and then was focused vertically onto a 100 mL beaker containing MX-5B or obliquely onto a flask containing PCP with desired concentration. The baker or the flask was placed on the VELP F20300161 magnetic stirrer plate (VELP®, Chelleson Sci. Inst. Co., Hong Kong) and a stirrer bar was put inside the reaction mixture so that the photocatalyst could be stirred and evenly distributed in the suspension during the photocatalytic reaction. By adjusting the constant voltage and the distance between flask/backer and Xenon lamp, light intensity irradiating on the flask/backer could be adjusted. During the irradiation, the ventilation fans equipped inside of the PLS-SXE-300 and the air condition of the room were turn on to maintain the room temperature so that the thermal effect could be negligible.
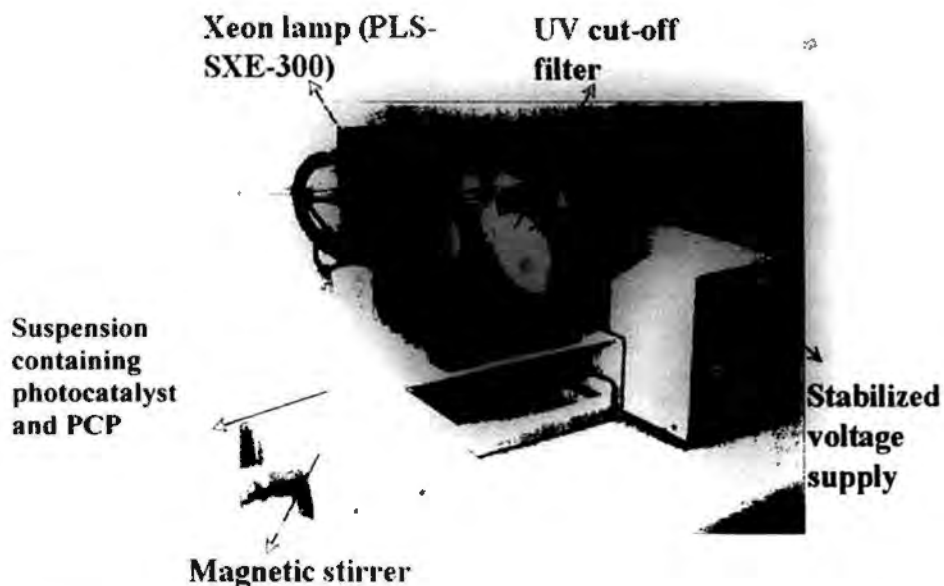
Plate 3.14 The light source and photoreactor with visible light obliquely focus onto a flask containing a aqueous suspension with photocatalyst and PCP.

3.2.5 Photocatalytic degradation of MX-5B

3.2.5.1 Photocatalytic degradation process of MX-5B

During the photocatalytic degradation of MX-5B, the photoreactor was adjusted to allow the visible light vertically irradiating on the reaction mixture as shown in Plate 3.15. The visible light intensity was measured by a light meter (LI-COR, USA) and was fixed at about 230 mW cm^{-2}. In each experiment, suitable amount of photocatalyst was added into MX-5B aqueous solution. The reaction mixture containing the photocatalyst and MX-5B were magnetically stirred in the dark for 60 min to ensure that an adsorption/desorption equilibrium was established between the photocatalyst and MX-5B. Then the reaction mixture was irradiated by the visible light.
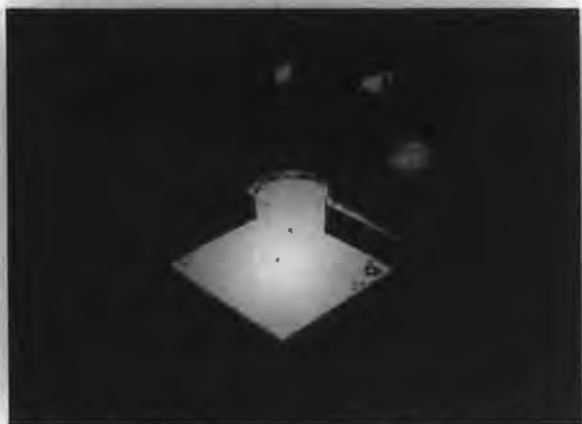
Plate 3.15 The photoreactor with visible light vertically irradiating onto reaction mixture containing photocatalyst and MX-5B.

3.2.5.2 Determination of MX-5B decolorization

To measure the remaining MX-5B concentration, at different stages of PCO process, 1.5 mL aliquots were collected and centrifuged using a MSE MSB 010 microcentrifuge (SANYO, Japan) to remove the catalyst particulates for analysis (Plate 3.16). The supernatant was tested at the wavelength of maximal absorption (538 nm) in the UV-VIS spectra of MX-5B by a Helis Gamma UV-VIS spectrophotometer (Thermo Fisher Scientific, Waltham, USA) (Plate 3.17). A series of MX-5B standards were prepared from 2.5 to 80 mg L^{-1} to construct a standard curve for qualification. Then the concentration of MX-5B in the reaction mixture before and after the PCO process was calculated according to the standard curve. The photocatalytic performance was evaluated by the decrease of the concentration, and removal efficiency (RE) (%) of MX-5B. RE(%) was calculated by the Equation 2.1:

$$RE(\%) = [(C_0 - C_t)/ C_0] \times 100\% \qquad \text{(Equation 2.1)}$$

Where C_0= MX-5B concentration after establishment of adsorption/desorption equilibrium (mg L^{-1}), C_t= MX-5B concentration after photocatalytic treatment.

Plate 3.16 A MSE MSB 010 microcentrifuge (SANYO, Japan)
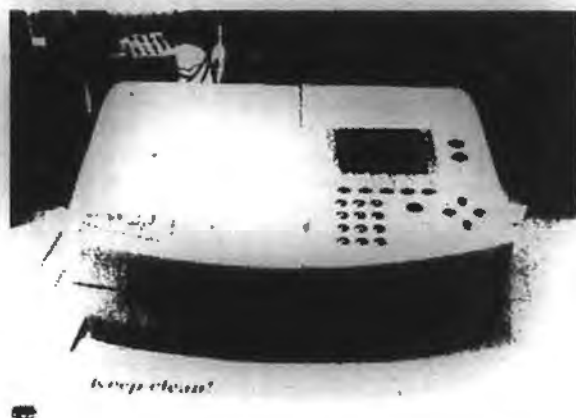
Plate 3.17 A Helis Gamma UV-Vis spectrophotometer (Thermo Fisher Scientific, Waltham, USA)

3.2.5.3 Decolorization performances of different photocatalysts

Four kinds of photocatalysts including Bi_2WO_6, $Ag-Bi_2WO_6$, $AgBr-Ag-Bi_2WO_6$ nanojunction and $AgBr-Ag-TiO_2$ prepared in Section 3.2.1 were used to evaluate the decolorization performance of $AgBr-Ag-Bi_2WO_6$ nanojunction under visible light illumination. The reaction mixtures for these four photocatalysts were prepared by adding the corresponding amount of photocatalyst with same amount of VLD component into 100 mL 50 mg L^{-1} MX-5B solution. The following procedures were

3.2.5.4 Effect of initial MX-5B concentration

To determine the effects of initial MX-5B concentration on the photocatalytic degradation of MX-5B, the photocatalytic experiments were carried out by using the reaction mixture with different concentrations of MX-5B (0, 10, 20, 40, 60 and 80 mg L^{-1}) and 25 mg AgBr-Ag-Bi_2WO_6 nanojunction. All the above experiments were conducted in triplicates.

3.2.5.5 Effect of initial pH value

To determine the effect of pH, the initial pH level of reaction mixture was adjusted by adding drops of 1 M HCl or NaOH solution, and was monitored using a pH meter (Thermo Orion, USA). The investigated pH values are 3.0 ± 0.2, 5.0 ± 0.2, 7.0 ± 0.2 and 9.0 ± 0.2. All the above experiments were conducted in triplicates.

3.2.5.6 Stability of AgBr-Ag-Bi_2WO_6 nanojunction

In order to study the stability of the AgBr-Ag-Bi_2WO_6 nanojunction, the effect of multiple cycles were investigated. The AgBr-Ag-Bi_2WO_6 nanojunction after the photocatalytic process in Section 3.2.5.3 was collected, and washed for three times with the milli-$Q^{®}$ water, and then was dried at 80°C. Then the 0.05 g AgBr-Ag-Bi_2WO_6 nanojunction was reused to photocatalytically degrade 50 mg L^{-1} MX-5B under visible light. Eventually, the five cycles were carried out to examine the stability of AgBr-Ag-Bi_2WO_6 nanojunction.

3.2.5.7 Photocatalytic mineralization of MX-5B

The photocatalytic mineralization of MX-5B was analyzed by TOC of the suspension and the generation of CO_2 and IC during the photocatalytic process. For the TOC detection, 200 mL reaction mixture initially containing 0.4 g AgBr-Ag-Bi_2WO_6 nanojunction and 40 mg L^{-1} MX-5B was irradiated by visible light. At each fixed time intervals, 20 mL suspension was taken out and the catalyst was removed by filtering the suspension through a Millex[®]-HN Millipore filter (pore size 0.45 μm, Millipore Corporation, Ireland). TOC of the filtrate was measured following the protocol of the Instruction Manual (Shimadzu Corporation, 2001). The filtrate was put into pre-cleaned sample vials for total carbon (TC) and IC determination by auto-sampler ASI-V connecting to a TOC analyzer TOC-V$_{CSH/CSN}$ (Shimadzu Corporation, Kyoto, Japan) (Plate 3.18). Then the TOC can be obtained from the difference between TC and IC.

For the detection of the evolved CO_2 and IC concentration, the flask containing 0.4 g AgBr-Ag-Bi_2WO_6 nanojunction and 40 mg L^{-1} MX-5B was saturated by the nitrogen gas before closed. Then the closed system was irradiated by the visible light. After irradiation for the desired time, the gas in the reactor was pumped through the Kitagawa precision gas detector tubes for carbon dioxide (Komyo Rikagaku Kogyo K.K., Kawasaki, Kanagawa, Japan) with the 25 mL syringe (TEPUMO[®], Germany). The amount of the evolved CO_2 was determined by a degree of the color-changed CO_2 adsorbent in the tubes. Then, the amount of evolved CO_2 was calculated by its content in the pumped gas according to the protocol of the Instruction Manual (Komyo Rikagaku Kogyo K.K., Japan). The resulting mixture was immediately filtered and the solution phase was subjected to measurement of IC by the TOC analyzer (Plate 3.18). All the above experiments were conducted in triplicates.

Plate 3.18 A TOC analyzer TOC-V$_{CSH/CSN}$ (Shimadzu Corporation, Kyoto, Japan) connected with an auto-sampler ASI-V.

3.2.6 Photocatalytic degradation of PCP

3.2.6.1 Photocatalytic degradation process of PCP

In this project, the colorless organic compound, PCP was also used as a pollutant target to be photocatalytically degraded. After establishment of adsorption/desorption equilibrium (60 min), the flask containing 50 mL suspension with 10 mg L^{-1} PCP and suitable amount of photocatalyst were irradiated under visible light as shown in Plate 3.13. At given irradiation time intervals, 1.5 mL aliquots of suspension were collected and filtered through a Millex®-HN Millipore filter to remove the catalyst particulates. Then the filtrate was inject into the clean 12×32 mm vials (Waters®, Waters Corporation, Milford, Ireland) and was ready for determination of PCP concentration.

3.2.6.2 Determination of PCP concentration

PCP concentration was determined by using reverse-phase high performance liquid chromatography (HPLC) described previously (Pang et al., 2007). The

analysis was performed by using a Waters 600 multi-solvent delivery system equipped with a Waters reverse-phase C18 (5 μm particle) column (4.6 mm×250 mm, Waters Spherisorb®, Waters Corporation, Milford, Ireland) on a Waters separations module (Waters 2695) comprised with a Waters 996 photodiode array detector (Plate 3.19). The mobile phase consisted of 75% HPLC grade acetonitrile (Mallinckrodt, Paris, Kentucky, USA), 24.875% Milli-Q water, and 0.125% acetic acid (BDH, Poole, England) at a flow rate of 1.5 mL min^{-1}. The maximum absorption wavelength was detected at 215 nm. Concentrations of PCP were calculated according to a standard curve obtained from HPLC measurements of the standard at different concentrations from 0.5 to 200 mg L^{-1}. The detection limit for PCP is around 0.5 mg L^{-1}.
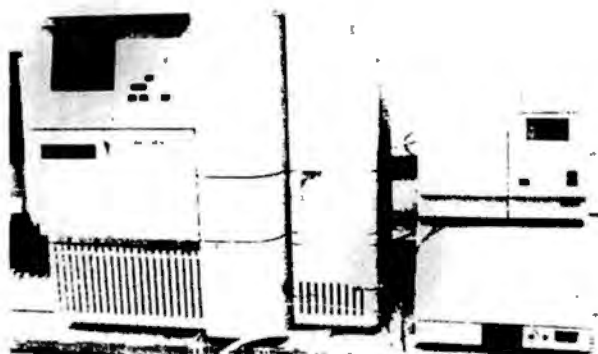
Plate 3.19 A Waters separations module (Waters 2695) comprised with a Waters 996 photodiode array detector.

3.2.6.3 Photocatalytic performances of different photocatalyst

Four kinds of photocatalysts including Bi_2WO_6, $Ag-Bi_2WO_6$, $AgBr-Ag-Bi_2WO_6$ nanojunction and $AgBr-Ag-TiO_2$ prepared in Section 3.2.1 were also used to evaluate the photocatalytic performance of $AgBr-Ag-Bi_2WO_6$ nanojunction on the degradation of PCP. The reaction mixtures for these four photocatalyst were

prepared by adding the corresponding amount of photocatalyst with same amount of VLD component into 50 mL 10 mg L^{-1} PCP solution. The following procedures were the same as described in Sections 3.2.6.1 and 3.2.6.2. The photocatalytic performance of different photocatalyst was also evaluated by the removal efficiency (RE) (%) of PCP, which was calculated in the same way as MX-5B.

3.3 Results

3.3.1 Preparation and characterizations of photocatalysts

Firstly, the Bi_2WO_6 sample was prepared by hydrothermal reaction under the acidic condition according to our recent report (Zhang et al., 2007). As shown in Fig. 3.1A, this sample exhibits flower-like superstructures, which are in fact built from two-dimensional nanoplates with a smooth surface (Fig. 3.1B). After the deposition-precipitation process and subsequent calcination treatment (at 500°C for 3 h), the Bi_2WO_6 superstructures are slightly disintegrated to form clusters of nanoplates (Fig. 3.1C). Interestingly, on the surface of Bi_2WO_6, there are many crystalline with the mean size of 5 nm firmly dispersed after the modified deposition-precipitation process, as demonstrated in TEM image (Fig. 3.1D). The HRTEM image (Fig. 3.1E) of the sample further demonstrates that the lattice spacings of the two fixed components, determined to be 0.375 and 0.333 nm, are in good agreement with the values for the Bi_2WO_6 (111) plane (JCPDF No. 73-1126) and for the cubic AgBr (111) plane (JCPDF No. 79-0149), respectively. It is also observed that the Bi_2WO_6 nanoplate is partially enwrapped in an amorphous nano-shell, where the AgBr crystalline is located beside it.
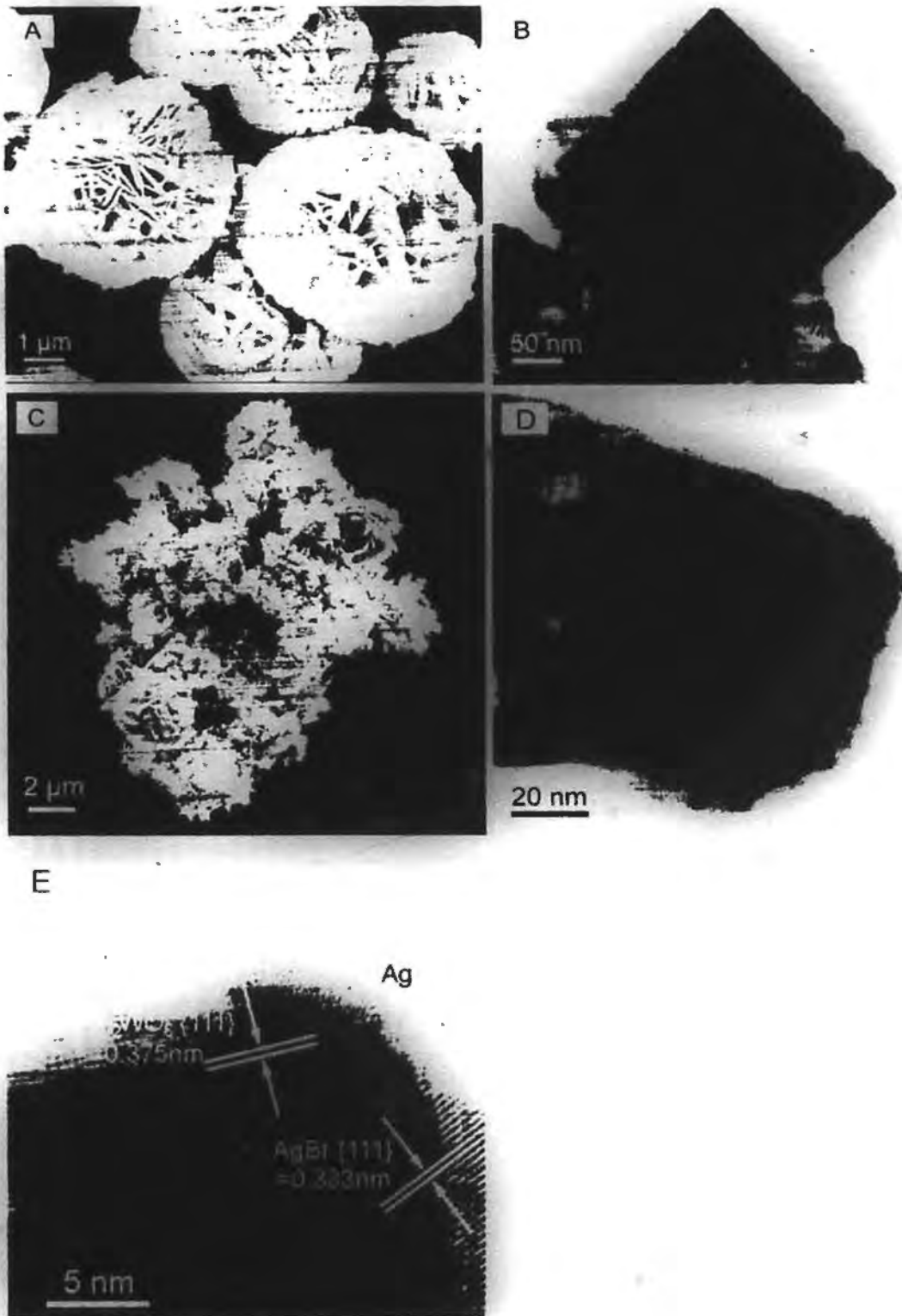
Fig. 3.1 SEM (A) and TEM (B) images of Bi_2WO_6 sample; SEM (C), TEM (D) and HR-TEM (E) images of $AgBr-Ag-Bi_2WO_6$ nanojunction.

The crystalline phases of AgBr-Ag-Bi$_2$WO$_6$ nanojunction and Bi$_2$WO$_6$ samples were investigated by XRD patterns (Figs. 3.2). All samples exhibit diffraction peaks assigned to the orthorhombic Bi$_2$WO$_6$ phase (JCPDF No. 73–1126). In addition, in the AgBr-Ag-Bi$_2$WO$_6$ nanojunction, there are two peaks with 2θ values of 30.94° and 44.33° corresponding to (200) and (220) crystal planes of cubic AgBr (JCPDF No. 79-0149), respectively (Fig. 3.2B). Moreover, the diffraction peak (at 64.4°) assigned to metal Ag is also displayed in the nanojunction (the inset of Fig. 3.2), and it is especially weak, indicating that Ag is poorly crystallized. These results are in good agreement with the HRTEM analysis (Fig. 3.1F). The phase of the used AgBr-Ag-Bi$_2$WO$_6$ nanojunction after the photocatalytic degradation process of MX-5B was also detected in Fig. 3.2. There is very similar between the patterns of the freshly prepared AgBr-Ag-Bi$_2$WO$_6$ nanojunction and the used one.
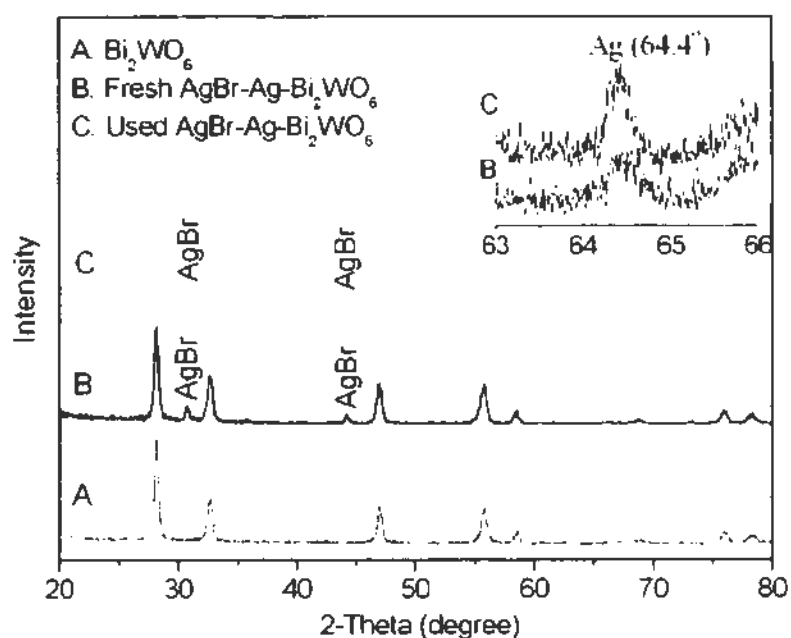
Fig. 3.2 XRD patterns of (A) Bi$_2$WO$_6$, (B) the fresh AgBr-Ag-Bi$_2$WO$_6$ nanojunction, and (C) the used AgBr-Ag-Bi$_2$WO$_6$ nanojunction after photodegradation of MX-5B under visible light irradiation. The insert shows peaks of Ag in the fresh and used AgBr-Ag-Bi$_2$WO$_6$ nanojunction system.

Subsequently, the compositions and the chemical states of its constituent elements was further investigated by EDXA for $AgBr\text{-}Ag\text{-}Bi_2WO_6$ nanojunction system and $AgBr\text{-}Ag\text{-}TiO_2$ composite (Fig. 3.3), and by XPS only for $AgBr\text{-}Ag\text{-}Bi_2WO_6$ nanojunction system (Fig. 3.4).

The EDXA spectrum reveals that besides Bi, W, and O elements derived from the Bi_2WO_6 substrate (Fig. 3.3A), there are only Ag and Br elements in $AgBr\text{-}Ag\text{-}Bi_2WO_6$ nanojunction system. In addition, as shown in Fig. 3.3B, besides Ti and O elements derived from the TiO_2 substrate, there are also only Ag and Br elements in $AgBr\text{-}Ag\text{-}TiO_2$ composite (copper signals appear from the copper grid). These results indicates the presence of AgBr and/or Ag in $AgBr\text{-}Ag\text{-}Bi_2WO_6$ nanojunction system and $AgBr\text{-}Ag\text{-}TiO_2$ composite. The atomic ratio of Ag: Br: W: Bi in the $AgBr\text{-}Ag\text{-}Bi_2WO_6$ nanojunction system and Ag: Br: Ti in $AgBr\text{-}Ag\text{-}TiO_2$ composite can be obtained by the EDXA analysis, which are 1.53: 0.83:6.75:14.69 and 0.92: 0.59:48.89, respectively. To estimate the quantitative amount of components in these two samples according to the EDXA data, it is discovered that, the weight percentages of Ag and AgBr components in $AgBr\text{-}Ag\text{-}Bi_2WO_6$ nanojunction system are 1.48% and 3.04%, respectively, which is a little larger than those in $AgBr\text{-}Ag\text{-}TiO_2$ composite (0.874 and 2.74%, respectively) as shown in Table 2.1.
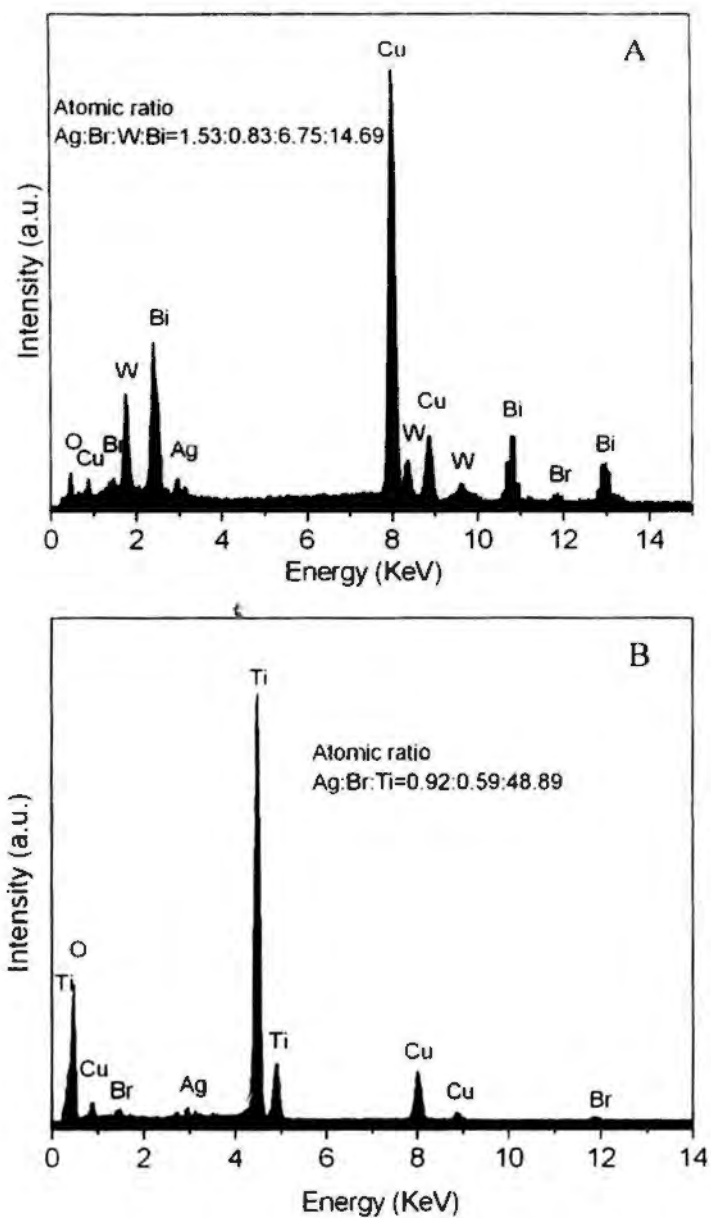
Fig. 3.3 EDXA spectra of AgBr-Ag-Bi$_2$WO$_6$ nanojunction system and AgBr-Ag-TiO$_2$ composite.

Table 3.1 Weight percentages (%) of each component in the catalysts.

	Ag	AgBr	Bi$_2$WO$_6$ or TiO$_2$
AgBr-Ag-Bi$_2$WO$_6$	1.48	3.04	95.5
AgBr-Ag-TiO$_2$	0.874	2.74	96.4

Fig. 3.4 shows the high-resolution XPS spectra of the Ag 3d and Br 3d regions in AgBr-Ag-Bi$_2$WO$_6$ nanojunction. The Ag 3d$_{3/2}$ and Ag 3d$_{5/2}$ peaks are identified at 374.0 and 368.0 eV, respectively, suggesting the presence of metal Ag (Fig. 3.4A) (Hu et al., 2006). Moreover, the peak of Br 3d at 68.9 eV is due to the crystal lattice of Br in AgBr (Fig. 3.4B) (Moulder et al., 1992). These results further confirm the presence of both Ag and AgBr species in the nanojunction.
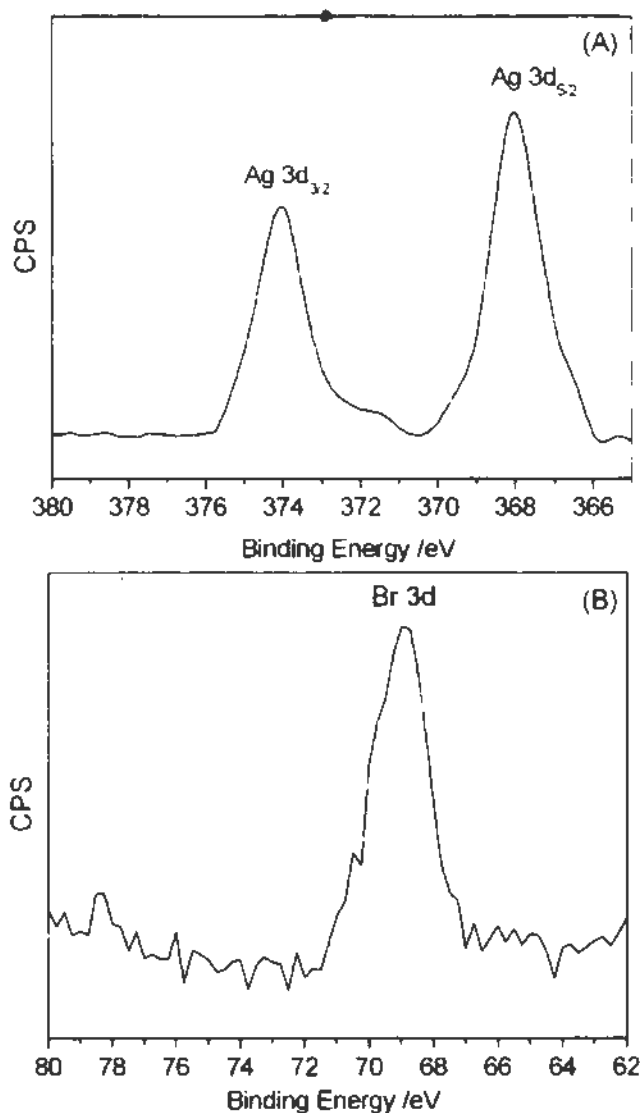
Fig. 3.4 Ag 3d (A) and Br 3d (B) XPS spectra of AgBr-Ag-Bi$_2$WO$_6$ nanojunction.

The optical absorptions of the Bi_2WO_6 sample and $AgBr-Ag-Bi_2WO_6$ nanojunction system were measured using an UV-VIS spectrometer (Fig. 3.5). The Bi_2WO_6 sample exhibits strong photoabsorption from the UV light region to visible light shorter than 470 nm as shown in Fig. 3.5, corresponding to the indirect band gap of Bi_2WO_6 (Zhang et al., 2007). Importantly, aside from the photoabsorption from Bi_2WO_6, the $AgBr-Ag-Bi_2WO_6$ nanojunction displays another wide, yet weak absorption band around 450-700 nm, corresponding to the indirect band gap of AgBr and surface plasmon absorption of metal Ag (Hu et al., 2006).
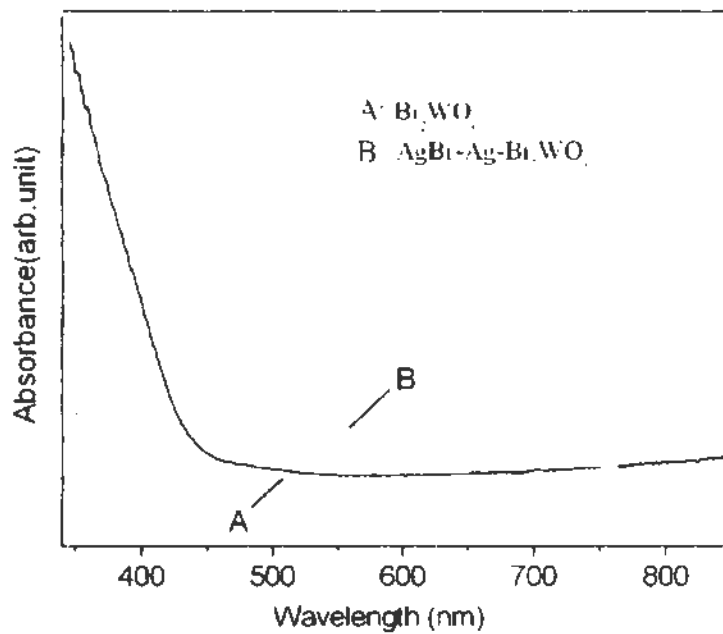
Fig. 3.5 UV-VIS diffuse reflectance spectra of (A) Bi_2WO_6 sample and (B) $AgBr-Ag-Bi_2WO_6$ nanojunction.

The surface charge of AgBr-Ag-Bi$_2$WO$_6$ nanojunction at different pH values was investigated by zeta potential test as shown in Fig. 3.6. The pH values I chose in this experiment were 3.0, 3.7, 5.2, 7.13, 8.48, 9.6 and 10.37. As a result, it is found that the surface charge of AgBr-Ag-Bi$_2$WO$_6$ nanojunction in the aqueous solutions goes forward from positive to negative with the increase of pH value from 3.0 to 10.37. And the zero point of charge (3.7) is obtained from the plotted curve in Fig.3.6. Thus, when the AgBr-Ag-Bi$_2$WO$_6$ nanojunction is in an aqueous suspension, the more acidic of the solution, the more positive charges on the surface are, if the pH value of the solution is smaller than 3.7. In contrast, if the pH value is larger than 3.7, the amount of negative charges on the surface goes up with the increase of pH value.
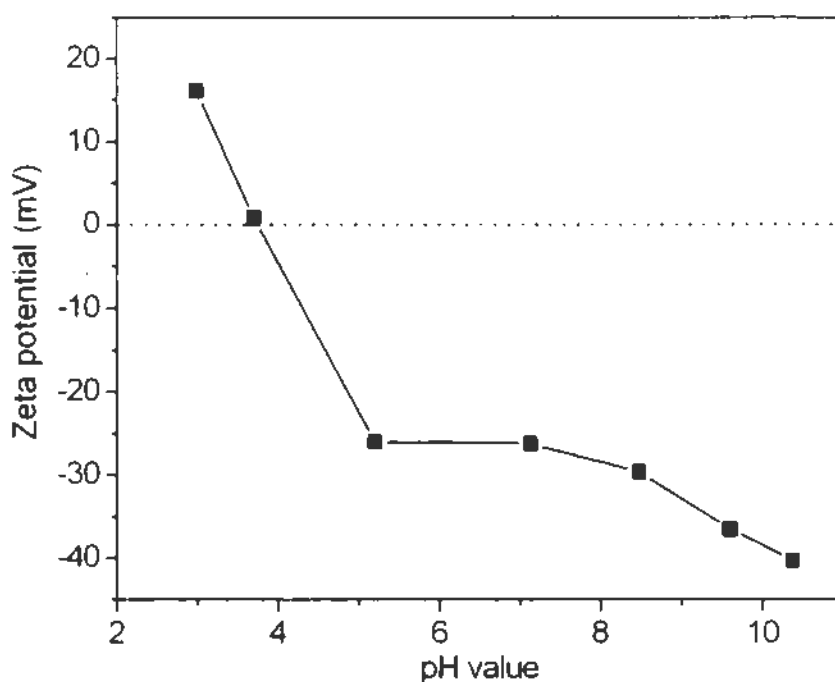
Fig.3.6 Zeta potentials for a suspension containing 0.05 g L^{-1} of AgBr-Ag-Bi$_2$WO$_6$ nanojunction in the presence of KNO$_3$ (10^{-4} M) at different pH values.

3.3.2 Photocatalytic degradation of MX-5B

3.3.2.1 Photocatalytic degradation performances

MX-5B was chosen as a representative pollutant to evaluate the photocatalytic performance of photocatalysts. When dissolved in distilled water, MX-5B displays a major absorption band centered at 538 nm that is used to monitor its photocatalytic degradation. Fig. 3.7 shows adsorption and photodegradation of MX-5B by different photocatalysts containing the same weight of each visible-light-active component under visible light irradiation ($\lambda \geq 400$ nm). As a comparison, MX-5B degradation without photocatalysts was also performed, and the results demonstrate that the amount of MX-5B remained constant in the absence of photocatalyst under visible-light irradiation (Fig. 3.7A), indicating that the MX-5B is resistant to the visible light. The AgBr-Ag-TiO$_2$ composite absorbed about 7.5% of MX-5B in dark after 60 min, while the others similarly exhibit weaker adsorption abilities as shown in Fig. 3.7. In the subsequent photocatalytic process, it is observed that the removal of MX-5B only reached 4% when using the Bi$_2$WO$_6$ superstructures with single visible-light active component as photocatalyst after 60 min of reaction time (Fig. 3.7 B), while the photocatalytic degradation efficiency of MX-5B was elevated to about 6% in the presence of Ag in Bi$_2$WO$_6$ superstructures (Fig. 3.7C). When AgBr-Ag-TiO$_2$ composite with AgBr as single visible-light active component was used as the photocatalyst, the photocatalytic degradation efficiency of MX-5B reached 61% after 60 min under visible light irradiation (Fig. 3.7D). Surprisingly, by AgBr-Ag-Bi$_2$WO$_6$ nanojunction with two visible-light active components (AgBr and Bi$_2$WO$_6$) and an electron transfer system (Ag), the MX-5B could be photocatalytically degraded 83% within 60 min under visible light irradiation, indicating the highest photocatalytic activity of AgBr-Ag-Bi$_2$WO$_6$ nanojunction (Fig.

54

3.7E). Based on the above results, it is deduced that each component in the AgBr-Ag-Bi$_2$WO$_6$ nanojunction is crucial for its excellent photocatalytic activity.
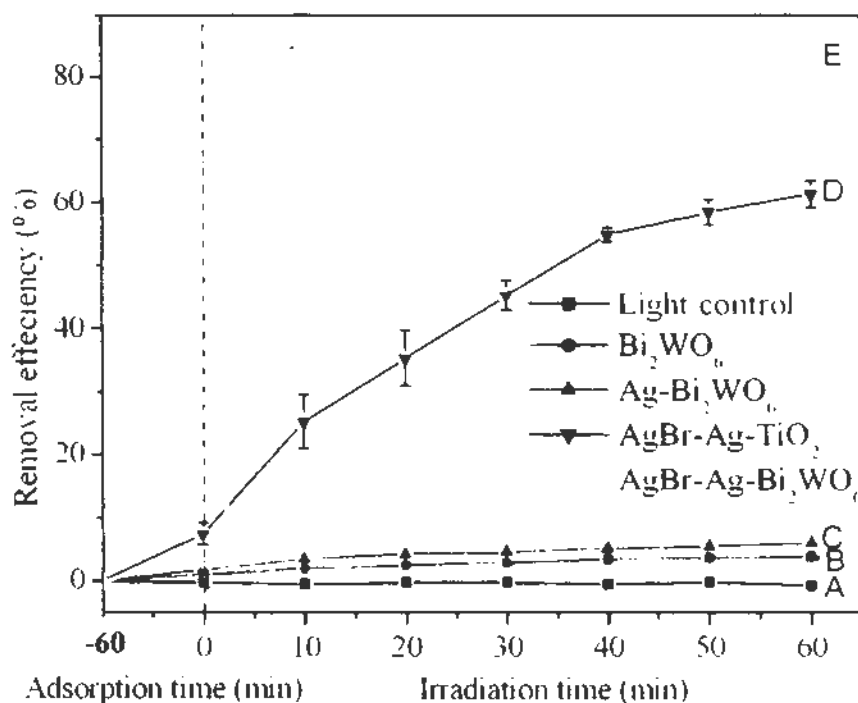
Fig. 3.7 The photodegradation efficiencies of MX-5B (50 mg L^{-1}, 100 mL) by different photocatalysts with same weight of each VLD component under visible light: (A) Light control, (B) 47.8 mg Bi$_2$WO$_6$, (C) 48.5 mg Ag-Bi$_2$WO$_6$ containing 47.8 mg Bi$_2$WO$_6$, (D) 55.6 mg AgBr-Ag-TiO$_2$ composites containing 1.52 mg AgBr, and (E) 50 mg AgBr-Ag-Bi$_2$WO$_6$ nanojunction containing 1.52 mg AgBr and 47.8 mg Bi$_2$WO$_6$. Each data point and error bar represents the mean and the standard deviations of independent triplicates respectively.

In order to further investigate the photocatalytic mineralization of MX-5B, Fig. 3.8 illustrates the TOC removal efficiency, and formation of CO$_2$ and inorganic carbon (IC: HCO$_3^-$ and CO$_3^{2-}$) during the degradation of MX-5B by AgBr-Ag-Bi$_2$WO$_6$ nanojunction under visible light irradiation. TOC removal efficiency increased to 61% after 28 h, companying steady increase of the amount of evolved CO$_2$ and the

concentration of IC in the solution as shown in Fig. 3.8. With prolonged irradiation time (>34 h), TOC content of the solution could not be reduced further because the triazine group of MX-5B is converted to cyanuric acid which is very stable in photocatalytic process (So et al., 2002).
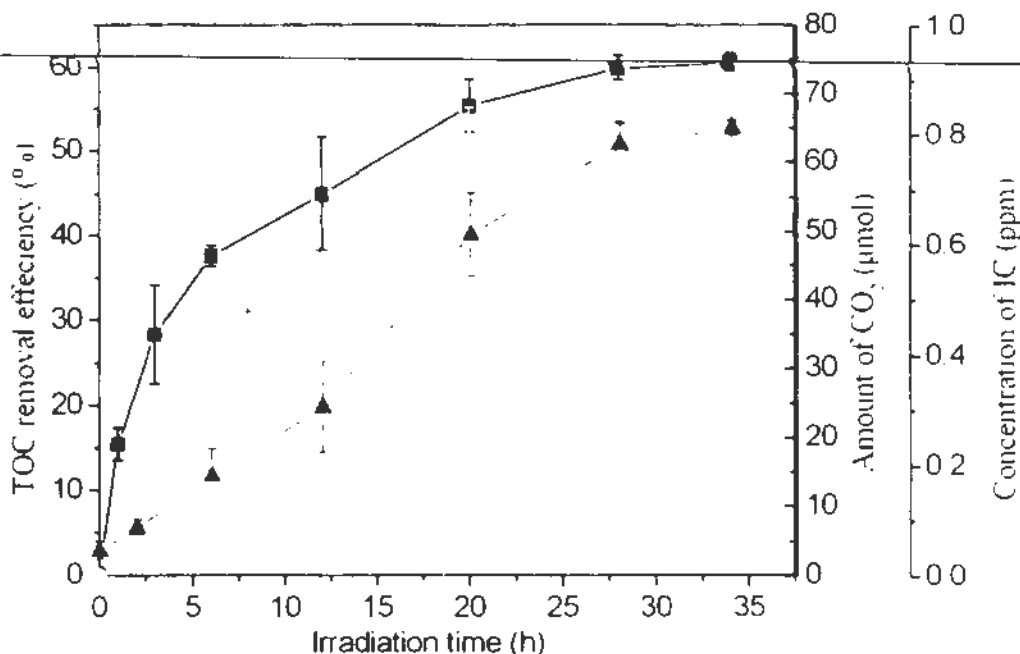
Fig. 3.8 The TOC removal efficiency, the evolved CO_2 amount and IC concentration during the photocatalytic degradation of MX-5B (40 mg L^{-1}, 200 mL) by 0.4 g AgBr-Ag-Bi_2WO_6 nanojunction under visible light irradiation. Each data point and error bar represents the mean and the standard deviations of independent triplicates respectively.

3.3.2.2 Factors affecting degradation efficiency of MX-5B

The initial concentrations of MX-5B for this study were 10, 20, 40, 60 and 80 mg L^{-1}. Fig. 3.9 demonstrates the effect of the initial concentrations of MX-5B on the photocatalytic degradation efficiencies of MX-5B. When the concentration of MX-5B was 10 mg L^{-1}, about 95.9% MX-5B were degraded within 60 min by AgBr-Ag-Bi_2WO_6 nanojunction under visible light irradiation. When the

concentrations of MX-5B gradually increased to 20, 40, 60 and 80 mg L^{-1}, the photocatalytic degradation efficiencies of MX-5B dropped to 84.7, 78.4, 73.0 and 62.1%, respectively.
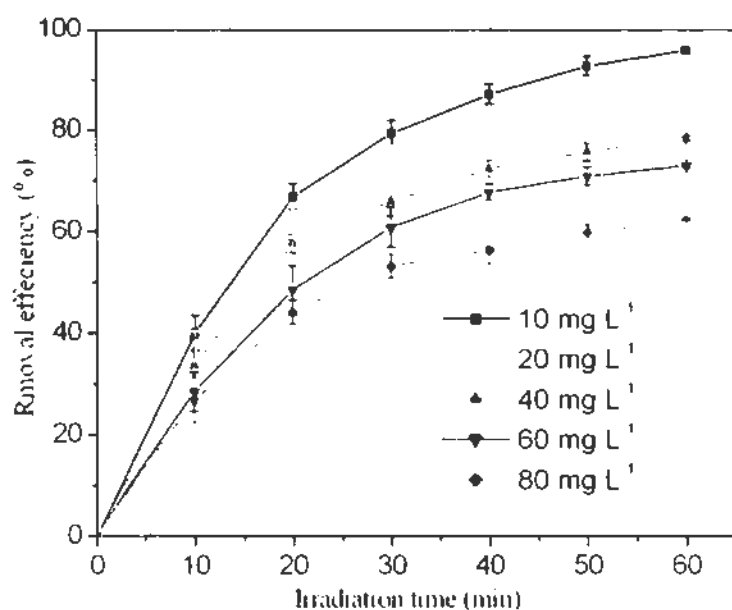
Fig. 3.9 The photocatalytic degradation of MX-5B (50 mg L^{-1}, 100 mL) by 25 mg AgBr-Ag-Bi$_2$WO$_6$ nanojunction under visible light at various initial concentrations. Each data point and error bar represents the mean and the standard deviations of independent triplicates respectively.

In order to investigate the pH effect, in this experiment, the initial pH value of the suspension containing the photocatalyst and MX-5B was adjusted by adding a few drops of 1 M HCl or 1 M NaOH. The range of pH tested for the study was pH 3.0±0.2, 5.0±0.2, 7.0±0.2 and 9.0±0.2. Fig. 3.10 displays the effects of initial pH value of solutions on photocatalytic degradation efficiencies of MX-5B with AgBr-Ag-Bi$_2$WO$_6$ nanojunction system as a photocatalyst.
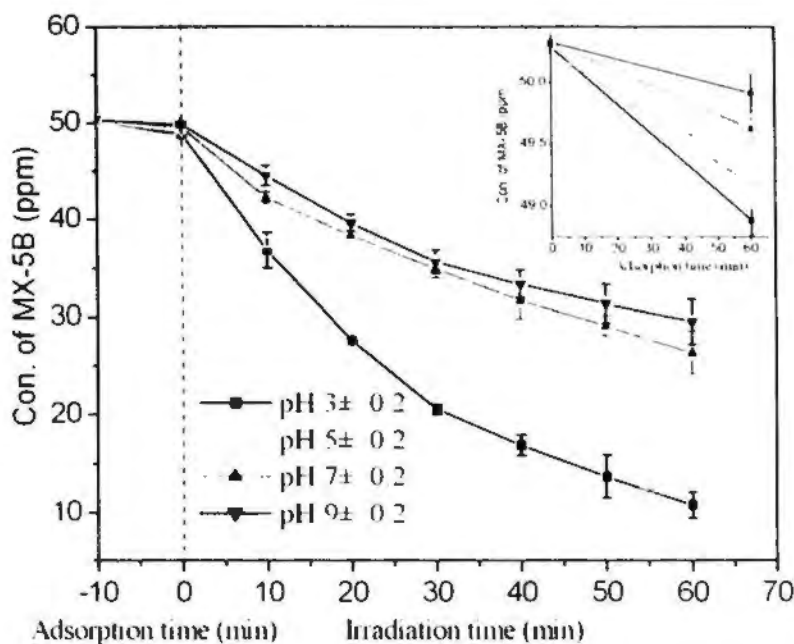
Fig. 3.10 The photodegradation of MX-5B (50 mg L^{-1}, 100 mL) in aqueous solutions with different initial pH value, containing 25 mg AgBr-Ag-Bi$_2$WO$_6$ nanojunction under visible light irradiation. The effect of pH on the adsorption of MX-5B is shown in the inset of figure. Each data point and error bar represents the mean and the standard deviations of independent triplicates respectively.

When pH value was 3±0.2, 40 mg L^{-1} MX-5B were photocatalytically degraded after 60 min of visible-light irradiation. With the increase of the initial pH value from 3±0.2 to 9±0.2, the photocatalytic degradation rate of MX-5B significantly decreased. And the concentrations of MX-5B remaining in the reaction mixture at initial pH values of 5±0.2, 7±0.2, and 9±0.2 after 60-min photocatalytic oxidation (PCO) treatment were 18.6, 26.4, and 29.5 mg L^{-1}. Since the adsorption of dye molecules onto the catalyst surfaces is an important step for PCO to take place, we further examined the relationship between pH value of the suspension and the adsorption of MX-5B, as shown in the inset of Fig. 3.10. The average adsorption of MX-5B on the AgBr-Ag-Bi$_2$WO$_6$ nanojunction surface at initial pH values of 3±0.2, 7±0.2, 5±0.2 and 9±0.2 were 1.4, 1.1, 0.7 and 0.4 mg L^{-1}, which indicates the adsorption capacity

of the photocatalyst in the reaction mixture increases with the decrease of the initial pH value These results reveal the similar trend between the photocatalytic degradation rate of MX-5B during the PCO process and the adsorption amount of MX-5B on AgBr-Ag-Bi$_2$WO$_6$ nanojunction before the PCO treatment when the initial pH values of the reaction mixture are different.

3.3.2.3 The stability of the AgBr-Ag-Bi$_2$WO$_6$ nanojunction

In order examine the stability of the AgBr-Ag-Bi$_2$WO$_6$ nanojunction under visible light, the cycling runs in the photocatalytic degradation of MX-5B was conducted as shown in Fig. 3.11. It should be noted that since the AgBr-Ag-Bi$_2$WO$_6$ nanojunction are microsized clusters, they were easily recycled by simple filtration or centrifugation without any treatment in these experiments. The freshly prepared AgBr-Ag-Bi$_2$WO$_6$ nanojunction removed 94% MX-5B in the reaction mixture after 100 min under visible light as shown in the first cycle in Fig. 3.11. When these reused AgBr-Ag-Bi$_2$WO$_6$ nanojunctions were employed as the photocatalyst, 89% MX-5B were photocatalytically degraded in the second cycle. In the third, fourth, and fifth cycle, the used the AgBr-Ag-Bi$_2$WO$_6$ nanojunction still could photocatalytically degrade 92%, 93% and 90% of MX-5B, respectively under the other identical conditions (Fig. 3.11), indicating that even after five cycles of the photocatalytic degradation process of MX-5B, the AgBr-Ag-Bi$_2$WO$_6$ nanojunction did not exhibit any significant loss of activity.
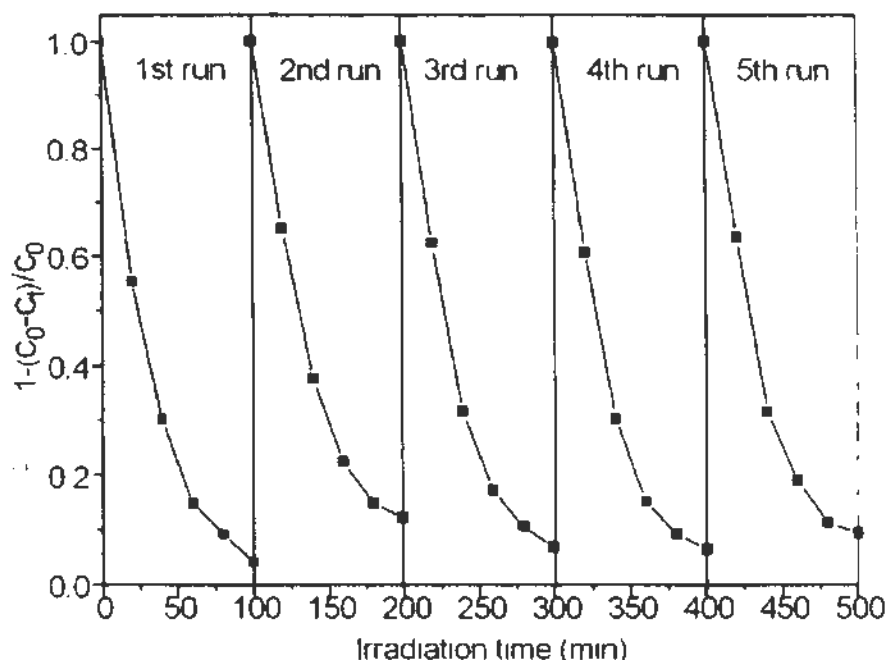
Fig. 3.11 Cycling runs in the photodegradation of MX-5B (50 mg L^{-1}, 100 mL) in aqueous dispersions containing 50 mg of AgBr-Ag-Bi$_2$WO$_6$ nanojunction under visible light illumination.

3.3.3 The photocatalytic degradation of PCP

In this study, other organic pollutant, PCP was also employed to evaluate the photocatalytic activities of AgBr-Ag-Bi$_2$WO$_6$ nanojunction. Fig. 3.12 demonstrates the photocatalytic degradation of PCP by different photocatalysts containing the same weight of each visible-light-active component under visible light irradiation ($\lambda \geq 400$ nm) as well as the removal efficiency of PCP without photocatalyst under visible light. Obviously, the amount of PCP remained constant under visible light illumination, indicating the fact that it is also resistant to the visible light. The AgBr-Ag-Bi$_2$WO$_6$ nanojunction degraded 62% of PCP in the reaction mixture after 60 min under visible light (Fig. 3.12). While the AgBr-Ag-TiO$_2$ composites with the AgBr as the visible-light active component only degraded 33% of PCP. Although,

the $Ag-Bi_2WO_6$ and Bi_2WO_6 can degrade PCP under visible light illumination, very low photocatalytic degradation efficiencies were achieved as shown in Fig. 3.12.
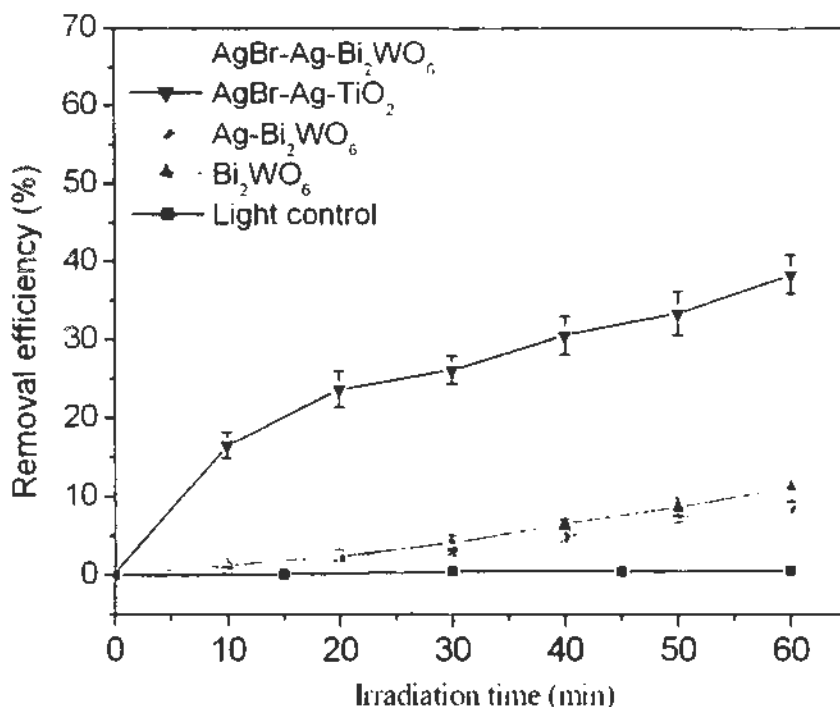
Fig. 3.12 The photodegradation of PCP (10 mg L^{-1}, 50 mL) in aqueous dispersions under visible light containing photocatalysts with same weight of each VLD component: Light control; 9.55 mg Bi_2WO_6; 9.7 mg $Ag-Bi_2WO_6$ containing 9.55 mg Bi_2WO_6; 11.1 mg $AgBr-Ag-TiO_2$ composites containing 0.304 mg AgBr; 10 mg $AgBr-Ag-Bi_2WO_6$ nanojunction containing 0.304 mg AgBr and 9.55 mg Bi_2WO_6. Each data point and error bar represents the mean and the standard deviations of independent triplicates respectively.

3.3.4 The photocatalytic mechanism investigation

More importantly, for both MX-5B and PCP degradation, it is discovered that pollutant degradation efficiencies by $AgBr-Ag-Bi_2WO_6$ nanojunction were 85 and 62% after 60-min treatment under visible light illumination, respectively, which were higher than the total degradation efficiencies by two individual photocatalysts ($AgBr-Ag-TiO_2$ and Bi_2WO_6) containing same weight of the visible-light-active

component ($AgBr$ or Bi_2WO_6) (67.2 % for MX-5B and 46.4 % for PCP), as shown in Fig. 3.13. This result reveals that there should be synergic effect between the two-visible-light-active components ($AgBr$ and Bi_2WO_6) in $AgBr$-Ag-Bi_2WO_6 nanojunction.
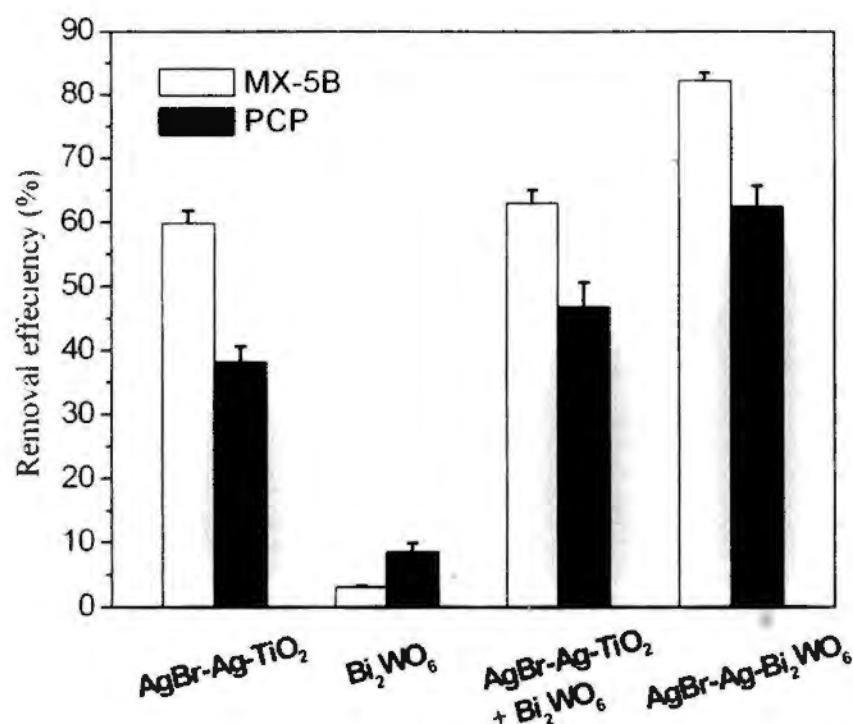
Fig. 3.13 The comparison of photocatalytic degradation efficiencies of MX-5B and PCP by different photocatalysts containing the same weight of each visible-light active component ($AgBr$ or Bi_2WO_6) after 60 min under visible light irradiation. Each data point and error bar represents the mean and the standard deviations of independent triplicates respectively.

3.4 Discussion

3.4.1 Preparation and characterization of catalysts

As shown in Figs. 2.1D and E, Ag and tiny $AgBr$ nanoparticles are deposited onto the Bi_2WO_6 substrate by impregnating the aqueous solution of $AgNO_3$ and NH_4OH to the aqueous solution containing Bi_2WO_6 substrate and CTAB via the modified

deposition-precipitation process (Hu et al., 2006; Elahifard et al., 2007). In this process, at alkaline condition, cationic surfactant CTAB can be adsorbed onto the surface of Bi_2WO_6 to limit the number of nucleation sites for AgBr to grow, leading to homogeneously dispersed AgBr islands with about 5 nm diameters on the Bi_2WO_6 nanoplate substrate (Fig. 3.1D). Aside from this, CTAB supplies bromide to precipitate Ag^+ in solution; however, it should be noted that metal Ag formation occurs accompanying the formation of AgBr (Hu et al., 2006; Elahifard et al., 2007). Thus, it is deduced that the amorphous nanoshell that partially enwraps Bi_2WO_6 nanoplate and AgBr crystalline as displayed in Fig. 3.1E should be metal Ag.

The XRD results indicate there are only three phase existing independently in the nanojunction sample including well crystallized AgBr and Bi_2WO_6, poor crystallized metal Ag, which further reveals that the amorphous nanoshell observed in TEM images (Fig. 3.1E) should be metal Ag.

For the analysis of the compositions and the chemical state of its constituent elements, both EDXA and XPS technologies were employed. EDXA yields the composition of the material within a region approximately 1 μm below the surface, relying on the penetration depth of electrons with relatively high energy (Tierno and Goedel, 2006). So EDXA contains information both due to the nanoplate surface and the core of the sample clusters. Thus the quantitative amount of components in the nanojunction sample can be estimated according to the fraction of the elemental composition obtained from the EDXA analysis as shown in Table 1.1. As a result, beside the Bi_2WO_6, there are only 1.48% Ag and 3.04% AgBr components existing in the $AgBr-Ag-Bi_2WO_6$ nanojunction sample. On the other hand, XPS only reveals information on the topmost few angstroms of the surface since it is based on the limited escape depth of electrons with relatively low energy (Tierno and Goedel,

2006). So, it is appropriate for detecting valency states of elements on the surface and the results reveal that metal Ag, Ag^+ and Br^- are present on the surface of the nanojunction sample.

Therefore, based on the TEM, EDXA, XPS and XRD results the construction of an $AgBr-Ag-Bi_2WO_6$ nanojunction including Ag nanoshell, tiny AgBr nanoparticles and Bi_2WO_6 nanoplate substrate is well established.

The detection of the optical absorptions further indicates that the region of visible light photo-response can be broadened by the conjunction of photoabsorption of visible-light active components, AgBr and Bi_2WO_6 in the $AgBr-Ag-Bi_2WO_6$ nanojunction system (Fig. 3.5). Thus, VLD photocatalytic performance of $AgBr-Ag-Bi_2WO_6$ nanojunction is expected to be excellent compared with that of photocatalyst with single visible-light active component such as Bi_2WO_6 and $AgBr-Ag-TiO_2$.

3.4.2 Photocatalytic degradation of MX-5B

3.4.2.1 Photocatalytic performances

MX-5B is a common monoazo dye widely used in dyeing cellulose, nylon, silk and wool. Due to the highly stability of aromatic dye molecules of azo dye, traditional biological and chemical methods often failed to degrade them (So et al., 2002). Of course, MX-5B can not be removed in the absence of photocatalyst with input of the low energy of visible light (Fig. 3.7A). P25 (TiO_2) have particles size about 30 nm and it have higher BET surface about 50 m^2 g^{-1} than Bi_2WO_6 substrate (Zhang et al., 2007). It is reasonable that the $AgBr-Ag-TiO_2$ composites possess larger adsorption capacity for MX-5B than Bi_2WO_6 based composite such as $AgBr-Ag-Bi_2WO_6$ nanojunction.

Recently, we have revealed that Bi_2WO_6 superstructures exhibit good photocatalytic activities under visible-light illumination for the degradation of Rhodamine B (RhB) (Zhang et al., 2007). However, the single phased Bi_2WO_6 superstructures have very low photocatalytic performance on the degradation of MX-5B due to its high stability. Since the junction of metal Ag can improve the electron-hole separation and interfacial charge transfer (Liu et al., 2004; Tada et al., 2006; Hu et al., 2006), $Ag-Bi_2WO_6$ sample shows an elevated photocatalytic activity. The $AgBr-Ag-TiO_2$ composite also has a better photocatalytic performance on the degradation of MX-5B under visible light because this composite contains 2.74% of AgBr (Table 3.1). AgBr is a kind of good VLD photocatalyst but is very unstable when it is used alone under visible light (Hu et al., 2006). Due to the presence of two visible-light active components (Bi_2WO_6 and AgBr) and an electron transfer component (Ag), the $AgBr-Ag-Bi_2WO_6$ nanojunction system exhibits the highest photocatalytic activity.

Previous studies shows that in the presence of photocatalysts (such as TiO_2), some organic dyes that can absorb visible light could be degraded by sensitization mechanism (Nasr et al., 1996; Vinodgopal et al., 1996; Yan et al., 2006), because the excited electrons of these dyes can inject into the conduction band of photocatalysts and subsequently these organic dyes are oxidized. In this case, however, the lowest unoccupied molecular orbital (LUMO) of MX-5B (-0.9 V versus NHE) (Liu et al., 2005) is more positive than the potential of conduction band of AgBr (-1.04 V versus NHE) (Belloni et al., 1999), thus the excited electrons of dye are thermodynamically unfavorable to transfer to AgBr. Although the LUMO of MX-5B is more negative than the potential of conduction band of Bi_2WO_6 (-0.07 V versus NHE) (Zhao et al., 2007), the Bi_2WO_6 shows a poor activity for the degradation of MX-5B as shown in

Fig. 3.7B, which indicates that the charge injection from the MX-5B to the Bi_2WO_6 is inefficient. Moreover, MX-5B can be steadily mineralized by $AgBr-Ag-Bi_2WO_6$ nanojunction and the loss of TOC is transformed to gaseous CO_2 and/or inorganic carbon in solution (Fig. 3.8), which further confirms that effectively photocatalytic degradation of MX-5B by $AgBr-Ag-Bi_2WO_6$ (Fig. 3.7E) are mainly derived from the direct band gap excitation instead of sensitization mechanism.

In addition, the degradation rate by $AgBr-Ag-Bi_2WO_6$ nanojunction is much higher than that by $AgBr-Ag-TiO_2$ composite within the 20 min (Figs. 3.7 D and E). The subsequent degradation rate of MX-5B by $AgBr-Ag-Bi_2WO_6$ nanojunction system decreases due to the following two reasons. Firstly, the concentration of MX-5B goes down, thus the vanishing rate reduces kinetically. Secondly, the intermediates formed upon PCO of the parental dye, such as aromatics, aldehydes, ketones and organic acids as shown by previous studies (Serpone et al., 1993; Tanaka et al., 2000), compete with the micro-molecular MX-5B in the degrading reaction.

3.4.2.2 Factors affecting degradation efficiency of MX-5B

In the range of the concentrations of MX-5B investigated in this study, the photocatalytic degradation rate decreases with the increase of initial dye concentration. One possible reason is the visible light-screening effect of the dye itself. At a high dye concentration, a significant amount of visible light may be absorbed by the dye molecules rather than the $AgBr-Ag-Bi_2WO_6$ nanojunction particles, which reduces the efficiency of the catalytic reaction. Another possible reason is the interference from intermediates formed during the photocatalytic oxidation process. They may compete with the dye molecules for the limited adsorption and catalytic sites on the photocatalytic particles (Serpone et al., 1993)

and thus inhibit decolorization. Such suppression would be even more pronounced in the presence of an elevated level of degradation intermediates formed upon an increased initial dye concentration.

The pH value can significantly affect the degradation efficiencies of MX-5B during the PCO process via varying the adsorption of MX-5B by the $AgBr-Ag-Bi_2WO_6$ (Fig. 3.9). Previous studies reveal that the adsorption and photodegradation of dye pollutants are pH-dependent, chiefly resulting from the variation of surface charge of catalysts with pH (Fu et al., 2005). As demonstrated by the zeta potential of $AgBr-Ag-Bi_2WO_6$ nanojunction in the aqueous solution with different pH values (Fig. 3.6), the surface charges on the surface of $AgBr-Ag-Bi_2WO_6$ nanojunction are determined by the pH value of the solution. The surface charge is positive when pH <3.7, and it becomes more negative with higher pH value when pH >3.7. In addition, the charge of MX-5B in aqueous solution is negative due to the presence of $-SO_3^-$ group (Fig. 1.2). Thus, electrostatic repulsion between the dye molecules and $AgBr-Ag-Bi_2WO_6$ nanojunction goes down with the decrease of pH from 9 to 3, resulting in the improvement of the adsorption and photodegradation of MX-5B.

3.4.2.3 The stability of the $AgBr-Ag-Bi_2WO_6$ nanojunction

The cycling runs in the photocatalytic degradation of MX-5B mediated by $AgBr-Ag-Bi_2WO_6$ nanojunction under visible light irradiation confirms the stability of the $AgBr-Ag-Bi_2WO_6$ nanojunction in VLD photocatalytic process, as shown in Fig. 3.11, revealing that the components of the $AgBr-Ag-Bi_2WO_6$ nanojunction is not photo-corroded and the nanojunction structure is stable during the photocatalytic process. XRD patterns of the $AgBr-Ag-Bi_2WO_6$ nanojunction before (Fig. 3.2B) and

after (Fig. 3.2C) photocatalytic reaction also show that the crystal structure of different components have no obvious changes. Although the single AgBr component is usually unstable under visible light irradiation, AgBr in the nanojunction is not destroyed during the photocatalytic process, which results from the fact that the presence of metal Ag can inhibit the decomposition of AgBr under visible light irradiation (Hu et al., 2006; Elahifard et al., 2007). Therefore, the as prepared $AgBr-Ag-Bi_2WO_6$ nanojunction is an effective and stable VLD photocatalyst.

3.4.3 The photocatalytic degradation of PCP

The PCP is a kind of colorless compound, having the different properties compared with the MX-5B, and its molecular structure is displayed in Fig. 1.3. However, in the similar pattern with the photocatalytic degradation of MX-5B, $AgBr-Ag-Bi_2WO_6$ nanojunction exhibits the highest photocatalytic performance on the degradation of the PCP among the photocatalysts employed in this study.

3.4.4 The photocatalytic mechanism

The electronic structures and energy band of visible-light-response components, AgBr and Bi_2WO_6 are widely studied by researchers (Belloni et al., 1999; Hu et al., 2006; Zhao et al., 2007). On the basis of their energy band diagram, the photocatalytic process of $AgBr-Ag-Bi_2WO_6$ nanojunction can be proposed, as shown in Fig. 3.14. Since both AgBr and Bi_2WO_6 can be excited by visible light and have different photoabsorption ranges, the conjunction of their photoabsorption can enhance the utilization of visible light and broaden the range of visible light photo-response. The photocatalytic reaction is initiated by the absorption of visible light photons with energy equal or higher than the band-gap in either AgBr or

Bi_2WO_6 semiconductors, which results in the creation of photogenerated holes in its valence band (VB) and electrons in its conduction band (CB). On one hand, CB-electrons (Bi_2WO_6) easily flow into metal Ag (electron transfer I: $Bi_2WO_6 \rightarrow$ Ag) through the Schottky barrier because the CB (or the Fermi level) of Bi_2WO_6 is higher than that of the loaded metal Ag, which is consistent with the previous study on electron transfer from semiconductor (Such as TiO_2) to metal (Such as Ag and Au) (Liu et al., 2004; Subramanian et al., 2004; Hirakawa and Kamat, 2005; Tada et al., 2006). This process of electron transfer I is faster than the electron-hole recombination between the VB and CB of Bi_2WO_6. Thus, plenty of CB-electrons (Bi_2WO_6) can be stored in Ag component, as similar with the previous study (Subramanian et al., 2004; Hirakawa and Kamat, 2005). As a result, more VB-holes (Bi_2WO_6) with a strong oxidation power escape from the pair recombination and are available to oxidize the pollutants or OH^-, which explains the reason why the Ag-Bi_2WO_6 sample exhibits higher photocatalytic activity than the pure Bi_2WO_6 sample for the destruction of organic pollutant, as demonstrated in Fig. 3.7 and Fig. 3.12. On the other hand, since the energy level of Ag is above the VB of AgBr, VB-holes (AgBr) also easily flow into metal Ag (electron transfer II: Ag $\rightarrow$ AgBr), which is faster than the electron-hole recombination between the VB and CB of AgBr. Thus, more CB-electrons (AgBr) with a strong reduction power can escape from the pair recombination and are available to reduce some absorbed compounds (such as O_2 and H^+, etc.). Therefore, simultaneous electron transfer I and II (that is, vectorial electron transfer of $Bi_2WO_6 \rightarrow$ Ag $\rightarrow$ AgBr) should occur as a result of visible-light excitation of both Bi_2WO_6 and AgBr, which is similar to the report on the CdS-Au-TiO_2 three-component nanojunction system (the vectorial electron transfer of $TiO_2 \rightarrow$ Au $\rightarrow$ CdS) (Tada et al., 2006). In this vectorial electron transfer process, metal Ag in AgBr-Ag-Bi_2WO_6 nanojunction system act as a storage and/or

recombination center for CB-electrons (Bi$_2$WO$_6$) and VB-holes (AgBr) and contributes to enhancing interfacial charge transfer and realizing the complete separation of VB-hole (Bi$_2$WO$_6$) and CB-electrons (AgBr). So this Z-scheme of AgBr-Ag-Bi$_2$WO$_6$ nanojunction can simultaneously and efficiently generate VB-holes (Bi$_2$WO$_6$) with a strong oxidation power and CB-electrons (AgBr) with a strong reduction power, explaining the high photocatalytic activity of the AgBr-Ag-Bi$_2$WO$_6$ nanojunction system compared with the sum of that of two photocatalysts (Bi$_2$WO$_6$ and AgBr-Ag-TiO$_2$), as proven in Fig. 3.13.
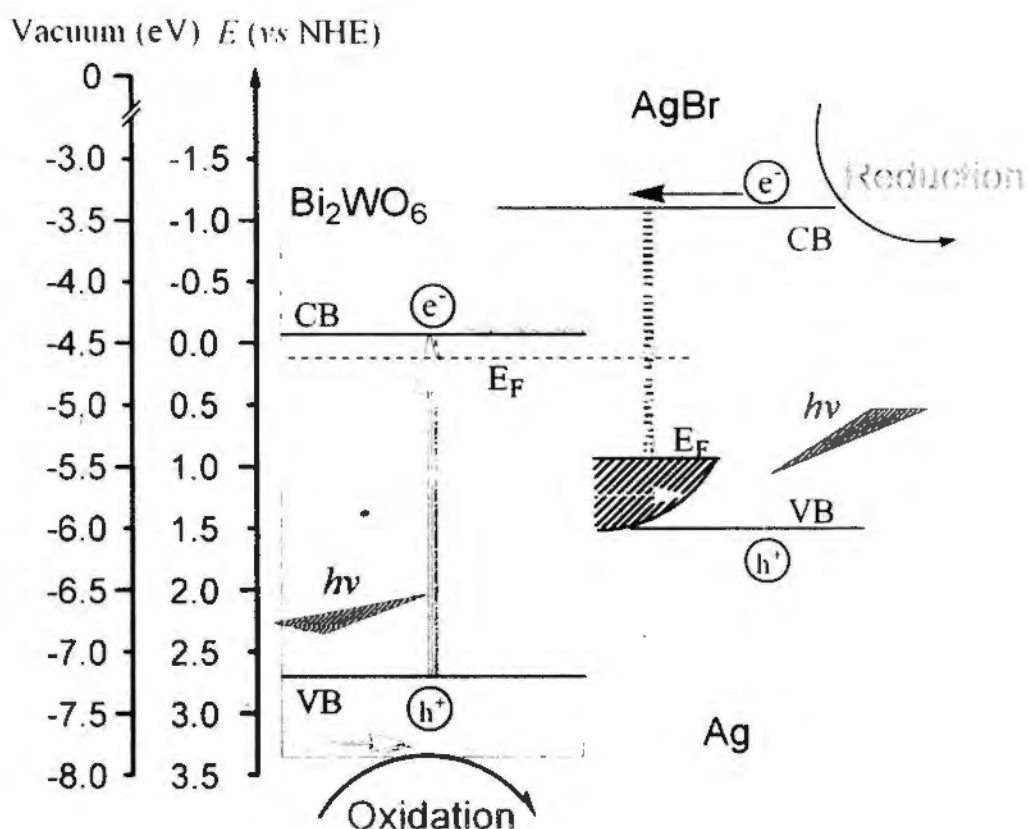
Fig.3.14 Energy band diagram and photocatalytic scheme of the AgBr-Ag-Bi$_2$WO$_6$ nanojunction.

3.5 Conclusions

An all-solid-state $AgBr$-Ag-Bi_2WO_6 nanojunction has been realized by using the facile deposition-precipitation method with Bi_2WO_6 sample as substrate, where both $AgBr$ and Bi_2WO_6 are used as the VLD photochemical systems while Ag is used as electron-transfer system. The UV-VIS spectra indicate that the range of visible light photo-response of $AgBr$-Ag-Bi_2WO_6 nanojunction is broadened. The decolorization of MX-5B by $AgBr$-Ag-Bi_2WO_6 increases with the decrease of initial pH value and initial dye concentration. Importantly, this $AgBr$-Ag-Bi_2WO_6 nanojunction shows much higher VLD photocatalytic activity than photocatalyst with single visible-light response component, such as Bi_2WO_6 nanostructures, Ag-Bi_2WO_6 and $AgBr$-Ag-TiO_2, for the degradation of an azo dye (MX-5B) and PCP. In particular, its photocatalytic activity is even higher than the sum of photocatalytic activity of two photocatalyst ($AgBr$-Ag-TiO_2 and Bi_2WO_6) containing same weight of visible-light component ($AgBr$ or Bi_2WO_6). The Energy band diagram scheme further suggests that in $AgBr$-Ag-Bi_2WO_6 nanojunction, the vectorial electron transfer driven by the two-step excitation of both VLD components ($AgBr$ and Bi_2WO_6) may be mainly responsible for its excellent VLD photocatalytic performance. Therefore, this work provides some insight into the design of new structures of multicomponent photocatalysts for enhancing VLD photocatalytic activity.

4. Zn:In(OH)$_y$S$_z$ solid solution nanoplates: Synthesis, characterizations and photocatalytic mechanism

4.1 Introduction

Recently, indium oxide (In(OH)$_3$), a wide band gap semiconductor (E_g=5.17 eV), has been proved to exhibit superior photocatalytic activity in the degradation of benzene when compared with TiO$_2$ under 254 nm UV irradiation (Li et al., 2007). Since its wide band gap is related to the deep potential of O 2p orbitals, Li et al. (2007) have succeeded in narrowing the band gap of In(OH)$_3$ by partial substitution of S^{2-} for OH$^-$ due to a higher energy level of S 3p compared with that of O 2p. To achieve a more suitable band structure for visible-light-driven (VLD) photocatalysis, Lei et al. (2006) and Li et al. (2008) have prepared zinc indium hydroxyl sulfide solid solution (Zn:In(OH)$_y$S$_z$-SS) and copper indium hydroxyl sulfide solid solution (Cu:In(OH)$_y$S$_z$-SS) by respectively doping Zn^{2+} or Cu^{2+} cation in In(OH)$_y$S$_z$ solid solution (In(OH)$_y$S$_z$-SS) in an aqueous solution of ethylenediamine. It is well known that the photocatalytic activity is closely related to the size, morphology and structure of photocatalysts (Kamat, 1993; Zhang et al., 2006; Zhang et al., 2007). Semiconductors with two-dimensional nanostructure (e.g. nanoplates) have attracted increasing attention in the photocatalytic field because of their high crystallinity and extremely high anisotropy with ultrathin thickness (Zhang and Zhu, 2005). Thus, the preparation of the Zn: In(OH)$_y$S$_z$ solid solution nanoplate (Zn: In(OH)$_y$S$_z$-SSN) with smaller particle size is an effective way to improve the photocatalytic performance of these solid solutions.

Moreover, for the TiO_2 photocatalysis, it is well established that reactive oxygen species (ROSs), such as hydroxyl radicals ($\cdot OH$), superoxide radicals ($\cdot O_2^-$), hydrogen peroxide (H_2O_2), can be generated (Hoffmann et al., 1995). Due to their strong oxidative ability, these ROSs are proved to be able to degrade a variety of organic pollutants (Ireland et al., 1995; Machado et al., 2000; Yang et al., 2009). Recently, Li et al. (2009) have found that besides the $\cdot OH$, the photogenerated holes (h^+) also play a major role for the degradation of Acid Orange 7 with magnetic AgBr as a photocatalyst. However, there is a lack of systematic study of the physiochemical mechanism about the $Zn:In(OH)_yS_z$-SS mediated PCO process, and the main responsible species for the degradation of organics still remain unknown. Furthermore, because the photogenerated electrons and holes, from which ROSs are produced, locate on the surface of the photocatalyst, some studies suggest that the adsorption capacity of the photocatalyst is very important for the photocatalytic degradation of organic pollutants (Fu et al., 2005; Zhang et al., 2009). The most interesting questions are also still not directly proved: (1) can these oxidative species diffuse to the aqueous solution to degrade the organic pollutants in the bulk, and (2) is the direct contact between the catalyst and pollutant a prerequisite for the efficient degradation of organic pollutant during the photocatalytic process?

In the present work, I report the synthesis of $Zn:In(OH)_yS_z$-SSNs using a hydrothermal reaction assisted by sodium dodecyl sulfate (SDS) instead of ethylenediamine. The effects of SDS, Zinc nitrate ($Zn(NO_3)_2$) or thiourea concentrations on the phases, photoabsorptions, and morphologies of the solid

solutions, and on their photocatalytic activities were investigated. In particular, we have developed a simple and versatile strategy to investigate the effect of a direct contact between the Zn:In(OH)$_y$S$_z$-SSNs and pollutants.

4.2 Materials and methods

4.2.1 Synthesis of photocatalysts

2 M NaOH solution was first prepared by dissolving 8 g NaOH (Riedel-de Haën®, Seelze, Germany) in 100 mL milli-Q® water. The photocatalysts were prepared by hydrothermal method as introduced in the Section 3.2.1. In(OH)$_3$ was prepared using indium nitrate hydrate (In(NO$_3$)$_3$·xH$_2$O) (99.9%, Sigma-Aldrich, St. Louis, USA) as the only precursor. In a typical synthesis, 1.5 mmol In(NO$_3$)$_3$·xH$_2$O was first dissolved in the milli-Q® water. When the pH value was adjusted to 11 using a 2 M NaOH solution, the precipitate with woolly appearance generated. After sonicating for 10 min and magnetically stirred for 30 min, the resulting suspension was transferred in a 50-mL Teflon-lined steel autoclave (Plates 3.1 and 3.2). Subsequently, the suspension was autoclaved and maintained at 160 °C for 24 h (Plate 3.3). The precipitates were collected by centrifugation and washed three times with milli-Q® water, and then washed three times with ethanol (≥99.9%, Merck KGaA, Darmstadt, Germany). After drying at 80°C, the product was obtained.

For the synthesis of In(OH)$_y$S$_z$-SS, suitable amounts of SDS (99.0%, Sigma-Aldrich, St. Louis, USA) was first dissolved in the milli-Q® water. The chemical structure of SDS is shown in Fig. 4.1. Then the desired amounts of

$In(NO_3)_3 \cdot xH_2O$ and thiourea (99.0%, Sigma-Aldrich, St. Louis, USA) was added into the SDS solution. While, for the preparation of $Zn:In(OH)_yS_z$-SS, desired amounts of zinc nitrate hexahydrate (98.0%, Sigma-Aldrich, St. Louis, USA) (The atomic ratio of Zn^{2+} to In^{3+} in the synthesis solution, hereafter simplified as X) was also added in the SDS solution before the addition of $In(NO_3)_3 \cdot xH_2O$ and thiourea. The pH value of all resulting suspensions also was adjusted to 11 using a 2 M NaOH solution. After sonicating and magnetically stirring, the resulting suspensions were hydrothermally treated at 160 °C for 24 h, and the products were obtained after washing and drying. The appearance of as prepared $Zn:In(OH)_yS_z$-SSNs was shown in Plate 4.1 (Synthesis conditions: 45 mM thiourea, 26 mM SDS, X=0.3). For comparison, the reference sample of $Zn:In(OH)_yS_z$-SS (R-$Zn:In(OH)_yS_z$-SS) was prepared by replacing the SDS aqueous solution with ethylenediamine solution according to the previous study (Lei et al., 2006).
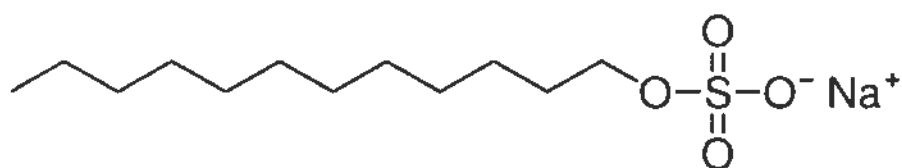
Fig. 4.1 The chemical structure of SDS.

Plate 4.1 The as prepared Zn:In(OH)$_y$S$_z$-SSNs (Synthesis conditions: 45 mM thiourea, 26 mM SDS, X=0.3).

4.2.2 Characterizations of photocatalysts

Similarly with those as mentioned in Section 3.2.2, transmission electron microscope (TEM) analyses of Zn:In(OH)$_y$S$_z$-SSs were performed with a FEI TECNAI F20 field emission electron microscope, X-ray photoelectron spectroscopy (XPS) data were recorded by a Quantum 2000 scanning ESCA microprobe instrument (Φ Physical Electronics), and UV-visible absorption spectra of the samples were recorded on a UV-VIS spectrophotometer (Varian®, Palo Alto, USA). X-ray diffraction (XRD) patterns were also recorded on a Huber diffractometer (V612365) equipped with a rotating anode and using Cu Kα radiation (Rigaku, Ru-300). While the data for XRD were recorded at a scan rate of 0.02 deg (2θ) s^{-1} in the 2θ range of 10° to 80° and at a scan rate of 0.005 deg (2θ) s^{-1} in the 2θ range of 21° to 24°.

Nitrogen adsorption-desorption isotherms were collected at 77°K using Micromeritics ASAP-2010 equipment (Micromeritics Instrument Corporation, USA)

(Plate 4.2). The Brunauer-Emmett-Teller (BET) analysis was used for the determination of specific surface area. All the samples were degassed at 180°C and 10^{-6} Torr for 24 h prior to the measurement.
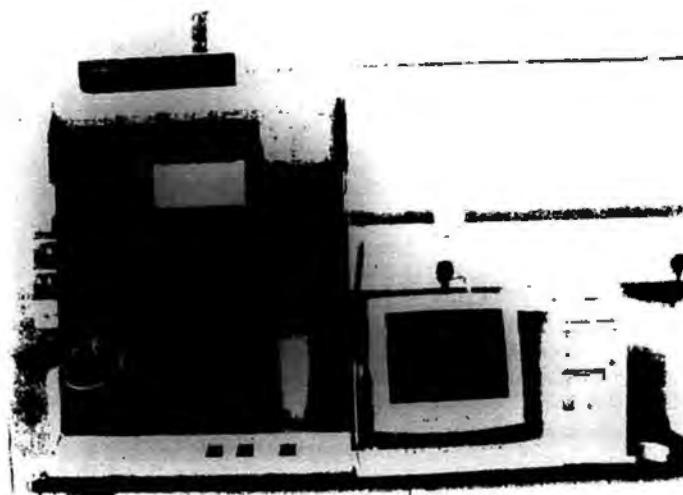
Plate 4.2 Micromeritics ASAP-2010 equipment (Micromeritics Instrument Corporation, USA)

4.2.3 Preparation of Rhodamine B (RhB) aqueous solution

50 mg L^{-1} RhB solution was prepared by dissolving 0.014 g of RhB powder (90%, Sigma-Aldrich, St. Louis, USA) into 250 mL milli-Q® water as shown in Plate 4.3.

Plate 4.3 The stock of 50 mg L^{-1} RhB.

4.2.4 The photocatalytic performances of different photocatalysts

The light source and photoreactor were the same with those used in the section 3.2.4. The visible light was vertically focused on the reaction mixture and the visible light intensity was fixed at 230 mW cm^{-2}. In each experiment, suitable amount of photocatalyst was added into RhB aqueous solution. The resulting reaction mixture were also magnetically stirred in the dark for 60 min to ensure that an adsorption/desorption equilibrium was established between the photocatalyst and RhB. Then the reaction mixture was irradiated by the visible light. At given time intervals, 1.5 mL suspension was sampled and centrifuged to remove the photocatalyst particles. The residual RhB in the solution was analyzed by recording variations at the wavelength of maximal absorption (553 nm) in the UV-VIS spectra of RhB with the Helis Gamma UV-VIS spectrophotometer. A series of RhB standards was prepared from 0.25 to 10 mg L^{-1} to construct a standard curve for qualification. The photocatalytic performance was evaluated by the decrease of the concentration and removal efficiency (%) of RhB.

4.2.5 The effect of scavengers

In order to examine the exact reactive species that play important role(s) in the photocatalytic degradation of RhB, the scavenger experiments were carried out by adding one kind of scavenger to 100 mL reaction mixture before the irradiation. The used scavengers were 0.5 mM Cr(VI) initially purged with nitrogen gas for the quenching of electron, 10 mM isopropanol (Riedel-de Haën®, Seelze, Germany) for

the removal of bulky •OH, 10 mM sodium oxalate (Peking Chemical Industrial Factory, Beijing, China) for the scavenging of hole, and 10 mM potassium iodide (KI) (Merck KGaA, Darmstadt, Germany) for the quenching of hole and surficial •OH. The stock solutions of Cr(VI) were prepared from potassium dichromate ($K_2Cr_2O_6$) (Merck KGaA, Darmstadt, Germany).

4.2.6 The adsorption effect

Since the adsorption amount of RhB on the photocatalysts is dependent on the pH value of the reaction mixture, one can investigate the effect of adsorption on the photocatalytic degradation efficiencies of RhB by adjusting the initial pH value of the reaction mixture. Herein, the initial pH value was adjusted by adding drops of 1 M HCl or 1 M NaOH solution, and was monitored using the pH meter (Thermo Orion, USA). And the pH values tested here were 3.7 ± 0.2, 4.5 ± 0.2, 6.4 ± 0.2, 8.5 ± 0.2, 9.7 ± 0.2.

4.2.7 The partition setup

50 mL 0.4 M H_2O_2 aqueous solution was prepared by directly diluting 2.1 mL H_2O_2 aqueous solution (30%, Beijin Huagong, Beijin, China) into 47.9 mL milli-Q® water. 50 mL of Fenton regent was prepared by first dissolving 0.105 g Iron (II) sulfate (90%, AJAX Chemicals, Sydney, Australia) with 0.372g ethylenediaminetetraacetic disodium salt (Na_2EDTA) (Laboratory regent, AJAX Chemicals, Sydney, Australia) into milli-Q® water and then adding suitable H_2O_2

aqueous solution (Zhang et al., 2006). 100 mg L^{-1} TiO_2 suspension was prepared by suspending 5 mg TiO_2 (P25) powder (Degussa Corporation, Frankfurt, Germany) in 50 mL milli-$Q^®$ water.

To investigate the effect of a direct contact between Zn:In(OH)$_y$S$_z$-SSNs and RhB, a semi-permeable membrane with the molecular weight cutoff (MWCO) of 12,000-14,000 daltons (Spectrum$^®$, Spectrum Laboratories, Inc., California, USA) (Plate 4.4) was used to separate the RhB and Zn:In(OH)$_y$S$_z$-SSNs. The setup of the partition system is shown as Fig. 4.2. The initial concentration of RhB in container was 2.6 mg L^{-1}. The outer system was 50 mL of the aqueous suspension containing 10 mg Zn:In(OH)$_y$S$_z$-SSNs. The suspension in the outer system was stirred continuously to keep the Zn:In(OH)$_y$S$_z$-SSNs evenly distributed in the outer solution. The whole partition setup was placed under the Xenon lamp, allowing the light to obliquely irradiate onto the solution. The visible light intensity was fixed at about 190 mW cm^{-2}. After 1 h, 1.5 mL solution both outside and inside of the container was sampled to detect the concentration of RhB. The outer system was also replaced by pure milli-$Q^®$ water, H_2O_2 aqueous solution, Fenton reagent without light irradiation or TiO_2 suspension irradiated by UV light in a series of comparison experiments.

Plate 4.4 A semi-permeable membrane with the MWCO of 12,000-14,000 Daltons (Spectrum®, Spectrum Laboratories, Inc., California, USA).
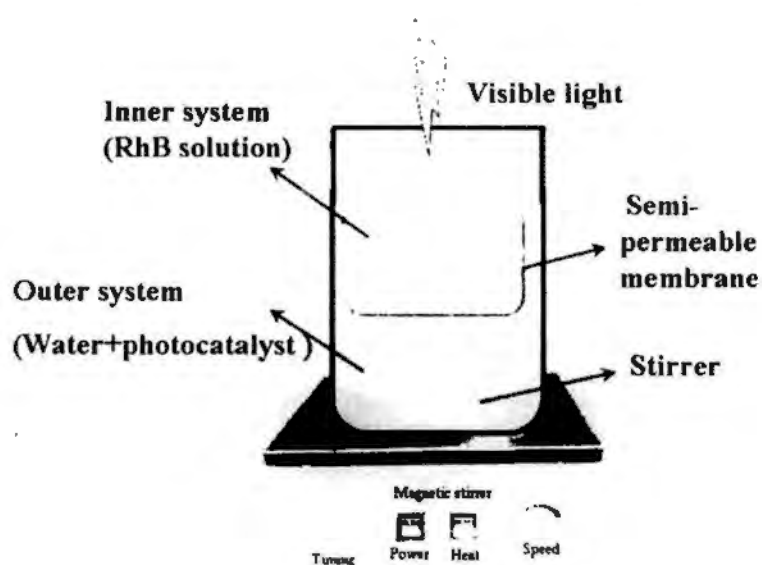
Fig. 4.2 The schematic illustration of setup for the partition system.

4.2.8 The identification of intermediates and mineralization products

To harvest higher concentration of intermediates and mineralization products, the photocatalytic reaction was carried out with 10 mg L^{-1} RhB and 200 mg L^{-1} Zn:In(OH)$_y$S$_z$-SSNs. The mineralization of RhB was identified by the detection of TOC, IC and CO_2, and the procedures were the same with that introduced in Section

3.2.5.7, except replacing MX-5B with RhB.

Parts of the intermediates were identified by a gas chromatography-mass spectroscopy (GC-MS) with gas chromatograph (Hewlett-Packard, 6890, Woodinville, England) equipped with a mass selective detector (Hewlett-Packard, 5973, Woodinville, England), an autoinjector (Hewlett-Packard, 7637, Woodinville, England) and a HP-5 MS column of 5% phenyl methyl silicone (30 m× 0.25 mm, 0.25 μm film thickness)) (Plate 4.5). The intermediates were identified by peak matching with the WILEY 275 library (Hewlett-Packard, Woodinville, England) and NBS75 library (Hewlett-Packard, Woodinville, England).
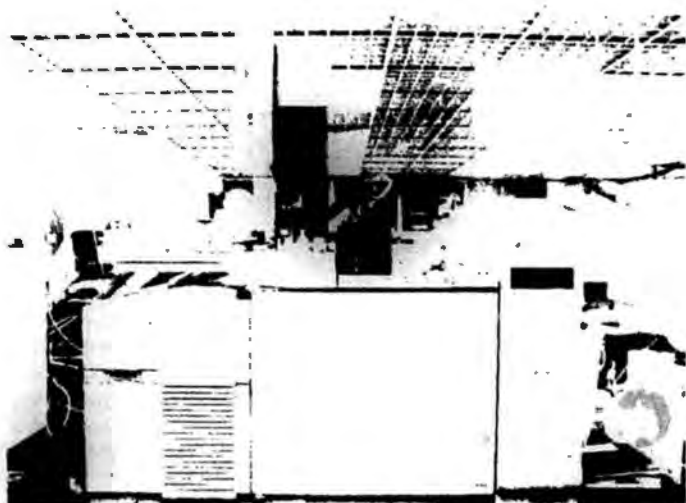
Plate 4.5 A gas chromatography-mass spectroscopy (Hewlett-Packard, Woodinville, England)

For GC-MS detection, one μL sample was injected in splitless mode for analysis. The temperature was maintained at 80°C for 5 min, and then increased to 310°C at a rate of 5°C min^{-1}. Before injection, the sample was pre-treated as follows: 40 mL of sample was taken after 20-h photocatalytic treatment. The suspension sample was

filtered to remove catalyst and the pH of the filtrate was adjusted to 2.0 with 10% HCl. Every 20 mL of the acidified filtrate was separately contained in dichloromethane (DCM) rinsed round-bottom extraction tube. Then, the acidified filtrate was mixed with 20 mL DCM (HPLC grade, Mallinckrodt, USA) and was shaken at 360 rpm for 1 h. Subsequently, the organic phase was transferred to another extraction tube and dried by a nitrogen evaporator (Associates Inc., Organomation N-Evap, Berlin, Germany) (Plate 4.6). The residue was re-dissolved in 0.5 mL DCM, and the solution was dehydrated by filtering with filter containing anhydrous sodium sulphate (Riedel-de Haën®, Seelze, Germany). Finally, trimethylsilylation was carried out at 50°C for 30 min after mix 1 mL above concentrated sample and 0.5 mL bis(trimethylsilyl)trifluoroacetamide (>99%, derivatization grade, Sigma-Aldrich, St. Louis, USA) (Hu et al., 2003).
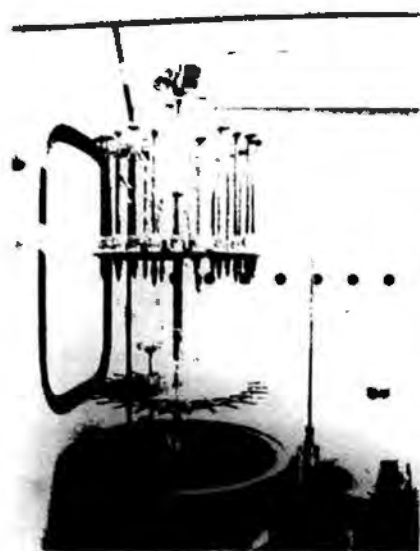
Plate 4.6 A nitrogen evaporator (Associates Inc., Organomation N-Evap, Berlin, Germany)

4.3 Results

4.3.1 Synthesis and characterizations of photocatalysts

4.3.1.1 The crystalline phase and chemical compositions

The crystalline phases of $In(OH)_3$, $In(OH)_yS_z$ and $Zn:In(OH)_yS_z$-SS samples were examined by XRD. Fig. 4.3 shows the low-resolution XRD patterns of $In(OH)_3$, $In(OH)_yS_z$ and $Zn:In(OH)_yS_z$-SS samples synthesized under various conditions with the 2-theta ranged from 20° to 80°. The characteristics of the XRD patterns for all the samples are very similar. These XRD patterns exhibit ten diffraction peaks located at about 22.2°, 31.7°, 35.6°, 39.0°, 45.5°, 51.2°, 56.6°,66.3°, 70.8° and 75.4°, which are indexed to the scattering from (200), (220), (013), (222), (400), (420), (422), (440), (442) and (620) crystal planes of the cubic $In(OH)_3$ phase, respectively. These results are in good agreement with that of the cubic $In(OH)_3$ powder obtained from the International Center of Diffraction Data Card reflections (JCPDS 85-1338). And there are no other peaks in the present XRD patterns, indicating no other phase or impurity in these samples.
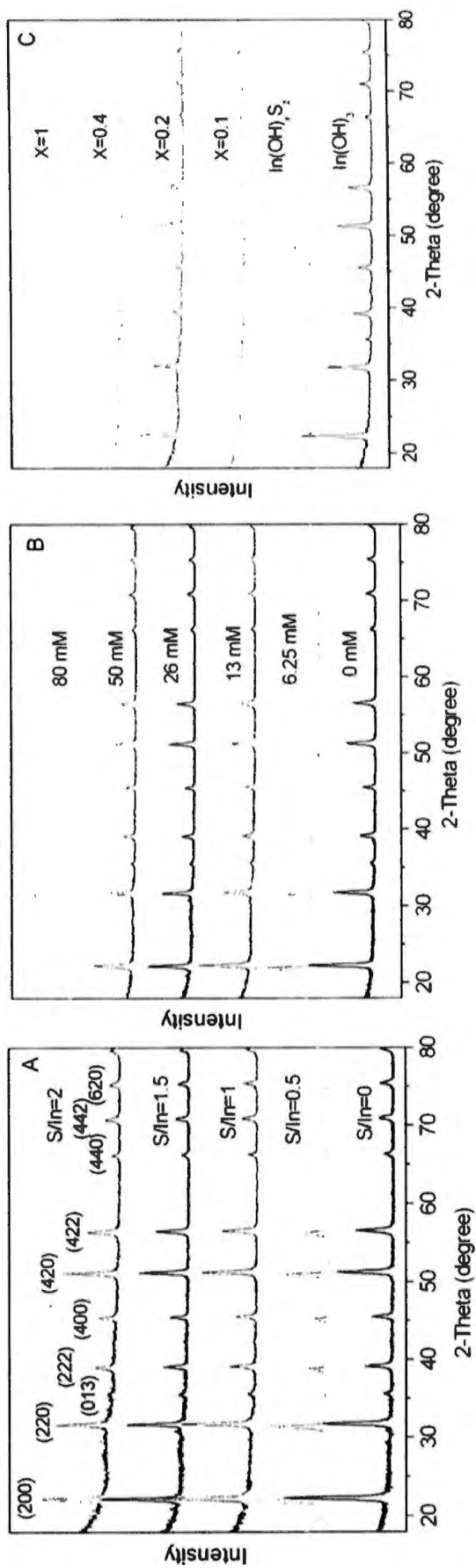
Fig. 4.3 Low-resolution XRD patterns of $In(OH)_3$, $In(OH)_yS_z$ and $Zn:In(OH)_yS_z$ solid solution samples synthesized under various conditions: (A) $In(OH)_3$ and $In(OH)_yS_z$ synthesized with the concentration of thiourea varied from 15 to 60 mM (Other synthesis conditions: 26 mM SDS, X=0), (B) $In(OH)_3$ and $In(OH)_yS_z$ synthesized with SDS concentrations varied from 6.25 mM to 80 mM (Other synthesis conditions: 45 mM thiourea, X=0), and (C) $In(OH)_3$, $In(OH)_yS_z$ and $Zn:In(OH)_yS_z$ synthesized with X value varied from 0.1 to 1 (Other synthesis conditions: 45 mM thiourea, 26 mM SDS). All these samples were synthesized in aqueous solution at 160 °C for 24 h.

To facilitate the analysis, enlargements of the XRD patterns from 21 to 24° for these samples are displayed in Fig. 4.4. The samples prepared in the absence of thiourea or SDS exhibit diffraction peaks indexed to pure cubic $In(OH)_3$ with calculated lattice constant $a=7.959$ Å (JCPDS 85-1338; $a=7.979$ Å). With an increase of thiourea concentration from 0 to 60 mM or an increase of SDS concentration from 0 to 80 mM in the synthesis solution, the diffraction peak at about 22.2° slightly shifts to low angles (Figs. 4.4 A and B), indicating the formation of $In(OH)_yS_z$-SS. When thiourea concentration was higher than 60 mM or SDS concentration was up to 130 mM, the diffraction peaks do not shift further, while diffraction peaks corresponding to β-Indium sulfide (In_2S_3) begin to appear. The samples also gradually change from white to deep yellow with the increase of thiourea or SDS concentration. Moreover, SDS concentration influences the crystalline phase of the samples. A higher concentration of SDS results in a lower diffraction intensity (Figs. 4.3B and 4.4B), which means the worse crystallization of the sample. If we added the Zn^{2+} cations into the synthesis solution (X is used to present the atomic ratio of Zn to In), the diffraction peaks at about 22.2° shift to a slightly larger angle with the increasing of X value from 0 to 1 (Fig. 4.4C), indicating the formation of $Zn:In(OH)_yS_z$ solution.
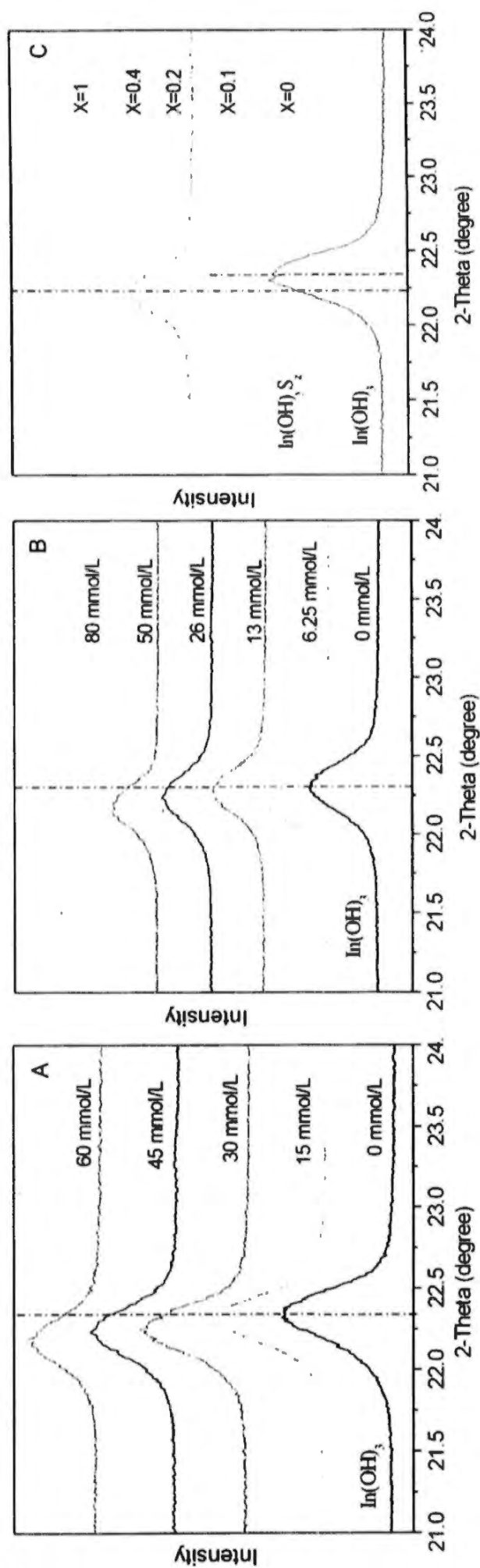
Fig. 4.4 Enlarged XRD patterns of $In(OH)_3$, $In(OH)_yS_z$ and $Zn:In(OH)_yS_z$ solid solution samples synthesized under various conditions: (A) $In(OH)_3$ and $In(OH)_yS_z$ synthesized with the concentration of thiourea varied from 15 to 60 mM (Other synthesis conditions: 26 mM SDS, X=0), (B) $In(OH)_3$ and $In(OH)_yS_z$ synthesized with SDS concentrations varied from 6.25 mM to 80 mM (Other synthesis conditions: 45 mM thiourea, X=0), and (C) $In(OH)_3$, $In(OH)_yS_z$ and $Zn:In(OH)_yS_z$ synthesized with X value from 0.1 to 1 (Other synthesis conditions: 45 mM thiourea, 26 mM SDS). Samples were synthesized in aqueous solution at 160 °C for 24 h.
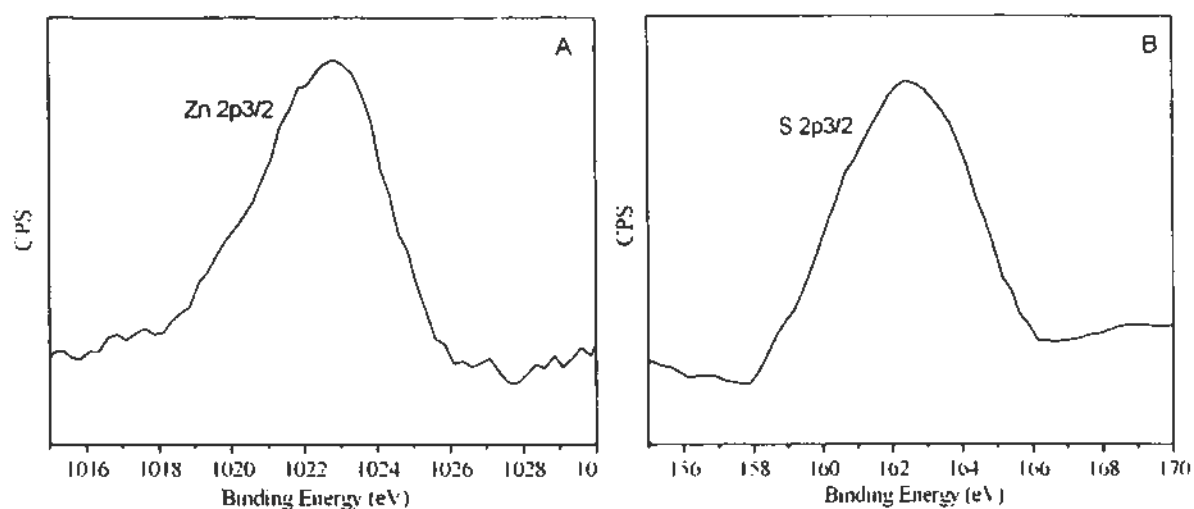
Fig. 4.5 Zn 2p3/2 (A) and S 2p3/2 (B) XPS spectra of Zn:In(OH)$_y$S$_z$-SS (Synthesis conditions: 60 mM thiourea, 26 mM SDS, X = 0.3).

XPS measurement was further carried out to investigate the composition of the Zn:In(OH)$_y$S$_z$-SS (Synthesis conditions: 60 mM thiourea, 26 mM SDS, X=0.3) and the chemical state of its constituent elements. The XPS survey spectrum reveals that the ratio of Zn, In, and S elementals on the surface of Zn:In(OH)$_y$S$_z$-SS are in the ratio of 2:10:3. Furthermore, detailed analysis was carried out by investigating high-resolution XPS spectra of the Zn 2p3/2 and S 2p3/2 region, as shown in Fig. 4.5. The peak at 1022.8 eV is attributed to Zn 2p3/2, which confirms the existence of element Zn (Pradhan et al., 2008) (Fig. 4A). On the other hand, the S 2p3/2 peak was identified at 162.2 eV, suggesting that the S element mainly exist as S^{2-} in the solid solution (Fig. 4B). No peaks is observed above 164 eV, which suggests that no other chemical states of S exist in Zn:In(OH)$_y$S$_z$-SS (Wagner and Muilenberg, 1979).

4.3.1.2 The photoadsorption properties

Fig. 4.6 shows the UV–VIS diffuse reflectance spectra (DRS) of $In(OH)_3$, $In(OH)_yS_z$-SS, ZnS and $Zn:In(OH)_yS_z$-SS samples synthesized under various conditions. As shown in Figs. 4.6A and B, the pure $In(OH)_3$ sample, obtained in the absence of thiourea or SDS, has an adsorption edge at 240 nm and a band gap of 5.17 eV, which is consistent with that reported by Avivi et al. (2000). With an increasing thiourea or SDS concentration, not only does the adsorption for $In(OH)_yS_z$ increases in intensity, but also its absorption edge red-shifts (Figs. 4.6A and B). The band gap, estimated from the onset of the absorption edge for $In(OH)_yS_z$, decreases from 5.17 to 2.09 eV when the thiourea concentration increased from 0 to 60 mM, and from 5.17 to 2.01 eV when the SDS concentration increased from 0 to 50 mM. The absorption edges of the $Zn:In(OH)_yS_z$-SSs, which are located between those of ZnS and $In(OH)_yS_z$, shift gradually from 560 to 405 nm with an increase of X from 0 to 1 (Fig. 4.6C), corresponding to an increase in the band gap from 2.21 to 3.06 eV. No absorption ascribed to ZnS is observed, confirming that the Zn^{2+} was homogeneously doped into the lattice of $In(OH)_yS_z$. Moreover, $Zn:In(OH)_yS_z$ with low Zn doping exhibits steep edges and strong absorption in the visible light region, suggesting that the absorption is due to the direct transitions between the VB and the CB of the $Zn:In(OH)_yS_z$-SS.
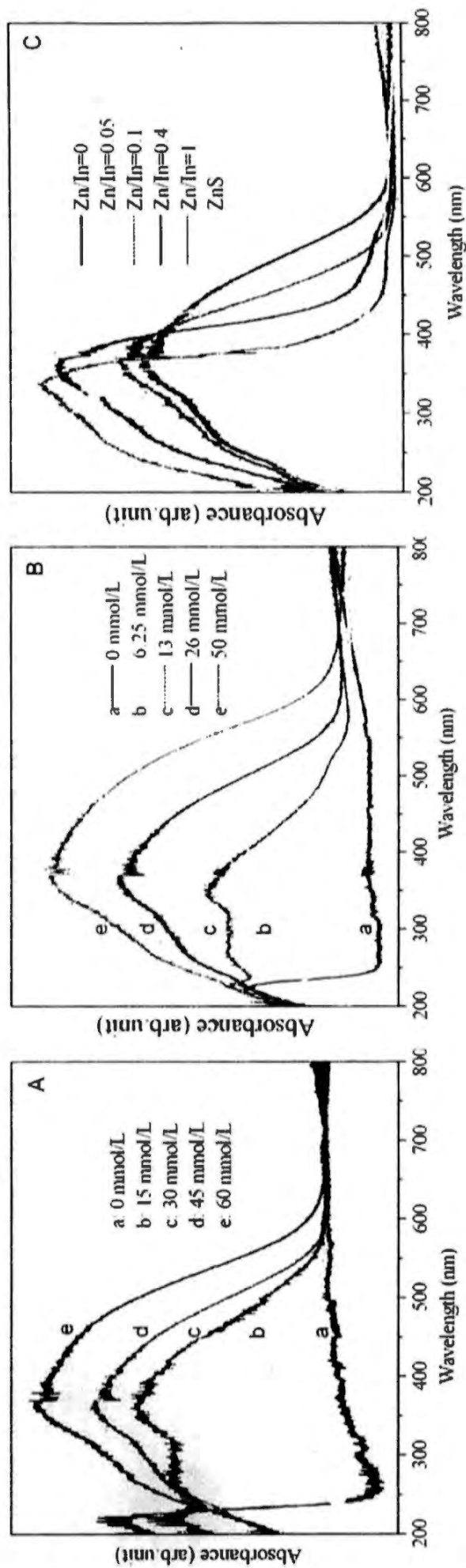
Fig. 4.6 UV–VIS DRS of In $(OH)_3$, $In(OH)_yS_z$, ZnS and Zn:$In(OH)_yS_z$ solid solution samples synthesized under various conditions: (A) In$(OH)_3$ and $In(OH)_yS_z$ synthesized with thiourea concentrations varying from 15 to 60 mM (Other synthesis conditions: 26 mM SDS, X=0), (B) In$(OH)_3$ and $In(OH)_yS_z$ synthesized with SDS concentrations varied from 6.25 to 80 mM (Other synthesis conditions: 45 mM thiourea, X=0), and (C) ZnS, In$(OH)_3$, $In(OH)_yS_z$ and Zn:$In(OH)_yS_z$ synthesized with X value varying from 0.05 to 1 (Other synthesis conditions: 45 mM thiourea, 26 mM SDS). Samples were synthesized in aqueous solution at 160 °C for 24 h.

4.3.1.3 Morphologies

SDS does not only play an important role in the substitution of S^{2-} to form Zn:In(OH)$_y$S$_z$-SSs, but it also significantly influences their morphologies. Fig. 4.7 demonstrates the TEM and HRTEM images of Zn:In(OH)$_y$S$_z$-SSs prepared with different concentrations of SDS as well as the image of R-Zn:In(OH)$_y$S$_z$-SS prepared according to the previous study (Lei et al., 2006). As shown in Fig. 4.7A, Zn:In(OH)$_y$S$_z$-SSNs exhibit a rectangular-plate shape, with an average width of about 10 nm and an average length of about 15 nm when the SDS concentration was 26 mM. The HRTEM image (inset of Fig. 4.7A) further demonstrates the clear lattice fringes with lattice spacing of 0.42 nm, which is slightly larger than the value of the (200) plane of the cubic In(OH)$_3$ (d=0.40 nm). This phenomenon mainly results from the larger ionic radius of S^{2-} (1.84 Å) compared with the thermochemical radius of OH⁻ (1.40 Å) (Li et al., 2007). With increasing concentrations of the SDS surfactant, the rectangular nanoplate tends to be transformed into smaller square nanoplates, meanwhile parts of the nanoplates display truncated corners or some breakage of the edges, resulting in irregular outlines of Zn:In(OH)$_y$S$_z$-SSs (Fig. 4.7B). Eventually, when the concentration of SDS was further increased to 80 mM, only spherical particles with an average diameter about 8 nm could be observed, instead of a plate-like morphology (Fig. 4.7C). Although the R-Zn:In(OH)$_y$S$_z$-SS have plate structure, the diameter sizes are not uniform and ranged from 20 nm to 300 nm (Fig. 4.7D).
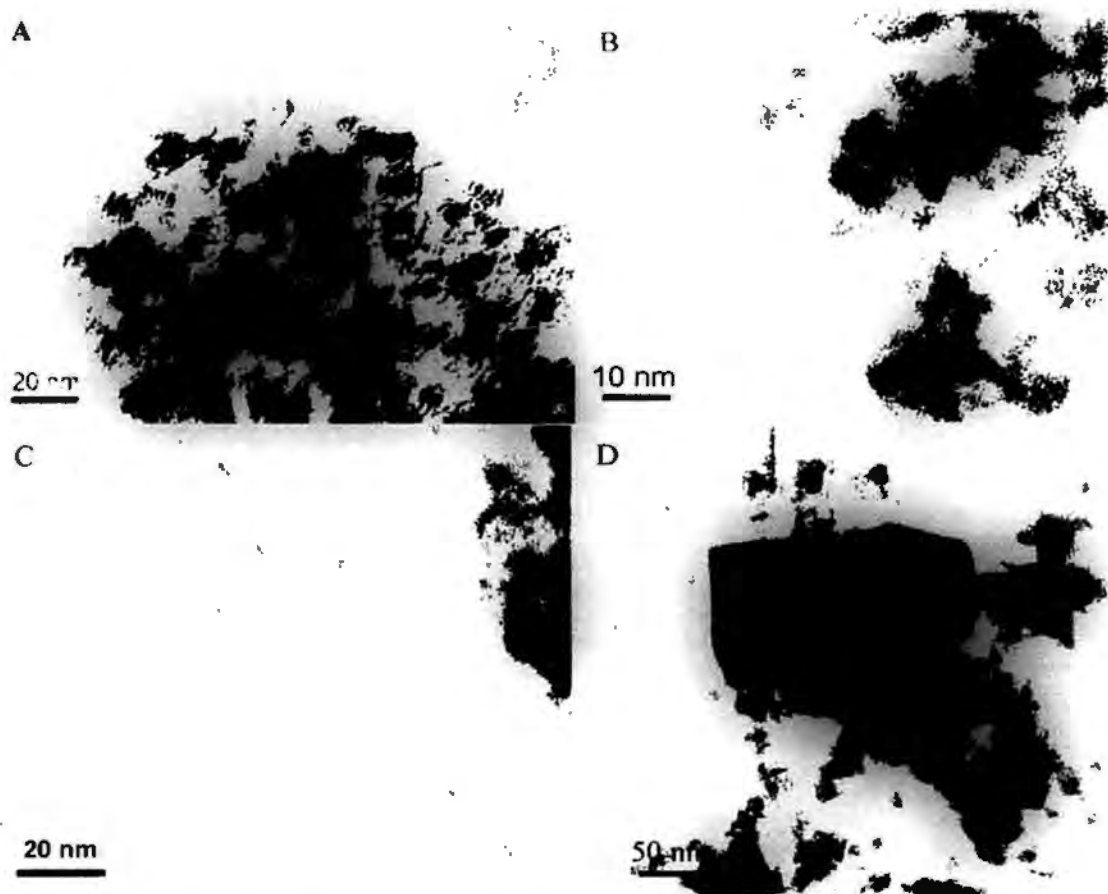
Fig. 4.7 TEM and HRTEM images of Zn:In(OH)$_y$S$_z$-SS (Other synthesis conditions: 45 mM thiourea, X = 0.3) synthesized with different SDS concentrations: (A) 26 mM, (B) 50 mM and (C) 80 mM; (D) TEM image of R-Zn:In(OH)$_y$S$_z$-SS prepared in an aqueous solution of ethylenediamine (Other synthesis conditions: 45 mM thiourea, X = 0.3) (Lei et al., 2006).

4.3.2 Photocatalytic activities

4.3.2.1 Photocatalytic performances of different photocatalysts

RhB, a widely used dye, was chosen as a representative pollutant to evaluate the photocatalytic performances of the photocatalysts. When dissolved in distilled water, RhB has a major absorption band centered at 553 nm, which was used to monitor the photocatalytic degradation of RhB. The photocatalytic performances of different photocatalysts were determined by comparing the degradation efficiencies of RhB with otherwise identical conditions under visible light irradiation (Fig. 4.8).

Under visible light irradiation, ZnS, a UV-excited photocatalyst, degraded 19% of RhB within 60 min. In contrast, $In(OH)_3$, with a wide band gap of 5.17 eV, shows no photocatalytic activity under visible light. When OH^- in $In(OH)_3$ was partly substituted by S^{2-}, the photocatalytic degradation efficiency was enhanced to 15%. However, this degradation efficiency is inadequate to meet modern environmental remediation goals. The incorporation of Zn^{2+} into the $In(OH)_yS_z$ further improved the photocatalytic degradation efficiency to 63.9% when X was 0.05.
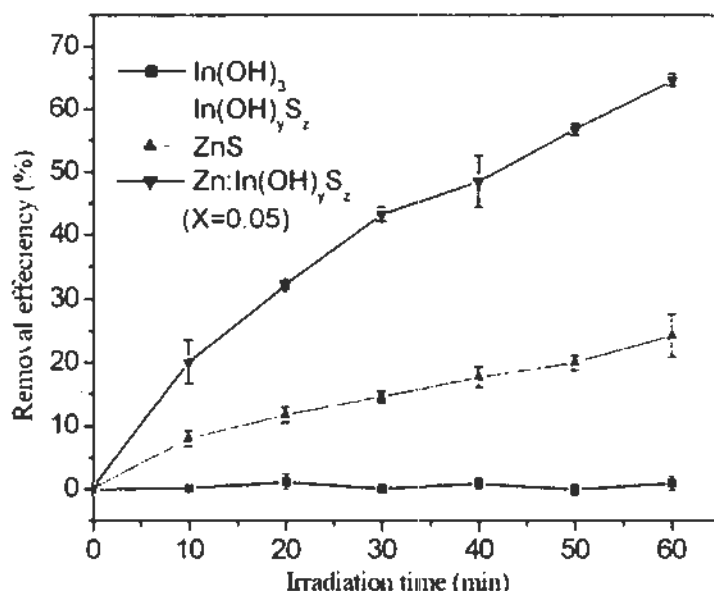
Fig. 4.8 The photocatalytic degradation efficiencies of RhB (5 mg L^{-1}, 100 mL) by different photocatalysts (100 mg L^{-1}) as a function of irradiation time under visible light. $In(OH)_3$ was prepared with 26 mM SDS and without thiourea, ZnS was prepared with 26 mM SDS, 45 mM thiourea and without In^{3+}, $In(OH)_yS_z$-SS was prepared with 26 mM SDS and 45 mM thiourea, and $Zn:In(OH)_yS_z$-SSN was prepared with 26 mM SDS, 45 mM thiourea and X value of 0.05. Each data point and error bar represents the mean and the standard deviations of independent triplicates respectively.

4.3.2.2 The effect of morphology and crystallinity

From the XRD (Section 4.3.1.1) and TEM results (Section 4.3.1.3), it is clear that SDS concentration in the synthesis solution affects the morphology and crystallinity of the $Zn:In(OH)_yS_z$-SS. The morphology and crystallinity of photocatalysts are suggested to be able to significantly influence the photocatalytic performances (Kamat, 1993; Zhang et al., 2007). Thus, in this project, I have also investigated the photocatalytic performances of $Zn:In(OH)_yS_z$-SS with different morphologies and degrees of crystallinity resulted from different concentrations of SDS.

Fig. 4.9 shows the photocatalytic degradation efficiencies of RhB under visible light irradiation by $Zn:In(OH)_yS_z$-SSs prepared with various SDS concentrations. $Zn:In(OH)_yS_z$-SSNs, which are prepared in the presence of 26 mM SDS, shows the highest photocatalytic activity and could photocatalytically degrade 93.9% RhB after 60 min. The highest photocatalytic activity of $Zn:In(OH)_yS_z$-SSN results from its smaller and uniform particle size (Fig. 4.7A), and higher degree of crystallinity (Fig. 4.3B). With the increase of the SDS concentration, the photocatalytic activity of $Zn:In(OH)_yS_z$-SS declined. When the concentration of SDS was 50 mM, the photocatalytic degradation efficiency of RhB only reached 78% after 60 min. What is more, only 27.4% RhB was photocatalytically degraded by $Zn:In(OH)_yS_z$-SS prepared with 80 mM SDS, mainly due to its sphere-like shape (Fig. 4.7C) and the lowest degree of crystallinity (Fig. 4.3B). It is also observed that after 60 min, 71.5% RhB was photocatalytically degraded by the R-$Zn:In(OH)_yS_z$-SS, which is lower than that degraded by $Zn:In(OH)_yS_z$-SSN with smaller and uniform particle size, but is higher than that degraded by $Zn:In(OH)_yS_z$-SS with spherical shape.
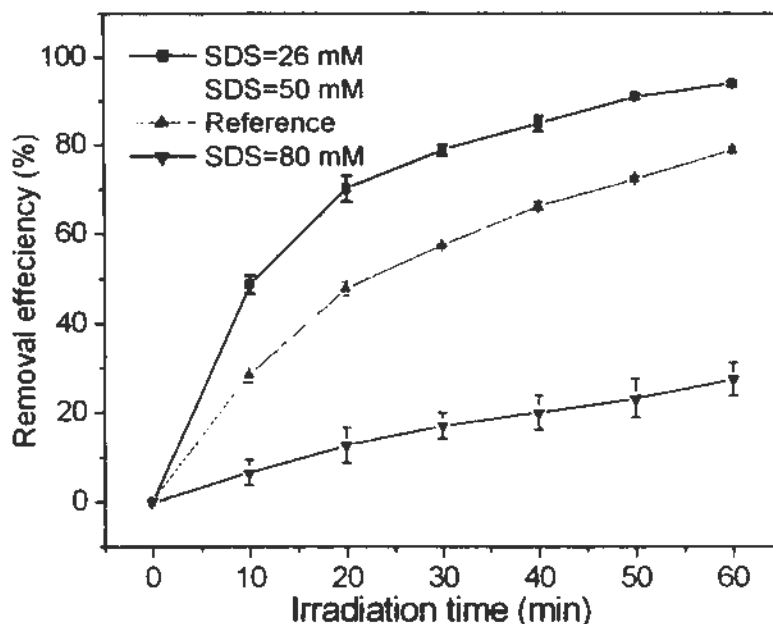
Fig. 4.9 The photocatalytic degradation efficiencies of RhB (5 mg L^{-1}, 100 mL) under visible light irradiation by 10 mg $Zn:In(OH)_yS_z$-SS prepared with 45 mM thiourea and X value of 0.5 at different SDS concentrations as well as R-$Zn:In(OH)_yS_z$-SS prepared in aqueous solution of ethylenediamine (Lei et al., 2006). Each data point and error bar represents the mean and the standard deviations of independent triplicates respectively.

4.3.3 Photocatalytic mechanism

4.3.3.1 The roles of the active species

In order to find out why the incorporation of Zn^{2+} in the solid solution can significantly improve the photocatalytic performances as mentioned in Section 4.3.2.1, the photochemical mechanism was further investigated by comparing the photocatalytic performances of $Zn:In(OH)_yS_z$-SSNs with various X values.

Fig. 4.10 shows the photocatalytic degradation efficiencies of RhB by $Zn:In(OH)_yS_z$-SSNs with various X values as a function of time under visible light

irradiation. When the X value was below 0.6, the photocatalytic performances of the Zn:In(OH)$_y$S$_z$-SSNs were gradually enhanced with the increase of the X value. When the X value was 0.6, the photocatalytic performance reached the optimal, and 95.6% RhB was quickly degraded. However, with the further increase of the X value (such as X=0.7), the photocatalytic performance declined and there was 92.7% RhB photocatalytically degraded after 60 min. When the X value was increased to 1.0, a quick and pronounced drop of the photocatalytic activity was observed and only 51.8% RhB was photocatalytically degraded after 60 min (Fig.4.10).
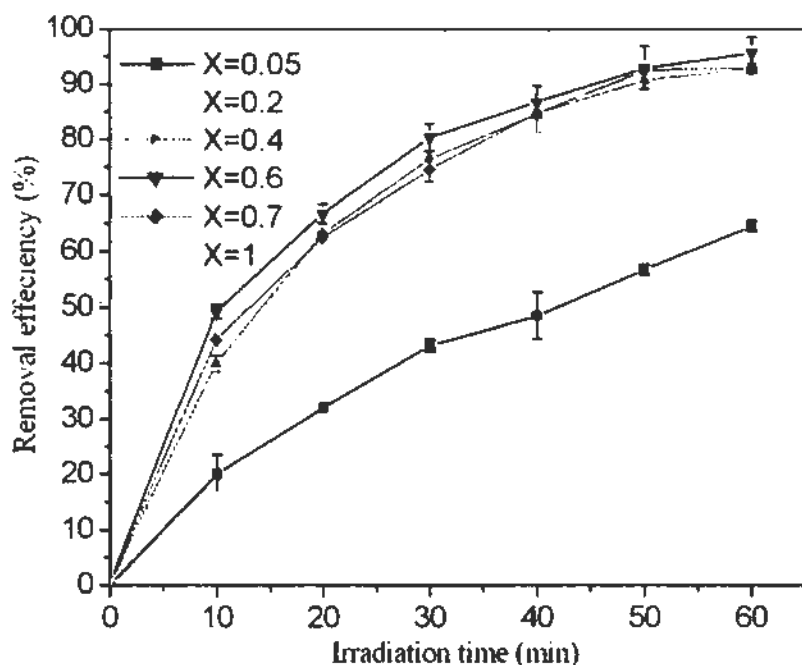
Fig. 4.10 The photocatalytic degradation efficiencies of RhB (5 mg L^{-1}, 100 mL) under visible light irradiation by 10 mg Zn:In(OH)$_y$S$_z$-SSNs prepared with different X value, 26 mM SDS and 45 mM thiourea. Each data point and error bar represents the mean and the standard deviations of independent triplicates respectively.

During the PCO process, the ROSs are generally accepted for the degradation of the organic pollutants. In order to investigate the specific reactive species that play important roles in $Zn:In(OH)_yS_z$-SSNs mediated photocatalytic process, several kinds of scavengers were added in the reaction mixture. Sodium oxalate was used to scavenge the photogenerated holes (Jin et al., 2004), KI was used to scavenge the photogenerated holes and •OH on the surface of photocatalyst generated (denoted as •OH$_s$) (Chen et al., 2005), isopropanol was added for the quenching of •OH in the bulk (denoted as •OH$_b$) (Chen et al., 2005; Khodja et al., 2005), and Cr(VI) was used for the quenching the photogenerated electrons (Chen et al., 2005).

Fig. 4.11 shows the photocatalytic degradation efficiencies of RhB by $Zn:In(OH)_yS_z$-SSNs in the presence of these scavengers under visible light irradiation. Notably, as it can be seen in Fig.4.11, the addition of isopropanol had negligible effect on the photo-degradation of RhB, indicating that there was little •OH$_b$ existing in aqueous solution. However, in the presence of sodium oxalate, the decolorization rate of RhB declined, and only 69% of RhB was degraded after 60 min irradiation. With the addition of KI, the decolorization rate of RhB dropped sharply and only 17% of RhB was degraded. Upon purging with nitrogen and the addition of Cr(VI), the photodegradation efficiency only reached 32%. These results give the evidences that the photogenerated holes and electrons as well as •OH$_s$ are involved in the photocatalytic degradation of RhB.
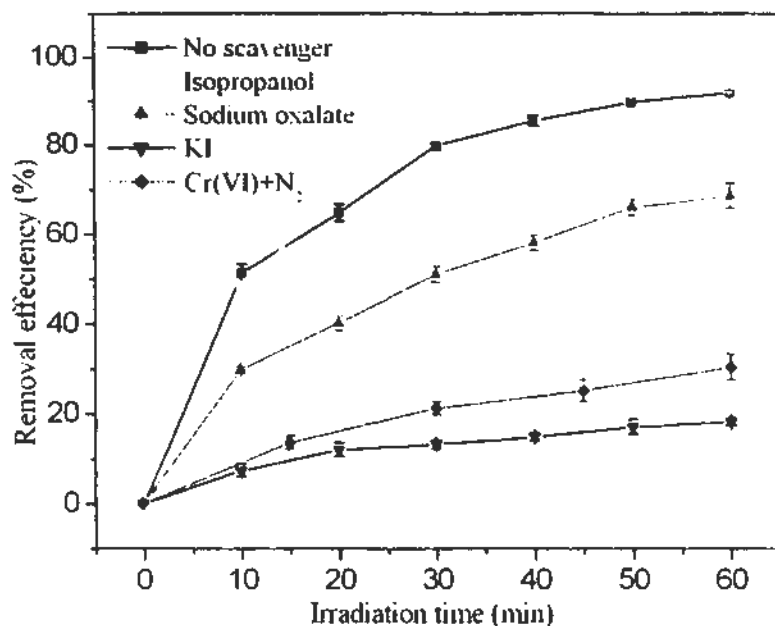
Fig. 4.11 The photocatalytic degradation efficiencies of RhB (5 mg L^{-1}, 100 mL) by 10 mg Zn:In(OH)$_y$S$_z$-SSNs (Synthesis conditions: 26 mM SDS, 45 mM thiourea, X=0.5) in the presence of the scavenger (10 mM isopropanol, sodium oxalate, KI and 0.5 mM Cr(VI)) under visible light irradiation. Each data point and error bar represents the mean and the standard deviations of independent triplicates respectively.

4.3.3.2 The adsorption effect

As discussed in Chapter 3, the adsorption efficiency of the pollutant by the catalyst can be 'tuned' by adjusting the initial pH of the suspension. In this chapter, the effect of adsorption on the photocatalytic degradation of RhB was also studied by adjusting the initial pH of reaction mixture, which is demonstrated in Fig. 4.12. It was observed that with the decrease of the pH value, the adsorption efficiency of RhB by Zn:In(OH)$_y$S$_z$-SSNs increased, which resulted in the improvement of the photocatalytic degradation of RhB.
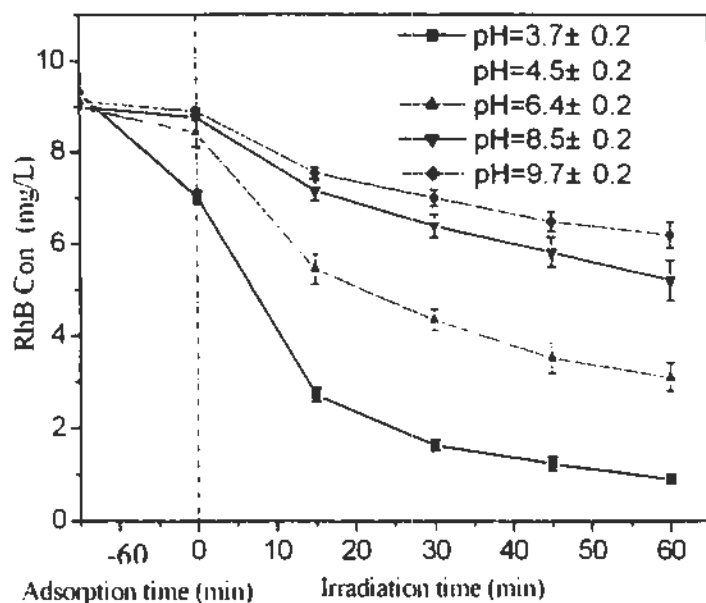
Fig. 4.12 The adsorption and photocatalytic degradation efficiencies of RhB as function of time by 100 mg L^{-1} Zn:In(OH)$_y$S$_z$-SSNs (Synthesis conditions: X value of 0.5, 26 mM SDS and 45 mM thiourea) at different initial pH value of suspension. Each data point and error bar represents the mean and the standard deviations of independent triplicates respectively.

4.3.3.3 The effect of direct contact

In this project, a novel and simple partition setup was constructed to further investigate the photocatalytic mechanisms, in which a semi-permeable membrane was used to allow the free entry of small molecules such as •OH and •O$_2^-$, but only slow leakage of RhB, as shown in Fig. 4.2.

Fig. 4.13 shows the percentages of RhB inside and outside semi-permeable membrane when the outer system was in the following control conditions: (A) Water + TiO$_2$, (B) Water + Zn:In(OH)$_y$S$_z$, (C) Water + visible light (VL), (D) Water + UV, and (E) Water. As shown from Fig. 4.13E, when the outer system was only water, 83.5% of the RhB was kept within the container and 16.3% of the RhB diffused into the outer water after 60 min. When the outer system was added with the

photocatalyst (such as TiO_2 or $Zn:In(OH)_yS_z$-SS), or the light irradiation (such as visible light or UV light), there were also $84\pm0.5\%$ of RhB kept within the container, indicating that either photocatalyst in the outer suspension or the irradiation of light could not degrade the RhB in the container or affect the diffusing of the RhB from the inside to the outside. However, the percentages of RhB in the outer system decreased when the our system contained the photocatalyst, TiO_2 or $Zn:In(OH)_yS_z$-SS due to the adsorption capacity of these photocatalyst.

Fig. 4.14 gives the percentages of RhB in or out of the container after 60 min for the different outer systems: (A) Water, (B) Water + H_2O_2, (C) Water + Fenton reagent, (D) Water + TiO_2 + UV, and (E) Water + $Zn:In(OH)_yS_z$ +VL. The percentages of RhB in and out of the container were kept about 83 ± 0.5 and $17\pm0.5\%$, respectively, when the outer system was water and H_2O_2, indicating that H_2O_2 hardly degrade RhB. Notably, when the outer system was Fenton reagent, only 5% of RhB remained in the container, and no RhB was detected outside of the container, which indicates that most of RhB both in and out of the container was degraded. When employing water, TiO_2 and UV as the outer system, RhB out of the container completely disappeared, and the percentage of RhB in the container declined to 56%. With the $Zn:In(OH)_yS_z$-SS, water and VL as the outer system, the concentration of RhB in the outer solution became about zero after 1 h of PCO process, which is similar to that in the TiO_2-mediated photocatalytic process. However, the percentage of RhB in the container showed no appreciable difference with that employing pure water as outer system, which indicates that RhB in the container was not degraded.
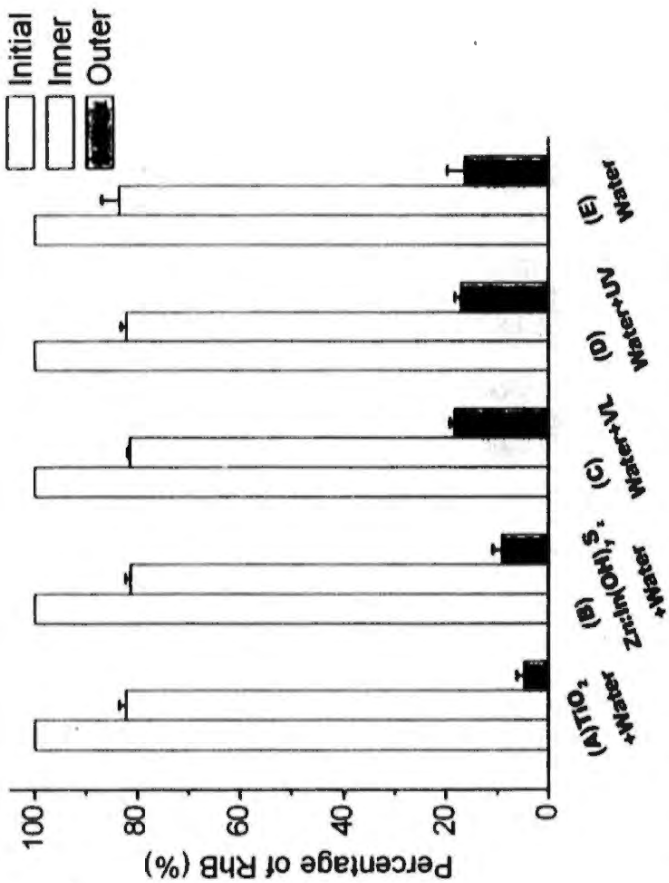
Fig. 4.13 The percentages of RhB inside and outside a semi-permeable membrane when the outer system in different control conditions. (A) Water and TiO$_2$, (B) Water + Zn:In(OH)$_y$S$_z$-SS, (C) Water + VL, (D) Water + UV, (E) Water. Each data point and error bar represents the mean and the standard deviations of independent triplicates respectively.
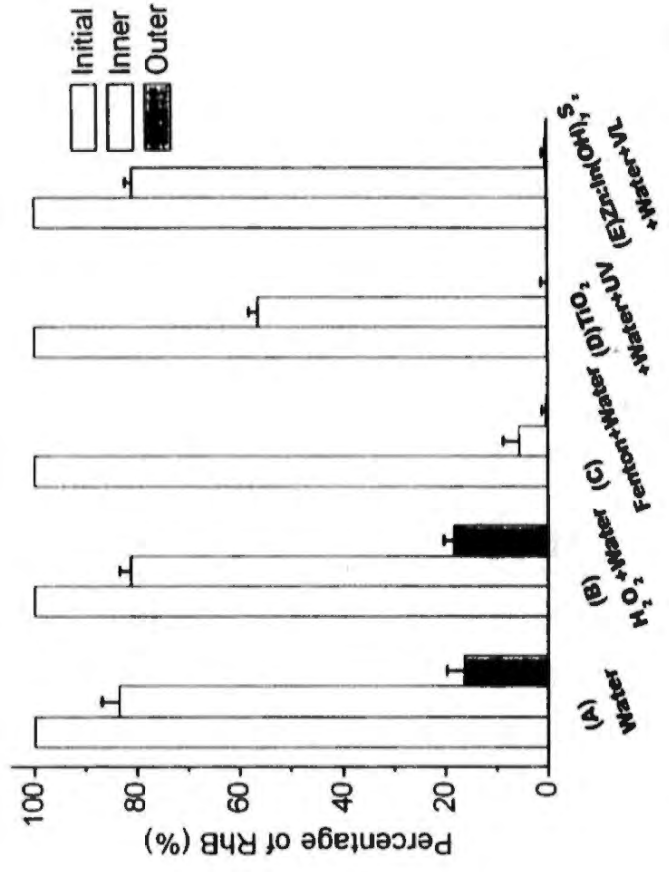
Fig. 4.14 The percentages of RhB inside and outside a semi-permeable membrane packaged container when the outer system was in various conditions. The initial concentration of RhB is 2.6 mg L^{-1}. (A) Water, (B) Water + H$_2$O$_2$, (C) Water + Fenton reagent, (D) Water + TiO$_2$ + UV, and (E) Water + Zn:In(OH)$_y$S$_z$ + VL.

4.2.3.4 The degradation mechanism of RhB

The intermediates generated during the photocatalytic process were identified by the GC-MS as shown in the Fig. 4.15. Compare to the blank, it is found that there are more several peaks appeared in GC-MS spectrum for the sample photocatalytically treated for 20 h, which are respectively indexed to the p-trimethylsilyloxybenzaldehyde oxime, 2-chlorocyclohexanol, (2-cyclohexen-1yloxy) trimethyl silane, 2,2,2-trifluoro-N,N-bis(trimethylsilyl) acetamide. Concerning the treatment process of acidification and trimethylsilylation, the intermediates generated during the PCO process should be smaller molecules such as 2-cyclohexene, benzaldehyde and cyclohexenol.

In order to further investigate the photocatalytic mineralization of RhB, Fig. 4.16 illustrates the total organic carbon (TOC) removal efficiency, and the formation of CO_2 and inorganic carbon (IC: HCO_3^- and CO_3^{2-}) during the mineralization of RhB by Zn:In(OH)$_y$S$_z$-SSNs under visible light irradiation. The TOC removal efficiency increased to 64% after 32 h, companying a steady increase in the evolved CO_2 and the concentration of IC in the solution, which reveals that RhB was steadily mineralized and the loss of TOC was transformed to gaseous CO_2 and/or inorganic carbon in solution. But the loss of TOC via mineralization was much lower than the photocatalytic decolorization of RhB, because the large organic molecules were photo-oxidized to smaller organic intermediates, and further degradation of these intermediates to CO_2 and H_2O took place slowly.
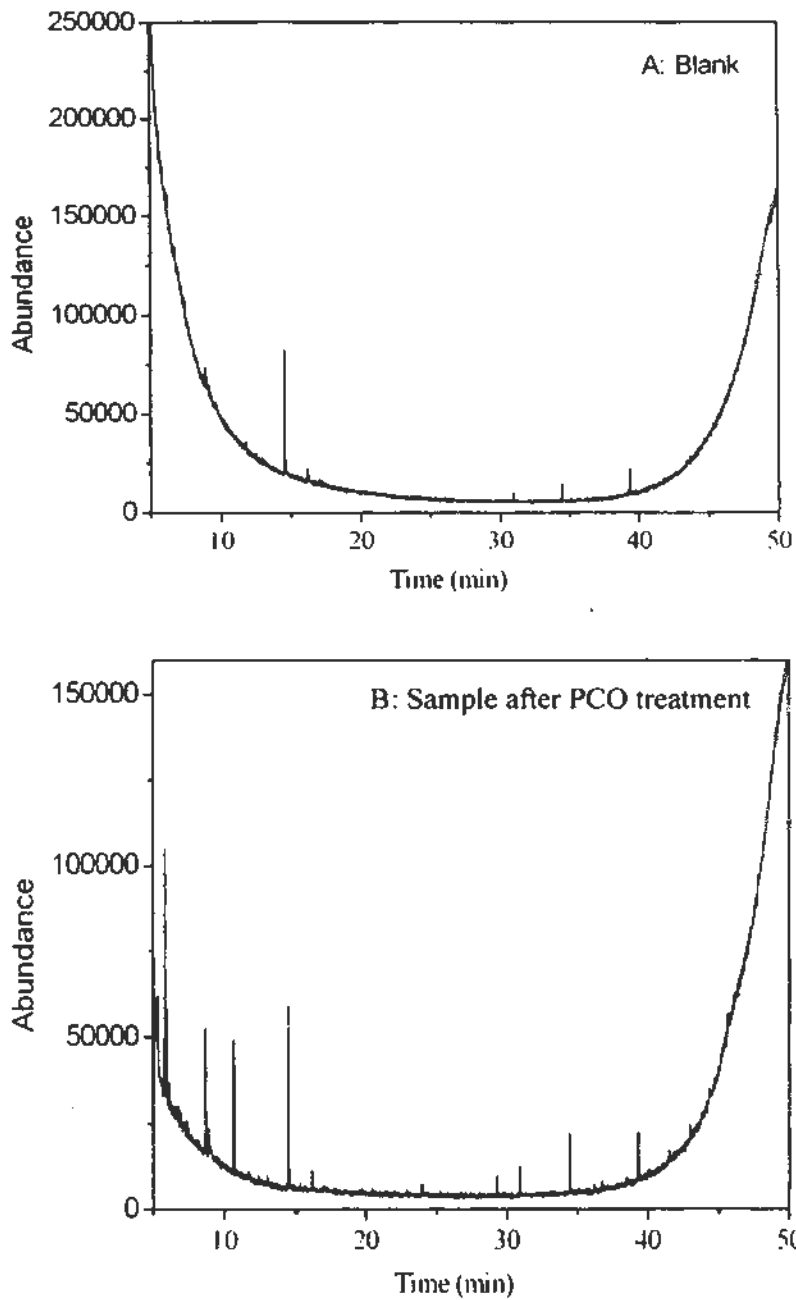
Fig.4.15 GC-MS spectrum of DCM (solvent as blank) and intermediates generated during the photocatalytic degradation of RhB: (A) blank, (B) intermediates generated after 20 h of PCO treatment.
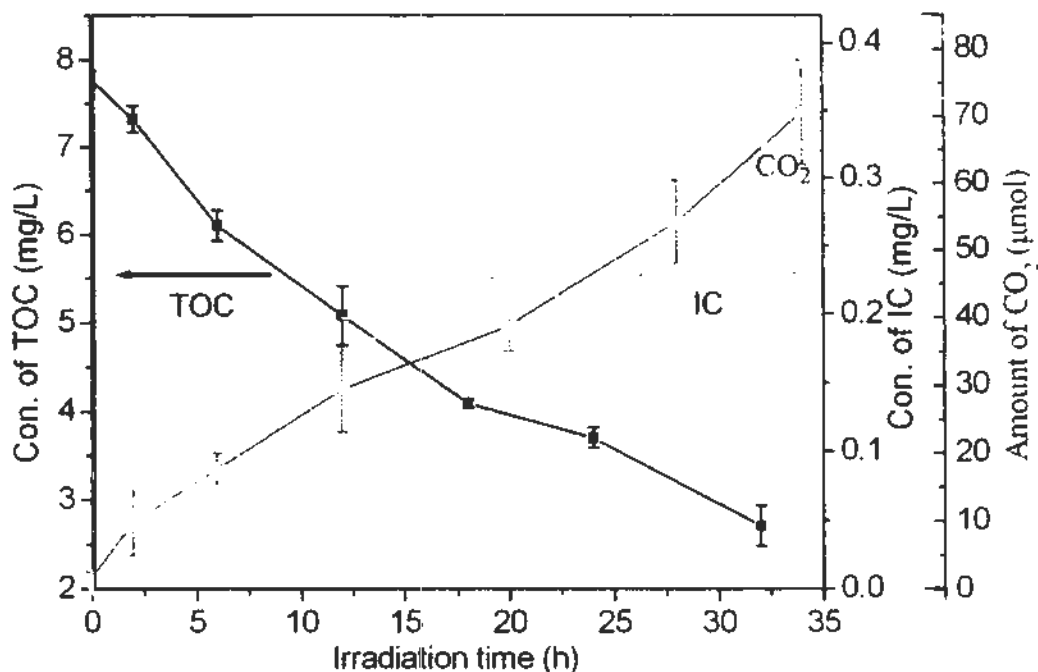
Fig. 4.16 TOC removal efficiency, formation of CO_2 and IC during the mineralization of RhB (10 mg L^{-1}, 200 mL) by 0.04 g $Zn:In(OH)_yS_z$-SSNs under visible light irradiation.

4.4 Discussion

4.4.1 Preparation and characterizations of catalyst

4.4.1.1 The crystalline phase and chemical compositions

XRD results indicates that all the solid solution samples exhibit single-phase diffraction patterns, indicative of the cubic structure similar to $In(OH)_3$ (Fig. 4.3). However, the diffraction peaks of the samples at about 22.2° slightly shifts to lower angle with the increase of the concentration of thiourea or SDS in the synthesis solution, revealing that more S^{2-} ions are homogeneously incorporated into the lattice of $In(OH)_3$ to form $In(OH)_yS_z$-SSs (Figs. 4.4 A and B). Considering the difference between the ionic radius of S^{2-} (1.84 Å) and the thermochemical radius of OH^- (1.40 Å), the low angle shift of the diffraction peaks is reasonable (Li et al., 2007).

Zn:In(OH)$_y$S$_z$-SSs were realized by adding Zn^{2+} cations into the synthesis solution. As shown in Fig. 4.4C, with the increase of X value from 0 to 1, the peak of Zn:In(OH)$_y$S$_z$ shifts to a slightly larger angle, suggesting that Zn^{2+} is homogeneously located in the lattice of In(OH)$_y$S$_z$. It is also speculated that Zn^{2+} is substituted for In^{3+} in the lattice of In(OH)$_y$S$_z$ due to the slightly larger ionic radius of In^{3+} (0.81 Å) than that of Zn^{2+} (0.74 Å) (Lei et al., 2006).

XPS results also indicates the presence of S^{2-} and Zn^{2+} in the solid solution, further confirming that Zn and S are homogeneously incorporated into the lattice of crystalline In(OH)$_3$ to form the Zn:In(OH)$_y$S$_z$-SS (Fig. 4.5).

4.4.1.2 The photoadsorption properties

Theoretical calculations indicate that VB of In(OH)$_3$ is dominated by O 2p. whose potential is much more positive than that of S 3p (Li et al., 2006). Thus, the more S^{2-} ions are substituted for OH$^-$ ions in In(OH)$_3$, the less positive the new VB and the smaller the band gap of In(OH)$_y$S$_z$-SS formed by the hybridization of O 2p and S 3p are. Therefore, the band gap of In(OH)$_y$S$_z$ can be narrowed by the S^{2-} incorporation, which is realized by the increase of the concentration of thiourea or SDS in the synthesis solution. On the contrary, since the energy level of Zn 4s4p is more negative than that of In 5s5p, the new CB in the Zn:In(OH)$_y$S$_z$-SS introduced by the hybridization of the In 5s5p with Zn 4s4p can shift to a more negative energy level, which results in the increase of the band gap of Zn: In(OH)$_y$S$_z$-SS (Fig. 4.6C). Therefore, the analysis of UV-VIS DRS of the samples gives us the opportunity to

design the suitable band gap as well as potentials of CB and VB of the solid solution to achieve the effective VLD photocatalysts.

4.4.1.3 Morphologies

As a kind of anionic surfactant, SDS has been widely used in control of the nanocrystal morphology and particles size of materials during the synthesis process (Usui, 2007; Kuo and Huang, 2008; Wang et al., 2008). Without any SDS in the synthesis solution, the cubic crystalline structure of the $Zn:In(OH)_yS_z$-SSs plays an important role in the high intrinsic anisotropic growth. Thus the $R-Zn:In(OH)_yS_z$-SSs possess large and nonuniform particle sizes, and plate morphology (Fig. 4.7D). Oxygen in the hydrophilic group of dodecyl sulfate ions is negatively charged as shown in Fig. 4.1. An electrostatic interaction between the hydrophilic group and a positive charged species such as Zn^{2+}, In^{3+} or the positive charged crystalline can confine the growth of the $Zn:In(OH)_yS_z$-SS plate during the synthesis process. Consequently, the $Zn:In(OH)_yS_z$-SSNs with smaller and uniform particle size are obtained when the SDS concentration was 26 mM (Fig. 4.7A). With the increase of concentration, SDS prefers to aggregate into spherical micelles (Rawat and Chattopadhyay, 1999). These spherical micelles have a property of encapsulating various salts in the solution, which eventually leads to the formation of spherical $Zn:In(OH)_yS_z$-SS nanoparticles (Fig. 4.7C).

4.4.2 Photocatalytic performances of different photocatalysts

Although ZnS is a UV-excited photocatalyst, it can easily be photosensitized by dyes (Zang et al., 1995). Thus it shows some photocatalytic activity during the degradation of RhB under visible light irradiation as shown in Fig.4.8. However, since the photoexcited electron of RhB cannot efficiently transfer to the CB of $In(OH)_3$, it shows no photocatalytic activity under visible light irradiation, which reveals that the effect of photosensitization of RhB is weak with the $In(OH)_3$ based semiconductor as photocatalysts. When OH^- in $In(OH)_3$ is partly substituted by S^{2-}, a visible-light response is induced by the excitations of electron from the new VB formed by the hybridization of O2p with S3p to the CB (Lei et al., 2006; Li et al., 2007). Therefore, the degradation efficiency of RhB was elevated with the $In(OH)_yS_z$-SSs as photocatalyst under visible light irradiation. Surprisingly, the incorporation of Zn^{2+} in $In(OH)_yS_z$-SS can largely enhance the VLD photocatalytic activity. The reasons will be illustrated in detailed in Section 4.4.4.

4.4.3 The effect of morphology and crystallinity

It is well known that the morphology and crystallinity can greatly influence the photocatalytic performance (Kamat, 1993; Zhang et al., 2006; Zhang et al., 2007). Regarding the highest photocatalytic activity of $Zn:In(OH)_yS_z$-SSNs prepared with 26 mM SDS (Fig. 4.9), there are two possible explanations. The first is that the ultrathin nanoplate structure allows the photogenerated holes and electrons inside the crystalline to transfer more easily to the surface, which facilitates the participation of

photogenerated charges in photocatalytic reactions (Zhang and Zhu, 2005). In addition, the previous study demonstrates that the high degree of crystallinity improves the photocatalytic performance of the photocatalyst due to the fewer defects on the surface to quench the photogenerated charges (Yu et al., 2005). As revealed in Figs. 4.3B and 4.4B, an increase of the SDS concentration reduces the degree of crystallinity of the solid solutions. Thus, the second important reason should be attributed to the higher crystallinity of the $Zn:In(OH)_yS_z$-SSN. Compared with the R-$Zn:In(OH)_yS_z$-SSs (BET surface area of 91.8 $m^2 g^{-1}$) (Lei et al., 2006) (Fig. 4.7D), the $Zn:In(OH)_yS_z$-SSNs (Fig. 4.7A) exhibit a much higher photocatalytic activity (Fig. 4.9). It is reasonable because the $Zn:In(OH)_yS_z$-SSNs prepared using SDS have smaller and uniform particle size, and larger BET surface area of 233.5 $m^2 g^{-1}$. The smaller article size can reduce the recombination of photogenerated charge carriers (Zhang et al., 2006), and the larger BET surface area benefits the adsorption of pollutants and can supply more active reaction sites for the degradation of a pollutant (Wang et al., 2005).

4.4.4 The photocatalytic mechanism

The light absorption capability and the potential positions of the VB and CB are crucial factors for the photocatalytic activity of semiconductors (Hoffmann et al., 1995; Li et al., 2007). The oxidative potential of VB holes in the $In(OH)_yS_z$ is only 1.8 V vs NHE, which cannot meet the redox potential of the $OH^-/\cdot OH$ ($OH^-=\cdot OH+e^-$, E=2.38 V) (Li et al., 2007). However, the photogenerated holes can oxidize organic

pollutants, and the consumption of the VB holes benefits the relative stability of the solid solutions (Li et al., 2007). In order to obtain a high photo-utilization rate, the level of the CB should be much more negative so that the photogenerated electrons have enough power to reduce the surface chemisorbed O_2, generating ROSs such as $\cdot O_2^-$ and $\cdot OH$. Fortunately, the energy level of Zn 4s4p is more negative than that of In 5s5p (Lei et al., 2006). With the Zn^{2+} incorporation, the new CB in the $Zn:In(OH)_yS_z$-SS introduced by the hybridization of the In 5s5p with Zn 4s4p will shift to a more negative energy level (Li et al., 2007). The more negative energy level of the CB facilitates the reduction of surface-absorbed oxygen to form more ROSs to degrade the organic pollutant. Therefore, the photocatalytic activities of $Zn:In(OH)_yS_z$-SSs are enhanced with an increase of the incorporation of Zn^{2+}. Remarkably, the maximum photocatalytic efficiency reaches 95.6% after 60 min when the X value is 0.6 (Fig. 4.10). However, the photocatalytic efficiencies quickly decreases with a higher ratio of Zn/In (X>0.7) due to less photoabsorption in the visible light range, which is reflected in the UV-VIS DRS (Fig. 4.6C).

As mentioned above, the holes, $\cdot O_2^-$ and $\cdot OH$ are considered to be major reactive species for the photocatalytic degradation of RhB. Several scavengers were employed to further confirm the specific reactive species that play important roles. Isopropanol is usually used as a diagnostic tools for $\cdot OH_b$ because it is easily oxidized by $\cdot OH$ and has low affinity to semiconductor surfaces in aqueous media (Chen et al., 2005; Khodja et al., 2005). However, the addition of isopropanol has negligible effect on the photocatalytic degradation of RhB. On the contrary, the

addition of sodium oxalate (hole scavenger) and KI (hole and $\cdot OH_s$ scavenger) can slow down the photocatalytic degradation of RhB, which indicates that the holes and $\cdot OH_s$ are involved in the photocatalytic degradation of RhB. Upon purging with nitrogen and the addition of Cr(VI), the role of species generated at the reduction site on the surface of photocatalyst such as $\cdot O_2^-$ and $\cdot OH_s$ could be ignored, since the photogenerated electrons are quenched by Cr(VI). Thus, in the presence of Cr(VI) and nitrogen, the photodegradation efficiency declined to 32% (Fig. 4.11). Therefore, it is concluded that, the holes, $\cdot O_2^-$ and $\cdot OH_s$ existing on the surface of Zn:In(OH)$_y$S$_z$-SSN are the major reactive species responsible for the photocatalytic degradation of RhB. Due to the strong oxidative ability of these reactive species, RhB can be degraded into the smaller molecules as identified by GC-MS, and even be further mineralized into inorganic species such as CO_2 and water (Fig. 4.16).

Moreover, according to the scavenger experiments, it is deduced that the photocatalytic degradation of RhB only occurs on the surface of the Zn:In(OH)$_y$S$_z$-SS. As expected, the greater adsorption of RhB by the Zn:In(OH)$_y$S$_z$-SS, the faster of the photocatalytic degradation of RhB (Fig. 4.13) is, which means that most of RhB is degraded on the surface of Zn:In(OH)$_y$S$_z$-SSNs.

In order to further investigate the effect of the direct contact between photocatalyst and pollutant, the partition setup was utilized, where the semi-permeable membrane allows the free diffusing of the smaller molecules such as the radicals and water, and the slow leakage of RhB, but it can prevent the entry of the photocatalyst. Thus, a minor portion of RhB in the container diffuses to the outside after placing for 60 min.

Once there are nanoparticles of photocatalyst in the outer suspension, the diffused RhB will be absorbed by these nanoparticles. While, these nanoparticles can not pass through the membrane to further influence the concentration of RhB in the container.

H_2O_2 is stable in the aqueous solution and can pass through the semi-permeable membrane due to its small molecule weight, but RhB has resistant ability to H_2O_2 (Fig. 4.14). It is well know that Fenton reagent is a aqueous solution consisted by H_2O_2 and Fe^{2+}, and is also a kind of homogenous system to generate the free •OH in the aqueous solution (Titus et al., 2004). Thus, the degradation of RhB in the container is probably due to the entry of the free •OH instead of H_2O_2 when the out system is Fenton reagent as shown in Fig. 4.14. When the water, TiO_2 and UV were used as outer system, the degradation of RhB in the outer system is reasonable because RhB in the outer system could be directly degraded by the ROSs generated by UV irradiated TiO_2 in outer system (Choi et al., 2001; Ishikawa et al., 2003). While the degradation of the RhB inside of the container only can be interpreted by the diffusion of ROSs generated by UV irradiated TiO_2 in outer system. This fact further reveals that some free ROSs generated during the photocatalytic process have the ability to pass through the semi-permeable membrane.

However, with the $Zn:In(OH)_yS_z$-SSNs, water and visible light as the outer system, RhB in the container is not degraded, which means most of ROSs generated by VLD $Zn:In(OH)_yS_z$-SSNs do not diffuse into the container. In contrast, RhB diffused from the inside of the container is effectively degraded by outer VLD $Zn:In(OH)_yS_z$-SSNs, indicating that only after the leaked RhB is absorbed onto the surface of

Zn:In(OH)$_y$S$_z$-SSNs, it can be photocatalytically degraded. These results provides a direct support to the assertion that the direct contact of Zn:In(OH)$_y$S$_z$-SSNs with RhB is necessary for the efficient photocatalytic degradation of RhB.

Based on the above results, the process of photocatalytic degradation of RhB by the Zn:In(OH)$_y$S$_z$-SSNs under visible light irradiation is proposed as Fig. 4.17. Under the visible light irradiation, electrons are promoted from the VB into the CB, leaving a hole. Although these photogenerated holes in the VB of Zn:In(OH)$_y$S$_z$-SSNs cannot oxidize OH$^-$ or H$_2$O into •OH, they can oxidize RhB adsorbed onto the surface of the catalyst, as shown in Step 2a in Fig. 4.17. On the other hand, the photogenerated electrons in the CB of Zn:In(OH)$_y$S$_z$ have strong reductive ability, and they can reduce the adsorbed oxygen into •O$_2^-$. Then, part of the •O$_2^-$ is transformed into •OH$_s$. These •O$_2^-$ and •OH$_s$, which are formed on the surface of Zn:In(OH)$_y$S$_z$-SSNs, also can degrade the adsorbed RhB, as indicated in Step 2b in Fig. 4.17. The location of these reactive species determines that photocatalytic degradation of RhB only occurs on the surface of Zn:In(OH)$_y$S$_z$-SSNs, which also explains why the morphology and BET area have great effects on the photocatalytic activity of Zn:In(OH)$_y$S$_z$-SSNs, as discussed previously. Because there are few reactive species in the aqueous solution, RhB in the aqueous solution cannot be degraded spontaneously. Only after the adsorbed RhB is degraded, can more RhB in the bulk solution be adsorbed onto the surface of Zn:In(OH)$_y$S$_z$-SSNs (Step 1 in Fig. 4.17) and further be degraded. In time, all of the RhB in suspension will be degraded to form smaller organic molecules, and these organic molecules can eventually be mineralized into CO$_2$ and H$_2$O.
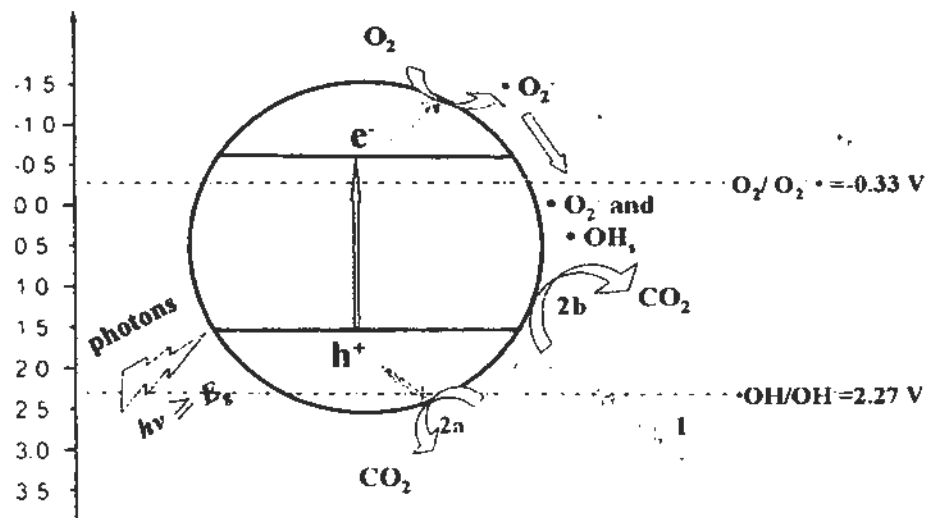
Fig.4.17 The schematic illustration of the process of photocatalytic degradation of RhB by the $Zn:In(OH)_yS_z$-SSNs under visible light.

4.5 Conclusions

$Zn:In(OH)_yS_z$-SSNs have been successfully synthesized via a hydrothermal method in an aqueous solution of SDS. The band.gap and redox potentials of CB and VB can be efficiently controlled by adjusting the substitution of S^{2-} for OH^- and the doping of Zn^{2+} in $Zn:In(OH)_yS_z$. The photocatalytic performances of the $Zn:In(OH)_yS_z$-SSs are also significantly influenced by the components, diameter size, morphologies and crystallinity. $Zn:In(OH)_yS_z$-SSNs (Synthesis conditions: 45 mM thiourea, 26 mM SDS, $0.4 \leq X \leq 0.7$) has the highest photocatalytic efficiencies, exceeding 92% for the degradation of RhB after 60 min under visible light irradiation. Furthermore, the photocatalytic mechanism indicates that holes, peroxide radicals and $\cdot OH_s$ are the main reactive species for the degradation of RhB. More importantly, for the first time, the direct contact between the $Zn:In(OH)_yS_z$-SS and RhB has been revealed to be a prerequisite for the photocatalytic degradation of RhB.

5. Photocatalytic disinfection of bacteria by AgBr-Ag-Bi$_2$WO$_6$ nanojunction under visible light

5.1 Introduction

Millions of deaths and many millions of cases of disease are caused by microbial contaminations and infections every year (Shannon et al., 2005). Especially, the bursting of *Clostridium difficile*, the occurrence of SARS, and the return of influenzas become pervasive problems afflicting people throughout the world these years (Chung et al., 2008).

Disinfection by aggressive chemicals such as detergents, chlorine and chloramines is most widely used method for controlling microbial contaminations and infections (Gopal et al., 2007). However, disinfection byproducts (DBPs) such as halogenated trihalomethanes and haloacetic acids will generate during this disinfection process (Gopal et al., 2007). These DBPs are probably carcinogenic and mutagenic, which will cause an unintended health hazard to human (Hua and Reckhow, 2007; Sciacca and Conti, 2009). In addition, the aggressive chemicals are also ineffective for long-term (Erkan et al., 2006). Although the UV-C radiation is capable of sustained disinfection and do not produce DBPs, disinfection only can be conducted by the direct irradiation due to its weak penetration (Kühn et al., 2003). The direct irradiation of UV-C can cause the skin caner and blindness on human (Parson, 2004), which limits its application to medical and technical purposes only (Erkan et al., 2006). Hence, it is necessary and urgent to develop alternative methods for controlling and/or eradicating the harmful microorganisms.

Since Matsunaga et al. (1985) reported for the first time the bactericidal effect of the TiO_2 photocatalysis in 1985, the photocatalytic destruction of microorganisms has become a subject attracting much research interest (Sunada et al., 1998; Blake et al., 1999; Kühn et al., 2003; Hu et al., 2006). However, TiO_2 can only be activated by wavelengths in the near-UV region ($\lambda < 400$ nm) and cannot efficiently utilize the major part of sunlight to photocatalytically disinfect the microorganisms. Therefore, the development of the visible-light-driven (VLD) photocatalysts for microbial disinfection seems to be a promising way from the viewpoint of using solar energy. Up to date, several kinds of VLD photocatalysts, such as doped or sensitized TiO_2 (Asahi et al., 2001; Zhang et al., 2008), aurivillius oxides (Tang et al., 2004; Zhang et al., 2005; Zhang et al., 2007), and some other composites (Liu et al., 2009), have been prepared for the degradation of organic pollutants. Only a few of them are applied to the photocatalytic disinfection of microorganisms under VL irradiation (Yu et al., 2005; Hu et al., 2006; Li et al., 2008; Ren et al., 2009). Furthermore, the efficiencies of VLD photocatalytic disinfection also need to be greatly improved to deal with the outbreak of harmful microorganisms and to meet the high requirements of future environmental and energy problems.

Although reactive oxygen species (ROSs) including hydroxyl radical ($\cdot OH$), superoxide radical ($\cdot O_2^-$) and hydrogen peroxide (H_2O_2) generated by UV-irritated TiO_2 have been revealed to be responsible for the disturbance or destruction of microorganisms (Maness et al., 1999; Cho et al., 2005), the fundamental mechanism underlying the VLD photocatalytic disinfection process has not been well-established

yet. For examples, little is known about the exact role(s) of the ROSs and whether they remain bound to the surface or diffuse into the solution bulk.

Recently, we have prepared several VLD photocatalysts including Bi_2O_3 (Zhang et. al., 2006), Bi_2WO_6 (Zhang et al., 2007), and $AgBr-Ag-Bi_2WO_6$ nanojunction (Zhang et al., 2009) for the photocatalytic degradation of organic pollutants, where $AgBr-Ag-Bi_2WO_6$ nanojunction is the most promising due to its double VL active components (AgBr and Bi_2WO_6) and the electron-transfer component (Ag). For a photocatalyst, it is known that there is strong correlation between the antimicrobial effect and the organic compound degradation effect (Chen et al., 2009). Herein, I further investigated the photocatalytic disinfection of kinds of bacteria, especially *E. coli* K 12, a most commonly target microorganism, by using $AgBr-Ag-Bi_2WO_6$ nanojunction as a VLD photocatalyst. Scavengers for different kinds of ROSs were employed to investigate the roles of these species in the photocatalytic disinfection process. In particular, the partition setup reported in chapter 4 (Zhang et al., 2009) had been modified in this work to confirm whether the direct contact between $AgBr-Ag-Bi_2WO_6$ nanojunction and the bacterial cells was a prerequisite for the photocatalytic disinfection of bacteria.

5.2 Materials and methods

5.2.1 Materials

Bi_2WO_6, $Ag-Bi_2WO_6$, $AgBr-Ag-Bi_2WO_6$ nanojunction and $AgBr-Ag-TiO_2$ were prepared according to Section 3.2.1. Nutrient agar (NA) plates were prepared for freshwater bacteria by dispersing 28 g nutrient agar (Lab M®, Lancashire, UK) into 1 L Milli-Q® water, whereas additional 30 g artificial sea salt purchased from Aquarium system (Sarrebourg, France) was added for marine bacteria. Then, it was sterilized by autoclaving at 121°C for 30 min and poured into the sterile Petri-dish after well-mixing. 10% nutrient broth (NB) solution was prepared for freshwater bacteria including *Escherichia coli* K 12 (*E. coli* K 12), *Escherichia coli* BW 25113(*E. coli* BW 25113) and *Pseudomonas fluorescens* 85070 (*P. fluorescens* 85070) by dissolving 0.04 g Difco™ nutrient broth (Becton, Dickinson and company, Sparks, USA) into 50 mL Milli-Q® water. 100% marine broth (MB) was prepared for marine bacteria, *Alteromonas macleodii* (*A. macleodii*) by dissolving 1.87 g Difco™ marine broth (Becton, Dickinson and company, Sparks, USA) into 50 mL Milli-Q® water. The nutrient solutions were then autoclaved for 30 min at 121°C and cooled to room temperature before use. 0.9 and 3.0% sodium chloride (NaCl) solutions were prepared by dissolving 9 and 30 g NaCl powder (Riedel-de Haën®, Seelze, Germany) into 1 L Milli-Q® water, respectively. They were also sterilized by autoclaving at 121°C for 30 min and cooled to room temperature before use.

For the preparation of reaction mixture, suitable amount of photocatalyst was homogenized by sonication in 45 mL NaCl solution (0.9% for freshwater bacteria

and 3% for marine bacteria) with a Branson 2510 sonicator (Branson Ultrasonics B. V., Soest, NL, USA) (Plate 3.5) at 35 kHz for 1 min before adding the bacteria.

5.2.2 Preparation of bacteria culture

Three freshwater bacterial stains, *Escherichia coli* K 12 (Plate 5.1A), *Escherichia coli* BW 25113 (Plate 5.1B) and *Pseudomonas fluorescens* 85070 (Plate 5.1C), and one marine bacterium, *Alteromonas macleodii* (Plate 5.1D) were chosen for the study.
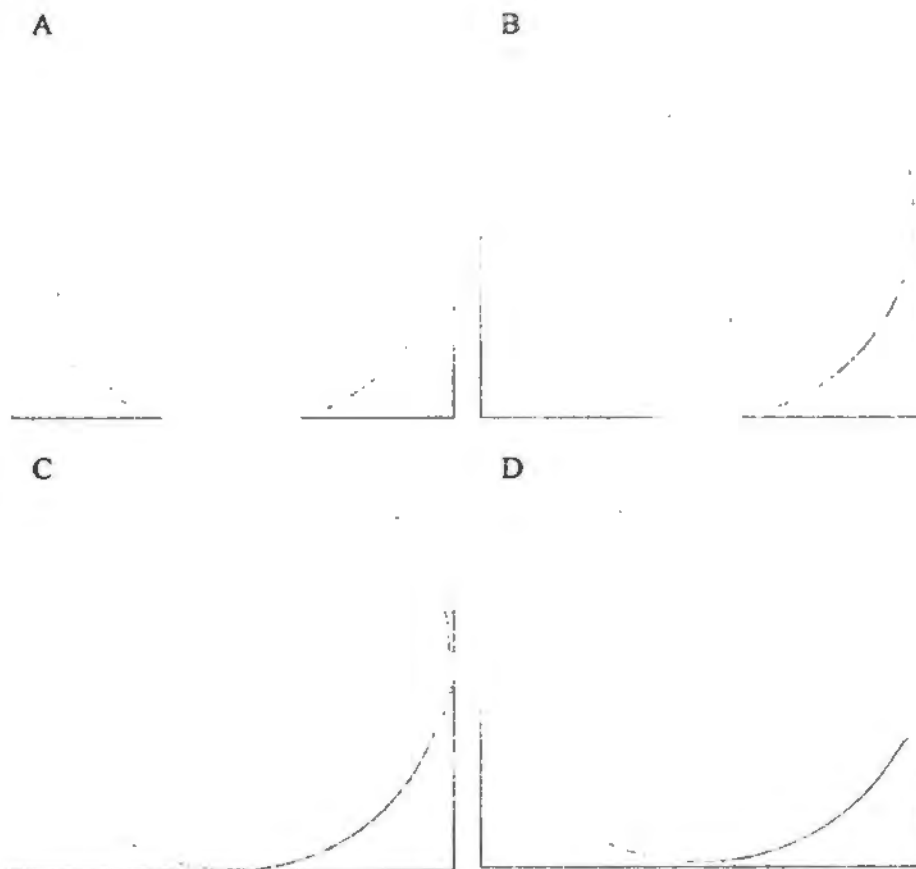
Plate 5.1 The used bacterial strains: (A) *Escherichia coli* K 12, (B) *Escherichia coli* BW 25113, (C) *Pseudomonas fluorescens* 85070, and (D) *Alteromonas macleodii*.

One single pure bacterial colony grown on the NA and Marine agar (MA) plates were inoculated into 10% NB (for freshwater bacteria *E. coli* K 12, *E. coli* BW 25113, *P. fluorescens* 85070) and 100% MB (for marine bacteria, *A. macleodii*), respectively. After cultured at 30°C with 200 rpm agitation for 16 h (for *E. coli* K 12, *E. coli* BW 25113, *P. Fluorescens* 85070) and for 20 h (for *A. macleodii*), the bacterial cells were washed twice with sterilized 0.9% (for freshwater bacteria) and 3.0% (for marine bacteria) NaCl solutions by centrifugation at 24,000 x g for 5 min using a Hermle Z323 centrifuge. The cell pellet was re-suspended in NaCl solution and the cell density was measured by a Helios Gamma UV-VIS spectrophotometer (Thermo Electro, England) (Plate 3.17).

5.2.3 Photocatalytic reactor

The photocatalytic disinfection process was carried out by using a 300 W Xenon lamp (PLS-SXE-300, Beijing Perfect Light Co. Ltd., Beijing) as a light source (Plate 3.14). Light was also passed through a UV cut-off filter ($\lambda \geq 400$ nm), and then was focused onto a flask containing a bacterial cell suspension and photocatalyst or the partition setup as shown in Fig. 5.1. The visible light intensity was fixed at 190 mW cm^{-2}. The photocatalyst and the suspension of washed cell were added into a flask covered by an aluminum cover. The reaction temperature was maintained at 25°C and the reaction mixture was stirred with a magnetic stirrer throughout the experiment.

5.2.4 Photocatalytic disinfection efficiencies test

At the different stages of photocatalytic oxidation (PCO) process, an aliquot of the reaction solution was sampled and immediately diluted with sterilized 0.9 or 30% NaCl solution for freshwater and marine bacteria, respectively; and an appropriate dilution of the sample was spread on NA or MA agar plate and incubated at 30°C for 24 h. The number of colonies formed was counted to determine the number of viable cells.

5.2.5 Photocatalytic disinfection performances of different photocatalysts

Four kinds of photocatalysts including Bi_2WO_6, $Ag-Bi_2WO_6$, $AgBr-Ag-Bi_2WO_6$ nanojunction and $AgBr-Ag-TiO_2$ were used in this study. The reaction mixtures of these photocatalysts were prepared by adding the corresponding amount of photocatalyst with same amount of VLD component into 45 mL sterilized 0.9% (for freshwater bacteria) and 3.0% (for marine bacteria) NaCl solution and homogenized by sonication. Then, 5 mL washed bacterial cells suspension with suitable density was added in the reaction mixture. The following procedures were the same as described in Sections 5.2.3 and 5.2.4. All the above experiments were conducted in triplicates.

5.2.6 Effect of scavengers

The scavenger experiments were carried out by adding individual scavenger to 50 mL reaction mixture containing about 5×10^7 cfu mL^{-1} *E. coli* K 12 and 100 mg L^{-1}

AgBr-Ag-Bi$_2$WO$_6$ nanojunction before the irradiation. The concentrations of individual scavengers are 0.05 mM Cr(VI) for the quenching of electron (e$^-_{CB}$), 0.3 M isopropanol (Riedel-de Haën$^®$, Seelze, Germany) for the scavenging of bulky •OH (•OH$_b$), 30 µM sodium oxalate for the scavenging of hole (h$^+_{VB}$), 2 µM Fe(II)-EDTA for the detection of hydrogen peroxide (H$_2$O$_2$). 100 mL stock solutions of 5 mM Cr(VI) and 3 mM sodium oxalate were respectively prepared by dissolving 0.074 g K$_2$Cr$_2$O$_7$ (Merck, Darmstadt, Germany) and 0.04 g sodium oxalate (Peking Chemical Industrial Factory, Beijing, China) in saline solution. 100 mL stock of 2 mM Fe(II)-EDTA solution was prepared dissolving 0.034 g Iron (II) sulfate (FeSO$_4$) (90%, Ajax Chemicals, Sydney, Australia) with 0.037g ethylenediaminetetraacetic disodium salt (Na$_2$EDTA) (Ajax Chemicals, Sydney, Australia) into saline solution. All the above experiments were conducted in triplicates.

5.2.7 The partition setup

The separated experiments were also carried out using the partition setup constructed in Chapter 4 by replacing 20 mL Rhodamine B (RhB) solution inside of the container with a 20 mL suspension of bacterial cells with initial cell density of about 5×10^7 cfu mL^{-1} in NaCl solution, and replacing 50 mL suspension with 10 mg Zn:In(OH)$_y$S$_z$-SSNs in Milli-Q$^®$ water by 50 mL suspension with 5 mg AgBr-Ag-Bi$_2$WO$_6$ nanojunction in NaCl solution as shown in Figure 5.1. At the different PCO stages, 1 mL suspension inside of the container was sampled and immediately diluted to determine the density of living cells by counting the cfu mL^{-1}.

For comparison, the disinfection effect in this partition setup was also investigated when the outer system was replaced by Fenton reagent. The preparation of the Fenton reagent is similar with that described in Section 4.2.7 except for that the Fenton reagent are prepared in saline solution. All the above experiments were conducted in triplicates.
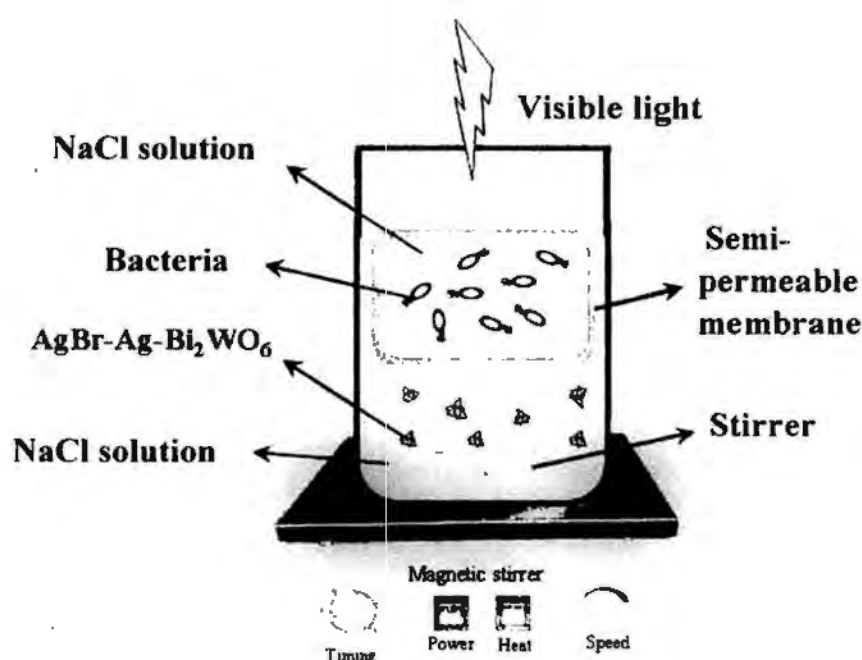
Fig. 5.1 The schematic illustration of partition setup for the disinfection of the bacteria.

5.2.8 Fluorescence spectroscopy

The viability of the *E. coli* K 12 at different stages of the AgBr-Ag-Bi$_2$WO$_6$ nanojunction mediated PCO process was examined by the LIVE/DEAD BacLight^{TM} bacterial viability kit L7012 (Invitrogen^{TM}, Molecular Probes, Inc., Foster City, USA) (Plate 5.2). Kit Contents for Viability Kit, L7012 are 300 μL 3.34 mM SYTO 9 dye solution in dimethyl sulfoxide (DMSO) (as Component A) and 300 μL 20 mM

Propidium iodide solution in DMSO (as component B). With an appropriate mixture of the SYTO® 9 green-fluorescent nucleic acid and the red-fluorescent nucleic acid stain, propidium iodide stains, bacteria with intact cell membranes give out green fluorescence, whereas bacteria with damaged membranes emit red fluorescence. The Viability Kit is stored frozen at -20°C and protected from light. According to procedures recommended by the manufacturer, the kit should be firstly allowed to warm to room temperature and centrifuged briefly before opening the vials. Combine equal volumes of component A and component B and mix them thoroughly in a microfuge tube. At the same time, 40 mL suspensions containing $AgBr-Ag-Bi_2WO_6$ nanojunction and bacterial cells of *E. coli* K 12 at different stages of the PCO process were sampled and concentrated by the centrifugation at 24,000 x g for 5 min. Remove the supernatant and re-suspend the pellet in 2 mL of 0.9% NaCl solution. Add 3 μL of the dye mixture for each mL of the above concentrated suspension. Mix the resulting mixture thoroughly and incubate it at room temperature in the dark for 15 minutes. After trapped 5 μL of the stained suspension between a slide and an 18 mm square cover slip, the stained bacteria were observed in a fluorescence microscope (Nikon ECLIPSE 80i, Tokyo, Japan) equipped with a filter block N UV-2A consisting of excitation filter Ex 330-380 nm (Nikon, Tokyo, Japan) and Spot-K slider CCD camera (Diagnostic instruments. Inc., Sterling Heights, USA) (Plate 5.3).
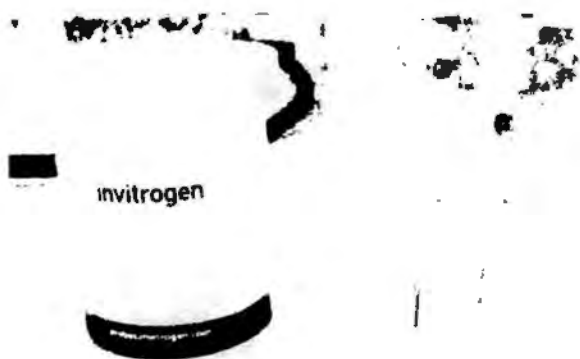
Plate 5.2 The LIVE/DEAD BacLight™ bacterial viability kit L7012 (Invitrogen™, Molecular Probes, Inc., Sterling Heights, USA)

Plate 5.3 A fluorescence microscope (Nikon ECLIPSE 80i, Tokyo, Japan) equipped with a filter block N UV-2A and Spot-K slider CCD camera.

5.2.9 Electron paramagnetic resonance spectrometry

To identify the generated ROSs during the AgBr-Ag-Bi$_2$WO$_6$ nanojunction mediated PCO process, electron paramagnetic resonance (EPR) signals of radicals spin-trapped by 5, 5-Dimethyl-1-pyrroline-N-oxide (DMPO) were recorded at ambient temperature on electron paramagnetic resonance spectrometer (Brucker EPR 300E spectrometer, Rheinstetten, Germany) (Plate 5.4). DMPO spin-trap reagent was purchased from Sigma Chemical Co. ($\geq$97%, Sigma-Aldrich, St. Louis, USA). Stock

solutions of DMPO (0.4 M) in degassed water or methanol (BDH Chemicals Ltd., UK) were prepared under argon and stored in the dark at -20°C before use. The irradiation source was a Quanta-Ray Nd:YAG pulsed laser system (λ= 532 nm, 10 Hz). The settings for the ESR spectrometer were as follows: center field, 3480.00 G; sweep width, 100 G; microwave frequency, 9.79 GHz; modulation frequency, 100 kHz; power, 5.05 mW (Hu et al., 2006). To minimize experimental errors, the same quartz capillary tube was used for all EPR measurements. Magnetic parameters of the radicals detected were obtained from direct measurements of magnetic field and microwave frequency.
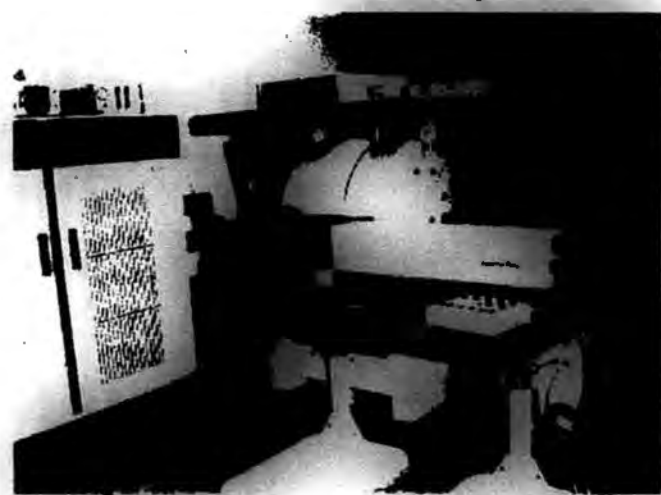
Plate 5.4 The electron paramagnetic resonance spectrometer (Brucker EPR 300E spectrometer, Rheinstetten, Germany)

5.2.10 Transmission electron microscopy (TEM)

In order to study the change of morphology and structure of the bacterial cells, and thus understanding the disinfection mechanisms, TEM images of E. coli K 12 during different stages of the AgBr-Ag-Bi$_2$WO$_6$ nanojunction mediated PCO process was

observed. 300 mL reaction mixture containing initial cell concentration of 2×10^8 cfu mL^{-1} with 200 mg L^{-1} AgBr-Ag-Bi$_2$WO$_6$ nanojunction was used under PCO treatment. 40 mL mixture at different time intervals was taken and centrifuged to get the pellet. After obtaining the cell pellet, the bacterial cells were prefixed by adding 2.5% glutaraldehyde (E.M. grade, Electron Microscopy Sciences, Hatfield, PA, USA) at 4°C for 2 h, Then the samples was washed twice with 0.1 M phosphate buffer saline (PBS) at pH 7.2 by centrifugation. The cell suspensions were trapped in 3% low melting point agarose (Sigma-Aldrich, St. Louis, USA) and the solidified encapsulated pellets were cut into small cubes with diameter less than 1 mm by a razor blade. Those small cell cubes were then post-fixed by 1% osmium tetraoxide in PBS (E.M. grade, Electron Microscopy Sciences, Hatfield, PA, USA) with stirring for 2 h in dark. After that, the cell pellets were washed twice with PBS and then dehydration was performed by adding a graded series of ethanol (50, 70, 85, 95 and 100%) into the solidified cell cubes. The small cell pellets were embedded in Spurr solution (E.M. grade, Electron Microscopy Sciences, Hatfield, PA, USA) for polymerization at 68°C for 24 h. By using ultra-microtome (Leica, Reichert Ultracuts, Wien, Austria) with diamond knife (DiATOME *ultra 45°*, Diatome Ltd., Biel, Switzerland) (Plate 5.5), Ultra-thin sections of 70 nm were made and placed on copper mesh grids with chloroform coating. They were then stained with 2.5% uranyl acetate and 2% lead citrate for contrast enhancement. Then the stained ultra-thin sections were examined by a H-7650C transmission electron microscope (Hitachi Ltd, Tokyo, Japan) (Plate 5.6) at 80 kV accelerating voltage.

Plate 5.5 (A) An ultra-microtome (Leica, Reichert Ultracuts, Wien, Austria) and (B) A diamond knife (DiATOME *ultra 45°*, Diatome Ltd., Biel, Switzerland)

Plate 5.6 A H-7650C transmission electron microscope (Hitachi Ltd, Tokyo, Japan)

5.2.11 Atomic absorption spectrophotometry (AAS)

To determine the silver ion (Ag^+) eluted from $AgBr$-Ag-Bi_2WO_6 nanojunction and potassium ion (K^+) leakage from the bacterial cells during the photocatalytic disinfection process, the $AgBr$-Ag-Bi_2WO_6 nanojunction/bacterial cell suspension

before and after PCO treatment was respectively collected and filtered through a Millipore filter with pore size of 0.45 μm (Millipore corporation, Ireland). After filtration, the solution was acidified with 3 M HNO₃, and Ag⁺ or K⁺ concentration was measured by a Z-2300 polarized Zeeman atomic absorption spectrophotometer (Hitachi High-Technologies, Tokyo, Japan) (Plate 5.7). All the above experiments were also conducted in triplicates.
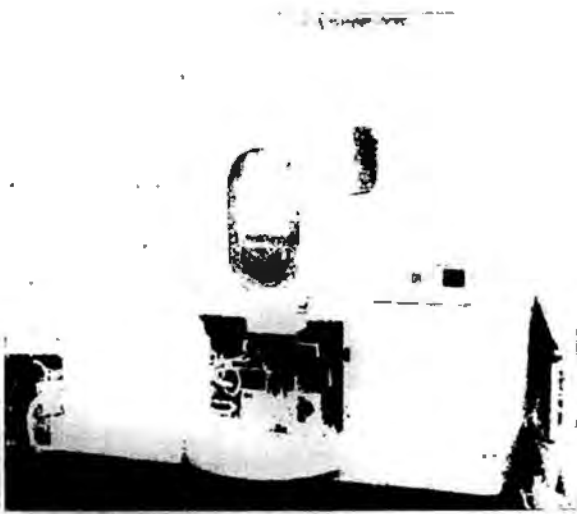
Plate 5.7 A Z-2300 polarized Zeeman atomic absorption spectrophotometer (Hitachi High-Technologies, Tokyo, Japan)

5.3 Results

5.3.1 Photocatalytic disinfection performance

E. coli K 12, a common waterborne pathogenic microorganism, was chosen as a representative microorganism to evaluate the photocatalytic disinfection performance of the photocatalyst. Before investigating the inactivation performances of different photocatalysts, control experiments were carried out. As shown in Fig.5.2A, the amount of viable cells of *E. coli* K 12 remained constant (about 5×10^7 cfu mL⁻¹) in

30 min when they were stirred at dark in a saline solution (Negative control) or in the reaction mixture containing each photocatalyst with the same weight of each VLD component (AgBr or Bi_2WO_6) (Dark control). It indicates that saline solution and the employed photocatalysts including AgBr-Ag-Bi_2WO_6, Ag-Bi_2WO_6, Bi_2WO_6 and AgBr-Ag-TiO_2 do not affect the survival of *E. coli* K 12, and therefore the employed photocatalysts itself have no toxic effect on the *E. coli* K 12. When the cells of *E. coli* K 12 were irradiated by visible light with intensity of 190 mW cm^{-2} for 30 min in saline solution without photocatalyst (Light control), the amount of viable cells also did not change, which demonstrates that *E. coli* K 12 is resistant to the light of Xenon lamp under the intensity employed in this project.

Fig. 5.2B shows the photocatalytic inactivation efficiencies of *E. coli* K 12 by different photocatalysts with the same weight of each VLD component under visible light irradiation ($\lambda \geq$ 400 nm). When Bi_2WO_6 was irradiated by visible light, it exhibited low bactericidal activity and only 0.19-log reduction in the vial cells count was obtained after 30 min. Although, Ag-Bi_2WO_6 and AgBr-Ag-TiO_2 samples have higher bactericidal activities under visible light irradiation, only 0.4 and 1 log inactivation were achieved within 30 min, respectively. Surprisingly, when employing AgBr-Ag-Bi_2WO_6 nanojunction as photocatalyst, 5×10^7 cfu mL^{-1} of *E. coli* K 12 was completely inactivated within 15 min under visible light irradiation (Fig. 5.2B). Therefore, AgBr-Ag-Bi_2WO_6 nanojunction has the highest VLD photocatalytic inactivation performance, far exceeding those of Bi_2WO_6 superstructure, Ag-Bi_2WO_6 and AgBr-Ag-TiO_2 composite.
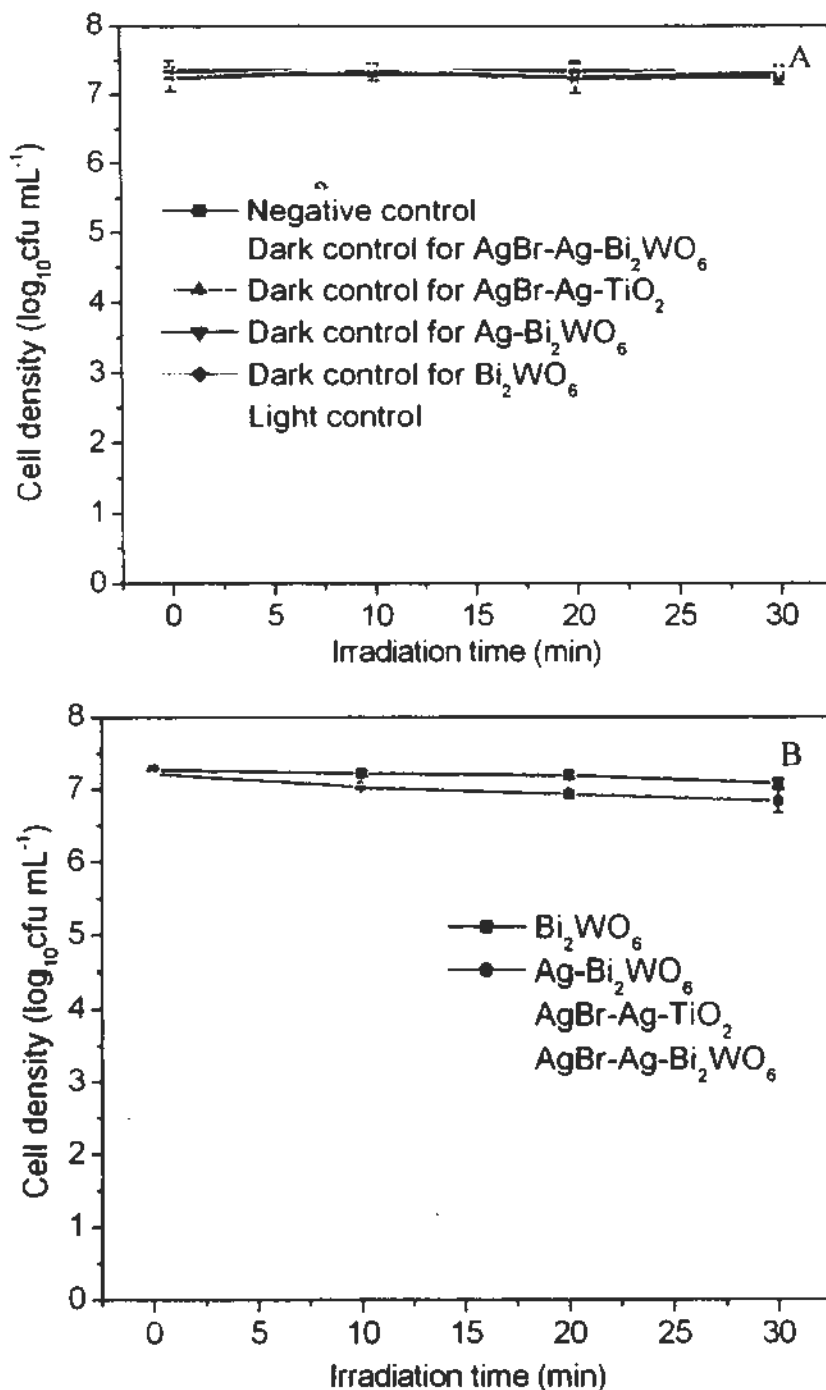
Fig. 5.2 The survivals of *E. coli* K 12 under control experiments (A) and PCO inactivation of *E. coli* K 12 in aqueous dispersions containing different catalysts with the same weight of each VLD component under visible light (B). The density of *E. coli* K 12 is ~5×10^7 cfu mL^{-1}. The amounts of photocatalysts in the dark controls and PCO process are 4.78 mg of Bi_2WO_6, 4.9 mg of Ag-Bi_2WO_6 containing 4.78 mg Bi_2WO_6, 5.55 mg of $AgBr$-Ag-TiO_2 composite containing 0.152 mg AgBr, and 5 mg of $AgBr$-Ag-Bi_2WO_6 nanojunction containing 0.152 mg AgBr and 4.78 mg Bi_2WO_6, respectively. Each data point and error bar represents the mean and the standard deviations of independent triplicates respectively.

When the AgBr-Ag-Bi$_2$WO$_6$ nanojunction was immerged in water or in suspension of the bacterial cells, there was trace amount of Ag$^+$ (about 0.55 mg L^{-1}) eluting from AgBr-Ag-Bi$_2$WO$_6$ nanojunction. But there was no more Ag$^+$ leakage even after 5 h photocatalytic reaction. More importantly, no obvious bactericidal effect was observed in the presence of 0.6 mg L^{-1} Ag$^+$ even after 2 h (Fig. 5.3).
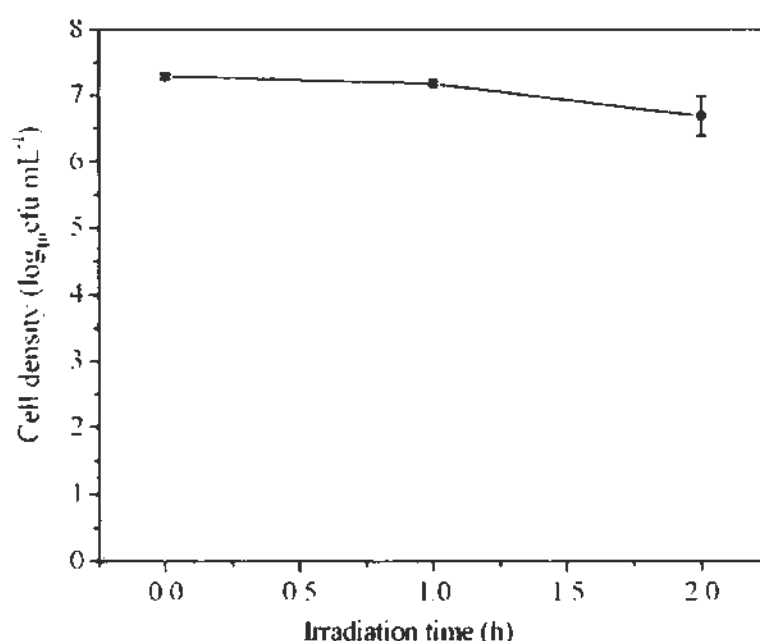
Fig. 5.3 Temporal course of the *E. coli* K 12 inactivation (~5×10^7 cfu mL^{-1}, 50 mL) in aqueous dispersion containing 0.6 mg L^{-1} Ag$^+$. Each data point and error bar represents the mean and the standard deviations of independent triplicates respectively.

In order to further confirm the photocatalytic disinfection effect of *E. coli* K 12 by AgBr-Ag-Bi$_2$WO$_6$ nanojunction under visible light irradiation, the fluorescence assays of photocatalytically untreated and treated *E. coli* K 12 have been investigated. During the process of this assay, these photocatalytically untreated and treated cells

were stained with the mixtures of SYTO 9 green-fluorescent nucleic acid stain and the red-fluorescent nucleic acid stain, propidium iodide, which are typical cell-labeling dyes respectively for the detection of living and dead bacteria. Fig. 5.4 shows the fluorescence microscopic images of $E.\ coli$ K 12 photocatalytically untreated or treated with $AgBr-Ag-Bi_2WO_6$ nanojunction under visible light irradiation with the time. After stained with these dyes, $AgBr-Ag-Bi_2WO_6$ nanojunction alone could not avoid giving out an orange colored fluorescence (Fig. 5.4A). Notably, except the orange fluorescence emitted by the photocatalyst, all of the photocatalytically untreated bacteria exhibited intense green fluorescence as demonstrated in Fig. 5.4B, indicating that all of the bacteria were living. After photocatalytically treated for 1 min, some bacteria gave out red fluorescence, indicating that parts of bacteria were dead (Fig. 5.4C). After 2-min treatment of VLD photocatalysis, the portion of red colored bacterial cells greatly increased as shown in Fig. 5.4D, revealing that the numbers of dead $E.\ coli$ K 12 increased. Moreover, after 2-min treatment, large amount of bacterial cells exhibited the yellow color because most of $E.\ coli$ K 12 was dying and both of dyes could penetrate the cell wall. After 5-min treatment, only few green colored bacteria were observed (Fig. 5.4D), which indicates that most of the bacteria were disinfected by the $AgBr-Ag-Bi_2WO_6$ mediated VLD photocatalytic process. Eventually, no living bacteria were found after 10 min (Fig. 5.4F). In fact, only about 0.1 and 0.001% bacterial cells, which are calculated according to the data of Fig. 5.2B, were survived after photocatalytically treated for 5 and 10 min, respectively.
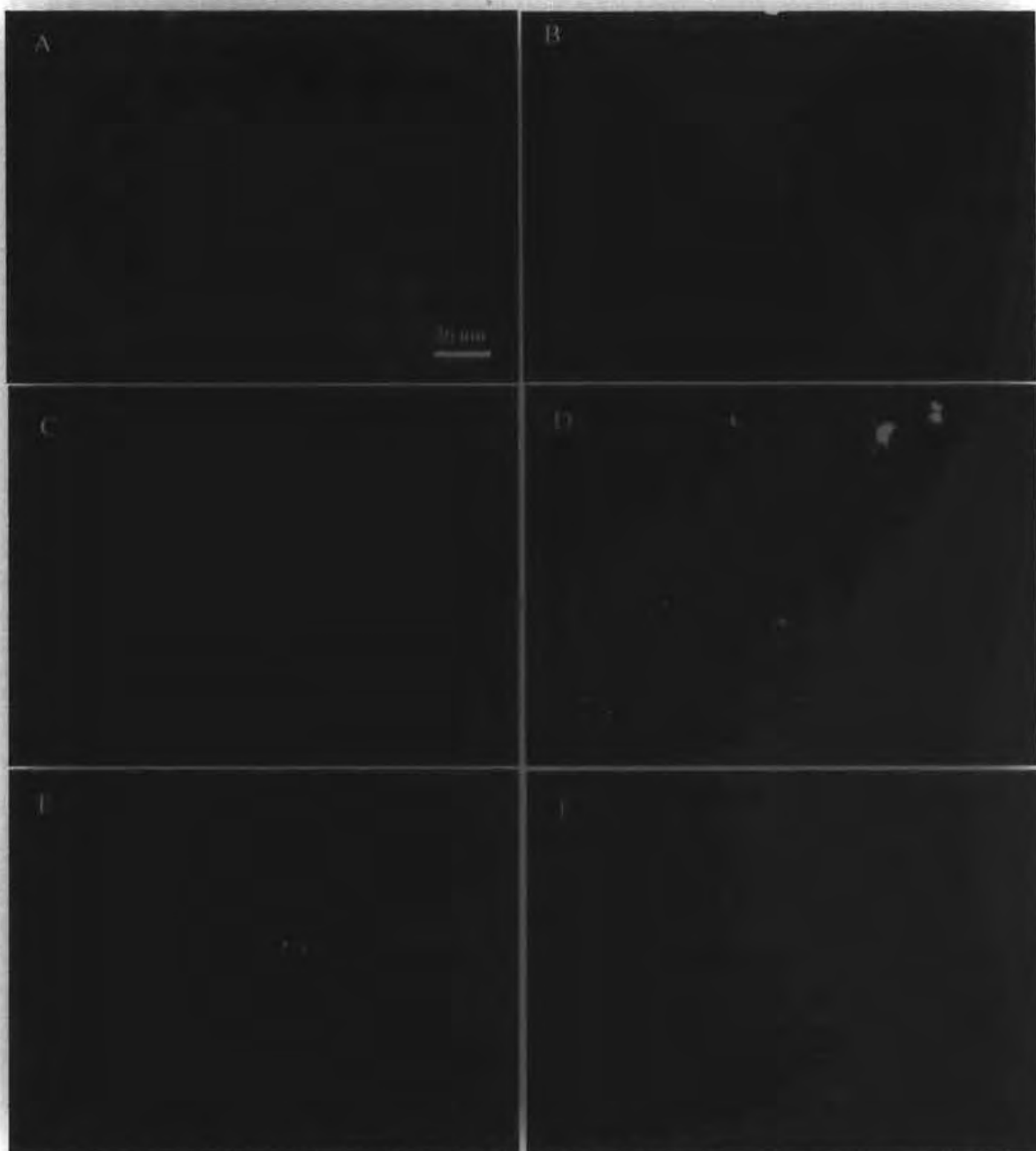
Fig. 5.4 Fluorescence microscopic images of *E. coli* K 12 ($\sim 5 \times 10^7$ cfu mL^{-1}, 50 mL) photocatalytically untreated or treated with 5 mg of AgBr-Ag-Bi$_2$WO$_6$ nanojunction under visible light irradiation. Only AgBr-Ag-Bi$_2$WO$_6$ nanojunction (A), The mixture of photocatalyst and *E. coli* K 12 before irradiation (B) and after irradiated by visible light for 1 min (C), 2 min (D), 5 min (E) and 10 min (F).

5.3.2 Photocatalytic disinfection mechanism

5.3.2.1 The ROSs in the photocatalytic disinfection process

The ESR spin-trap technique (with DMPO) was first used to obtain information on the active radicals involved in irradiated or unirradiated $AgBr-Ag-Bi_2WO_6$ nanojunction dispersion. Fig. 5.5 displays DMPO spin-trapping ESR spectra recorded at ambient temperature in $AgBr-Ag-Bi_2WO_6$ nanojunction suspension under visible light irradiation or in dark. Since $\cdot O_2^-$ in water is very unstable and undergoes facile disproportionation rather than slow reaction with DMPO (Ma et al., 2003), the involvement of $\cdot O_2^-$ was examined in methanol (Fig. 5.5A). From Fig. 5.5A, the six characteristic peaks of the DMPO-$\cdot O_2^-$ adducts were observed in visible light irradiated $AgBr-Ag-Bi_2WO_6$ nanojunction dispersion. While, no $\cdot O_2^-$ signal was detected in dark under otherwise identical conditions. Similarly, the four characteristic peaks of DMPO-$\cdot OH$ (1:2:2:1 quartet pattern) were also observed only in visible light irradiated aqueous suspension of $AgBr-Ag-Bi_2WO_6$ nanojunction (Fig. 5.5B). These facts confirm that $\cdot OH$ and $\cdot O_2^-$ can be generated by the $AgBr-Ag-Bi_2WO_6$ nanojunction mediated photocatalytic process.
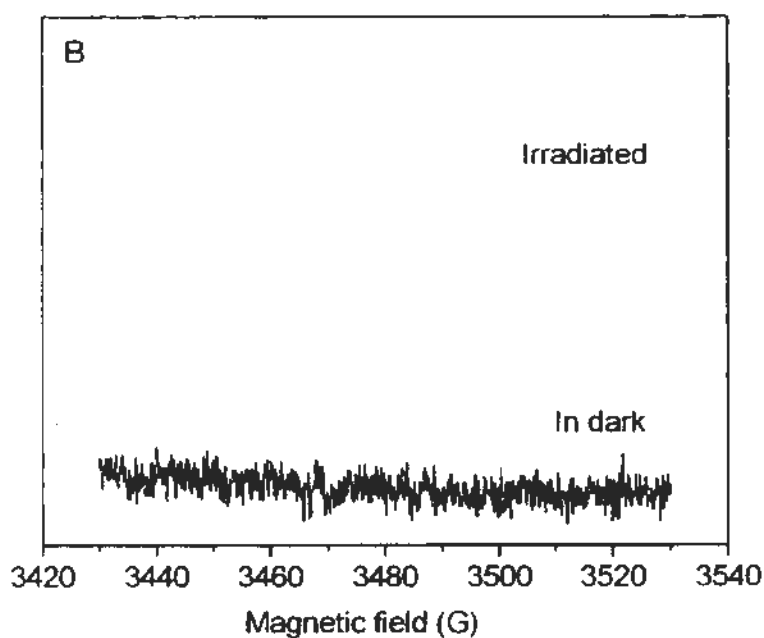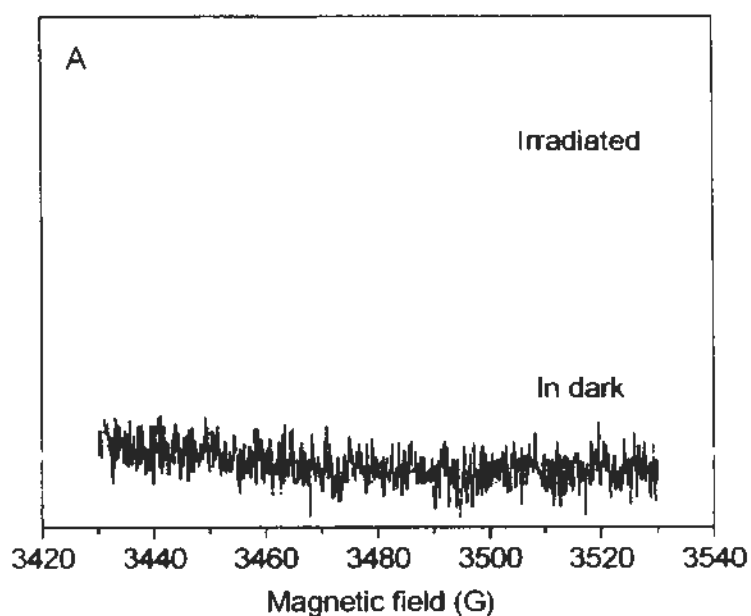
Fig.5.5 DMPO spin-trapping ESR spectra recorded at ambient temperature in AgBr-Ag-Bi$_2$WO$_6$ nanojunction suspension under visible light irradiation (λ=532 nm): (A) DMPO-•O$_2^-$ in methanol dispersion, and (B) DMPO-•OH in aqueous dispersion.

Here, the scavenger experiments were also conducted to detect ROSs generated during this photocatalytic process and to further investigate the exact kind(s) of ROSs playing significant role(s) in the disinfection process. During the PCO process, •OH can be detected by suppressing the •OH-mediated process with alcohol scavenger (Chen et al., 2005; Khodja et al., 2005), the oxidative pathway can be testified by the hole scavenger of sodium oxalate (Jin et al., 2004), ROSs generated at the reduction site can be eliminated by an electron scavenger of Cr(VI) (Chen et al., 2005), and photocatalytically generated H_2O_2 can be examined by enhancing the generation of the bulk phase free •OH by reacting photocatalytically generated H_2O_2 with Fe(II) (Khodja et al., 2005).

Before the testing of the specific ROSs using the above scavenger, the control experiments were also conducted to check the toxicity effect of each of these scavengers with as-mentioned concentration on *E. coli* K 12 within 15 min as shown in Fig. 5.6A. The control experiments show that the intensity of cells remained constant with the addition of each of these scavengers with as mentioned concentration either in the reaction mixture containing $AgBr-Ag-Bi_2WO_6$ nanojunction under the dark condition or in the bacterial cells suspension irradiated by the visible light, indicating that the scavenger itself do not affect the survival of *E. coli* K 12.

Fig. 5.6B demonstrates the photocatalytic disinfection of *E. coli* K 12 by $AgBr-Ag-Bi_2WO_6$ nanojunction with the addition of each kind of scavengers. Without any scavenger, the density of *E. coli* K 12 sharply declined from ~5×10^7 to 2

cfu mL^{-1} after 15-min photocatalytic treatment (Fig. 5.6B). In the presence of sodium oxalate (a hole scavenger), the density of *E. coli* K 12 only declined to 6×10^4 cfu mL^{-1} after 15 min irradiation, indicating the involvement of •OH generated by the oxidative pathway in the photocatalytic disinfection. With the addition of Cr(VI) (a electron scavenger), the density of *E. coli* K 12 also only dropped to 2×10^3 cfu mL^{-1} after 15 min, which results from the fact that the ROSs generated by the reductive pathway can disinfect the bacteria. For the detection of H_2O_2, Fe^{2+} was used to improve the generation of the bulk phase •OH and therefore enhance the inactivation path. In this case, however, no obvious enhancement of photocatalytic disinfection efficiency was obtained by the addition of Fe^{2+}, indicating that there was little H_2O_2 involved. Finally, isopropanol was utilized as a diagnostic tool for the detection of the free •OH in the solution. As can be seen from Fig. 5.6B, the addition of isopropanol could almost completely inhibit the photocatalytic disinfection of *E. coli* K 12, which indicates that the free •OH in the aqueous suspension plays an important role in this photocatalytic disinfection process.
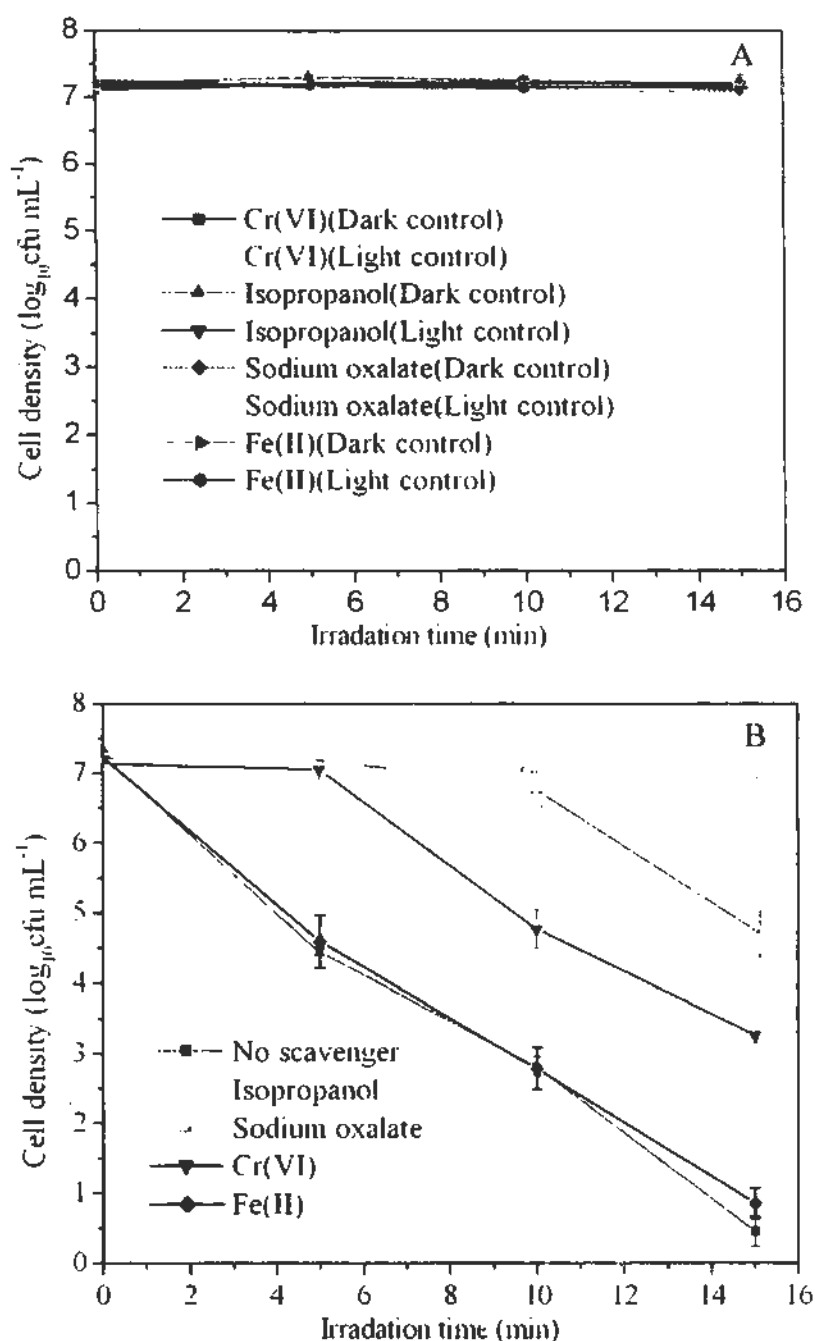
Fig. 5.6 The survivals of *E. coli* K 12 in presence of each scavenger under control experiments (A) and the photocatalytic inactivation of *E. coli* K 12 in presence of each scavenger with AgBr-Ag-Bi$_2$WO$_6$ nanojunction as photocatalyst under visible light (B). The density of *E. coli* K 12 is ~5×10^7 cfu mL^{-1}. The concentrations of the scavengers are 50 µM Cr(VI), 2 µM Fe(II)-EDTA, 0.3 M isopropanol and 30 µM sodium oxalate. Each data point and error bar represents the mean and the standard deviations of independent triplicates respectively.

5.3.2.2 The effect of direct contact

According to the above results, it is deduced that the adsorption of the bacterial cells by the photocatalyst is not so important for the disinfection efficiency. Thus, in the following study, the effect of adsorption time on the photocatalytic disinfection efficiency of *E. coli* K 12 using AgBr-Ag-Bi$_2$WO$_6$ nanojunction as photocatalyst has been investigated as shown in Fig. 5.7. As expected, with the adsorption time before the PCO process ranged from 0 to 60 min, there was no significant change for the subsequent photocatalytic disinfection efficiency.

To further confirm the role of the diffusing •OH, the photocatalytic disinfection of *E. coli* K 12 was also conducted using the modified partition setup (Fig. 5.1). Fig. 5.8 demonstrates the disinfection efficiency of *E. coli* K 12 inside a membrane packaged container when the outer system was under various conditions. As shown in Fig. 5.8, there were no obvious changes about the intensity of *E. coli* K 12 in the control experiments including negative control, dark control and light control, revealing that the saline solution, catalyst or visible light itself do not influence the survival of *E. coli* K 12 even after 1.5 h. However, there was about 6.5 log-reduction in viable cells count within 1.5 h when the outer system was visible-light irradiated AgBr-Ag-Bi$_2$WO$_6$ nanojunction suspension, indicating that the •OH generated outside diffused to inside of the container to disinfect the *E. coli* K 12. When the outer system was replaced by a Fenton reagent, ~5×10^7 cfu mL^{-1} of *E. coli* K 12 was quickly disinfected within 10 min, which further confirms that the bulky •OH can disinfect the bacteria in the container.
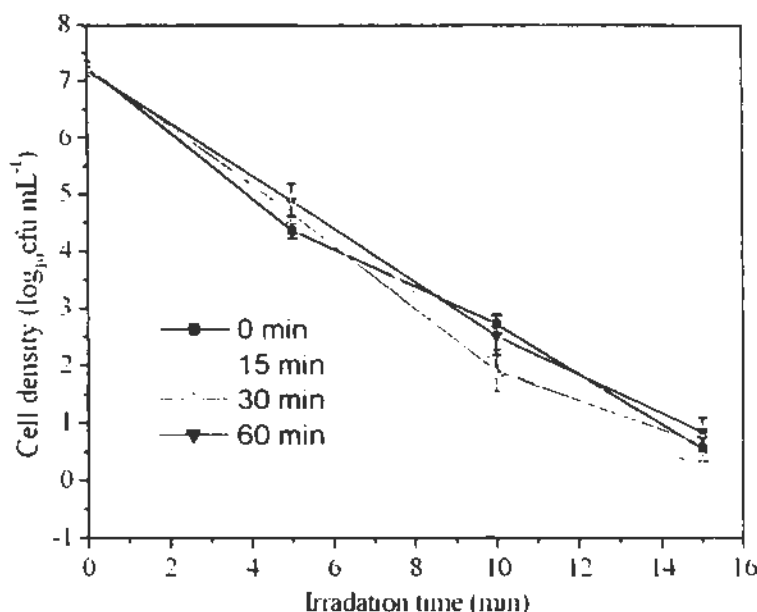
Fig. 5.7 The photocatalytic disinfection of *E. coli* K 12 ($\sim 5 \times 10^7$ cfu mL^{-1}, 50 mL) by 5 mg AgBr-Ag-Bi$_2$WO$_6$ nanojunction under visible light with different equilibrium time. Each data point and error bar represents the mean and the standard deviations of independent triplicates respectively.
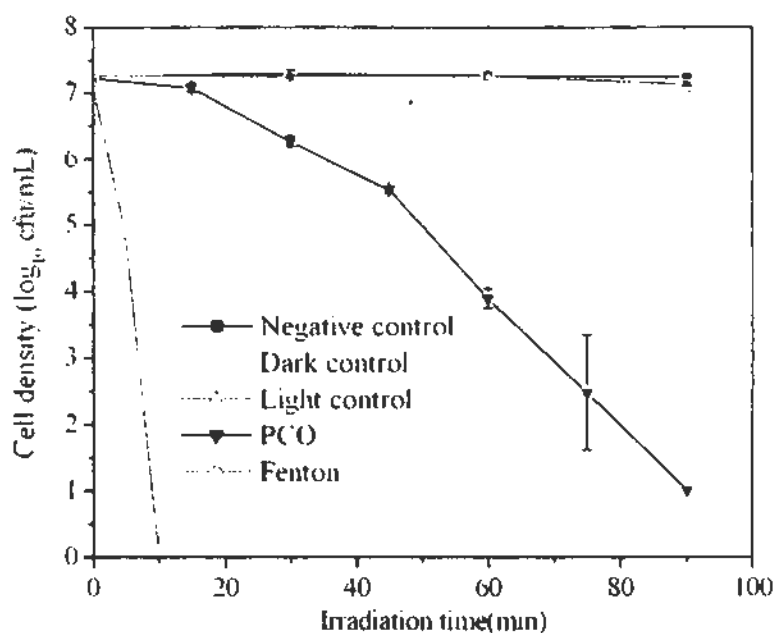
Fig 5.8 The photocatalytic disinfection of *E. coli* K 12 ($\sim 5 \times 10^7$ cfu mL^{-1}, 20 mL) inside a container when the outer system was in various conditions (PCO, Water + 5 mg AgBr-Ag-Bi$_2$WO$_6$ nanojunction + visible light irradiation; Fenton, Water + Fenton reagent (Zhang et al., 2006). Each data point and error bar represents the mean and the standard deviations of independent triplicates respectively.

5.3.2.3 The destruction mechanism of the bacteria

To understand the destruction process of bacteria by the diffusing •OH generated by VLD AgBr-Ag-Bi$_2$WO$_6$ nanojunction, the structure and morphology of E. coli K 12 at the different stages of PCO process were examined by TEM images as shown in Fig. 5.9. Before the PCO process, E. coli K 12 exhibited an intact cell structure with clear cell wall as well as the evenly rendered interiors (Fig. 5.9A). The dark black particles or spots appeared in these micrographs were AgBr-Ag-Bi$_2$WO$_6$ nanojunction clusters or particles. Only after 15-min photocatalytic treatment, an electron translucent region and the filament-like structure appeared at the central of the cells, but the cell wall structure was still intact (Fig. 5.9B). After 30-min irradiation, great changes had taken place to the morphology of E. coli K 12 (Fig. 5.9C). It was observed that the cell structure of some bacteria was distorted and the cell wall was ruptured. With the prolonged irradiation time (2h), the electron translucent regions were more significant and more cell structures were severely ruptured (Fig. 5.9D). When the PCO proceeded to 4h, the whole cell became completely translucent and only the layer of cell wall was existing (Fig. 5.9E). Eventually, there was only a small portion of cell debris (Fig. 5.9F) that we can observe, demonstrating the complete destruction of E. coli K 12.
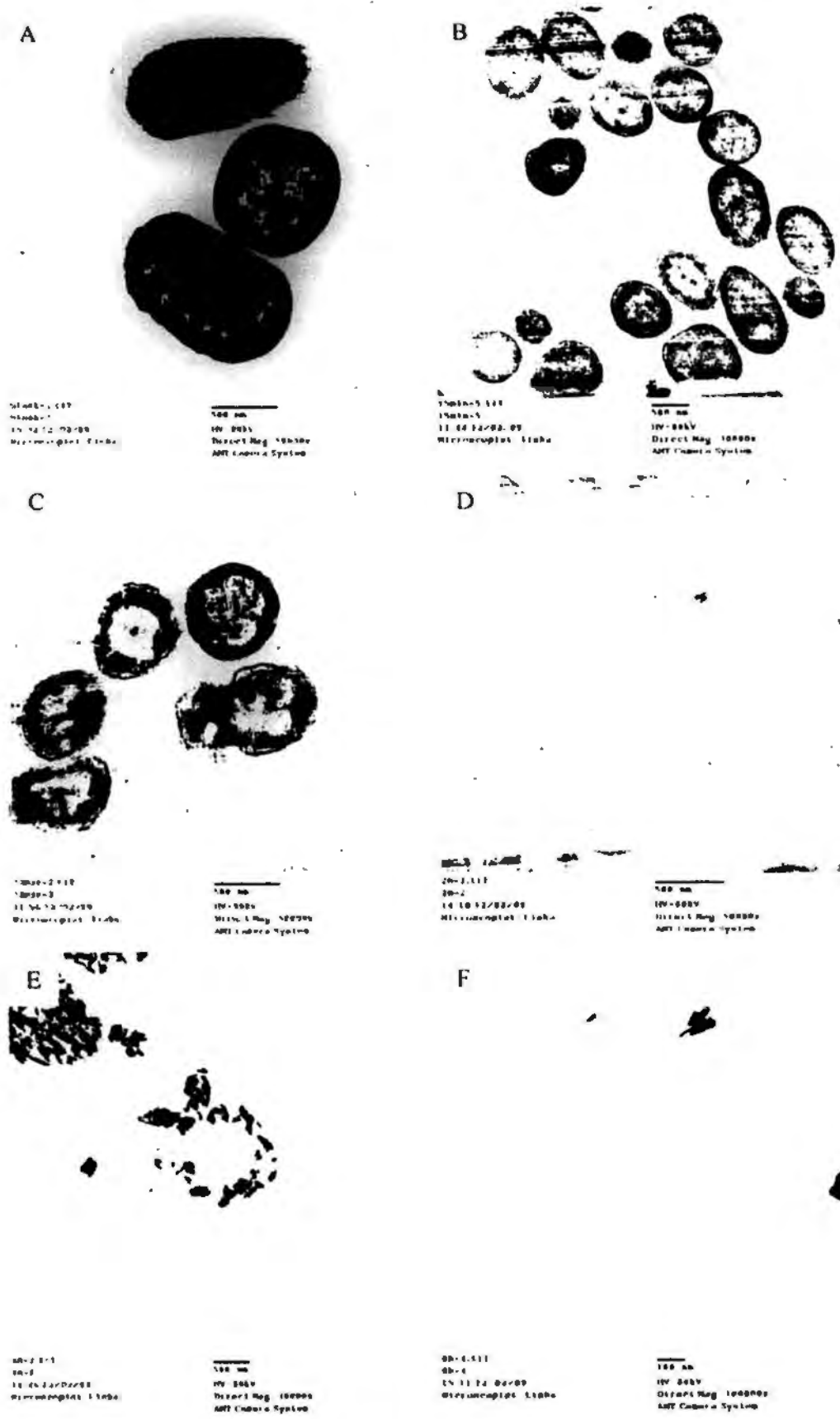
Fig.5.9 TEM images of *E. coli* K 12 photocatalytically untreated or treated with AgBr-Ag-Bi$_2$WO$_6$ nanojunction under visible light irradiation. Before irradiation (A), and after irradiated for 15 min (B), 30 min (C), 2h (D), 4 h (E) and 8 h (F).

In addition, the K^+ leakage of the bacteria along the PCO process was detected by AAS as shown in Fig. 5.10. Obviously, no significant leakage of K^+ occurred in the three sets of control experiments (Dark control, light control and negative control) (Fig. 5.10). In contrast, only after 15-min photocatalytic treatment, the concentration of the K^+ in the reaction mixture reached 790 μg L^{-1}, which shows that K^+ quickly leaked from the bacteria during the PCO process (Fig. 5.10).
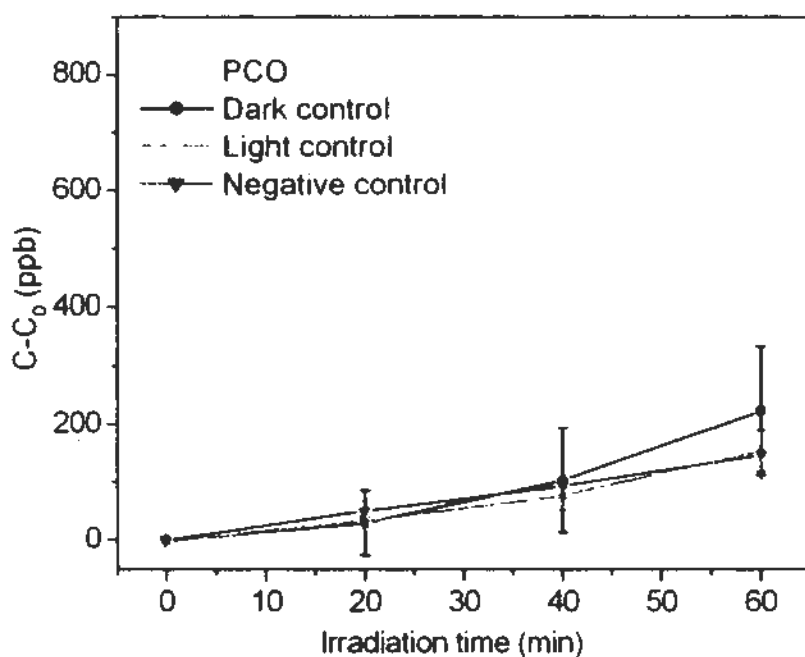
Fig. 5.10 K^+ leakage from *E. coli* K 12 under different conditions (PCO, AgBr-Ag-Bi$_2$WO$_6$ nanojunction with visible light irradiation; Dark control, only AgBr-Ag-Bi$_2$WO$_6$ nanojunction; Light control, only visible light irradiation; Negative control, no light and no catalyst). Each data point and error bar represents the mean and the standard deviations of independent triplicates respectively.

5.3.3 Disinfection of other bacteria

In the non-partition setup, other bacteria such as freshwater bacteria *E. coli* BW 25113 and *P. fluorescens* 85070, and a marine bacterium *A. macleodii* were used to examine the universality of disinfection of AgBr-Ag-Bi$_2$WO$_6$ nanojunction mediated photocatalysis as displayed in Fig. 5.11. The control experiments show that the saline (for freshwater bacteria) or 3% NaCl solution (for marine bacteria), visible-light irradiation and AgBr-Ag-Bi$_2$WO$_6$ nanojunction alone do not affect the survival of these three kinds of bacteria. Clearly, as shown in Fig. 5.11A, complete inactivation of *E. coli* BW 25113 (about 7.3-log) was obtained by the VLD AgBr-Ag-Bi$_2$WO$_6$ nanojunction within 10 min. And about 6.5-log photocatalytic inactivation of *P. fluorescens* 85070 was achieved within 30 min (Fig. 5.11B). Although the inactivation of the marine bacterium *A. macleodii* was relatively slower, about 5.1-log reduction of the cell density could be reached by this photocatalytic process (Fig. 5.11C).

In the partition setup, the inactivation of the freshwater bacterium, *P. fluorescens* 85070 and the marine bacterium, *A. macleodii* was further studied when the outer system was consisted by water, AgBr-Ag-Bi$_2$WO$_6$ nanojunction and visible light irradiation as shown in Fig.5.12. The control experiments also show that the NaCl solution, visible light and photocatalyst do not significantly affect the survival of these bacteria even after the prolonged time (90 min). Although these bacteria were separated from the photocatalyst of the AgBr-Ag-Bi$_2$WO$_6$ nanojunction, about 4.2-log inactivation of *P. fluorescens* 85070 and 6-log inactivation of *A. macleodii* were achieved after 90 min under visible light.
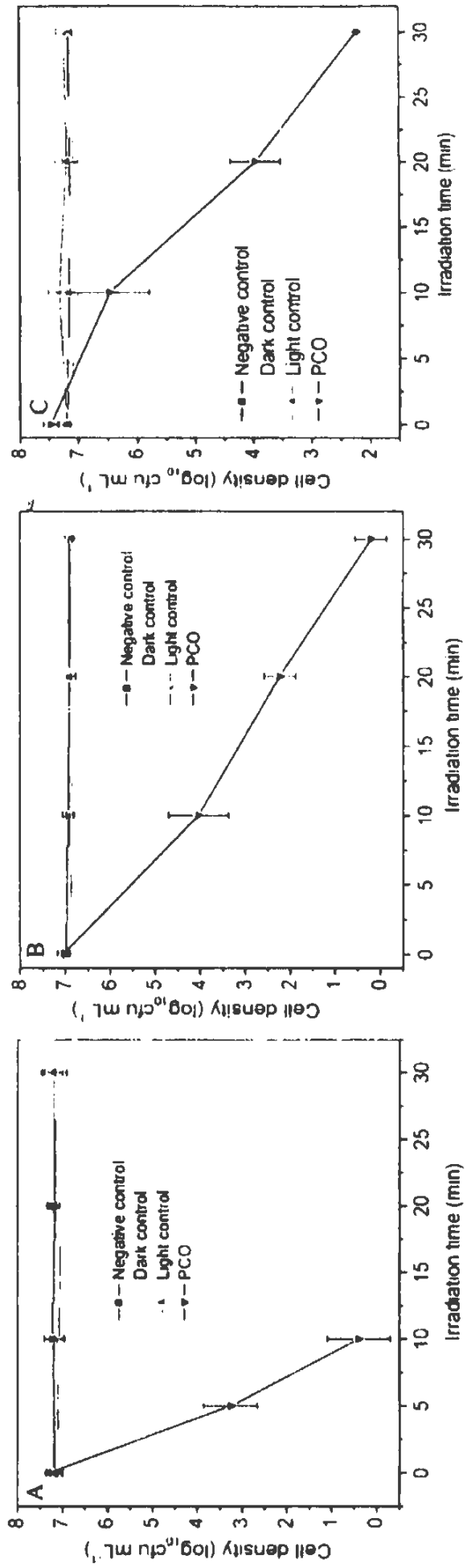
Fig. 5.11 Temporal course of other bacteria inactivation ($\sim 5 \times 10^7$ cfu mL^{-1}, 50 mL) in the non-partition setup with suspension containing 5 mg of AgBr-Ag-Bi$_2$WO$_6$ nanojunction under visible light irradiation. (A) *E. coli* BW 25113, (B) *P. fluorenscens* 85070, and (C) *A. macleodii*. Each data point and error bar represents the mean and the standard deviations of independent triplicates respectively.
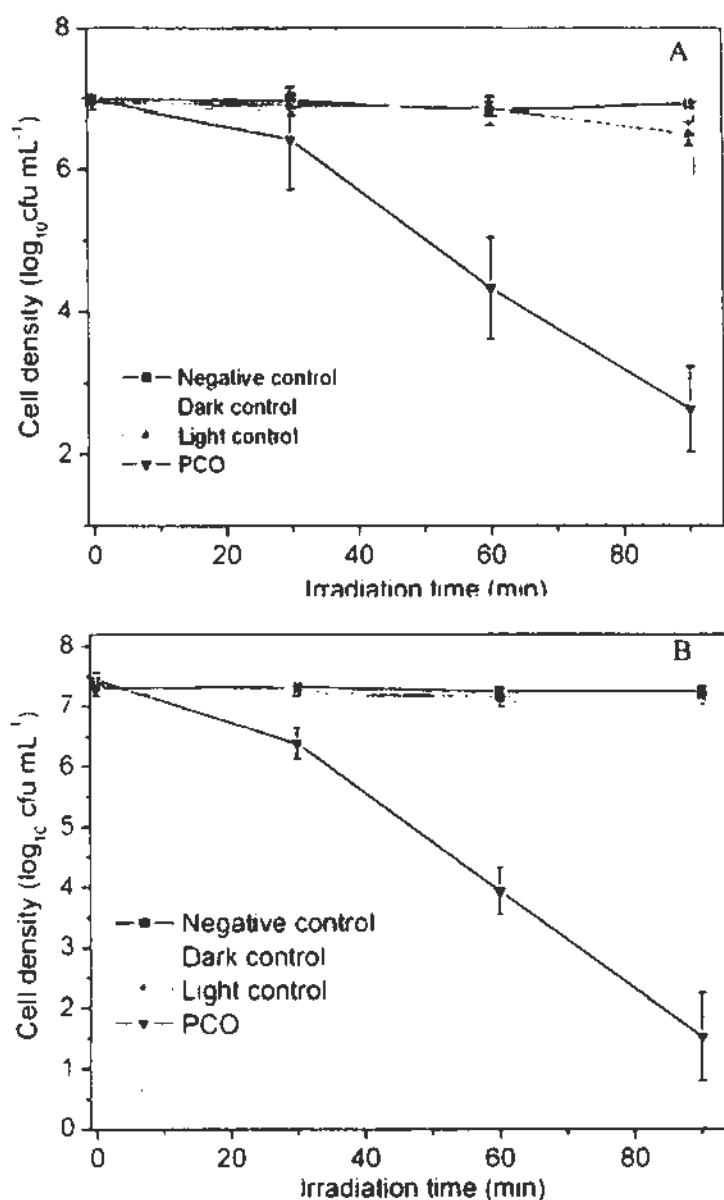
Fig. 5.12 Temporal course of other bacteria inactivation   (~5×10^7 cfu mL^{-1}, 20 mL) in the partition setup when outer system consisted by water, 5 mg of AgBr-Ag-Bi$_2$WO$_6$ nanojunction and visible light irradiation: (A), *P. fluorescens* 85070, and (B) *A. macleodii*. Each data point and error bar represents the mean and the standard deviations of independent triplicates respectively.

5.4 Discussion

5.4.1 Photocatalytic disinfection performances

As discussed in Chapter 3, AgBr-Ag-Bi$_2$WO$_6$ nanojunction exhibits higher photocatalytic activity than other photocatalysts containing single visible-light active component, such as Bi$_2$WO$_6$, Ag-Bi$_2$WO$_6$ and AgBr-Ag-TiO$_2$ composite, for the degradation of the azo dye, Procion Red MX-5B, and colorless pollutant, pentachlorophenol. There are two reasons for its excellent photocatalytic performance on the degradation of the organic pollutant. One is the broadened visible-light photo-response range of AgBr-Ag-Bi$_2$WO$_6$ nanojunction due to the presence of double visible-light active components (AgBr and Bi$_2$WO$_6$). The other reason may result from the synergic effect among the three components under the visible light irradiation, namely the vectorial electron transfer of Bi$_2$WO$_6$ → Ag → AgBr. For a photocatalyst, it was discovered that there is an apparent correlation between the two photocatalytic processes of organic pollutant degradation and microbial disinfection (Chen et al., 2009). Therefore, consistent with the degradation of organic pollutant as shown in Section 3.3.2, the AgBr-Ag-Bi$_2$WO$_6$ nanojunction also has the highest VLD photocatalytic inactivation activities, among the investigated photocatalysts including Bi$_2$WO$_6$ superstructure, Ag-Bi$_2$WO$_6$ and AgBr-Ag-TiO$_2$ composite (Fig.5.2B).

It is generally accepted that Ag$^+$ at high concentrations exhibits bactericidal activity (Pal et al., 2007). However, so little amount of Ag$^+$ in this case do not significantly affect the survival of *E. coli* K 12 even after 2h. These facts suggest that

the quick inactivation of *E. coli* K 12 (Fig. 5.2B) should result from the photocatalytic performance of AgBr-Ag-Bi$_2$WO$_6$ nanojunction instead of the eluted Ag$^+$.

For the fluorescence assays of photocatalytically untreated and treated *E. coli* K 12, SYTO 9 green-fluorescent nucleic acid stain generally labels the living bacteria with intact membrane, while propidium iodide penetrates only the bacterial cells with damaged membranes. When the mixture of both dyes was used, the penetration of propidium iodide can lead to a reduction of SYTO 9 stain fluorescence. Therefore, fluorescence assay employing the mixture of these two dyes is a reliable way to evaluate the disinfection of the bacteria. All of the bacteria were under living condition before the irradiation even in the presence of the AgBr-Ag-Bi$_2$WO$_6$ nanojunction (Fig. 5.4A), which again proves that no toxic effect is caused by the photocatalyst itself. However, after the reaction mixture containing with bacteria and AgBr-Ag-Bi$_2$WO$_6$ nanojunction irradiated under visible light, the population of living bacteria decrease swiftly, companying the quick increase of the population of killed bacteria (Figs. 5.4 B, 5.4C and 5.4D). Eventually, no living bacteria are observed after 10-min of photocatalytic treatment (Fig. 5.4E). Therefore, the AgBr-Ag-Bi$_2$WO$_6$ mediated VLD photocatalytic process do not merely inactivate the bacteria but effectively disinfect them.

5.4.2 Photocatalytic disinfection mechanism

5.4.2.1 The roles of ROSs in the photocatalytic disinfection process

Our previous study has indicates that AgBr-Ag-Bi$_2$WO$_6$ nanojunction has a Z-scheme structure, where a completely separated VB-hole (Bi$_2$WO$_6$) and CB-electron (AgBr) can be generated under VL irradiation (Zhang et al., 2009). Both the oxidation power of photogenerated VB-holes (Bi$_2$WO$_6$) (+2.68 V versus NHE) and the reduction power of photogenerated CB-electrons (AgBr) (-1.04 V versus NHE) are very strong. It is deduced that the photogenerated VB-holes can oxidize the OH$^-$/H$_2$O to produce •OH (E^0 (OH$^-$/•OH) =2.38 V versus NHE) (Li et al., 2007), while the photogenerated CB-electrons can reduce the surface chemisorbed O$_2$ to produce •O$_2^-$ (E^0 (O$_2$/•O$_2^-$)=-0.33 V versus NHE) (Li et al., 2007). To confirm this conjecture, the ESR spin-trap technique (with DMPO) was used to examine the generation of ROSs during the AgBr-Ag-Bi$_2$WO$_6$ nanojunction dispersion under visible light irradiation or in dark. No signals were detected in dark, while both •O$_2^-$ and •OH signals were obtained under the visible light irradiation (Fig 5.5). These facts confirm that •OH and •O$_2^-$ were produced in visible light irradiated suspension of AgBr-Ag-Bi$_2$WO$_6$ nanojunction, providing a solid indication that photogenerated VB-holes (Bi$_2$WO$_6$) and CB-electrons (AgBr) can retain long enough and react with adsorbed oxygen/H$_2$O to produce a series of ROSs which finally induce the decomposition of organic pollutants and/or microorganisms. However, only limited ROSs including •OH and •O$_2^-$ can be detected by this technique and there probably are other ROSs existing in the AgBr-Ag-Bi$_2$WO$_6$ nanojunction mediated photocatalytic disinfection process.

Besides •O$_2^-$ and •OH produced by VLD AgBr-Ag-Bi$_2$WO$_6$ nanojunction, H$_2$O$_2$ is

also potentially generated during this photocatalytic process for the disinfection of *E. coli* K 12 (Maness et al., 1999; Cho et al., 2005). To find out the exact kind(s) of these ROSs playing significant role(s) in the disinfection process, the photocatalytic disinfections of *E. coli* K 12 with addition of different scavengers were further investigated as shown in Fig. 5.6B. It should be first noted that the concentration of each of these scavengers is specified in the experimental conditions because under these as mentioned concentrations, these scavengers have no toxic effect on *E. coli* K 12 within 15 min as demonstrated in Fig. 5.6A. During the VLD photocatalytic disinfection process mediated by AgBr-Ag-Bi$_2$WO$_6$ nanojunction, the addition of sodium oxalate (a hole scavenger) and Cr(VI) (an electron scavenger) can partially inhibit the photocatalytic disinfection because both of •OH generated by the oxidative pathway and the ROSs such as •O$_2^-$, H$_2$O$_2$ and •OH generated by reductive pathway are probably involved in the disinfection of *E. coli* K 12. For the reductive pathway, •O$_2^-$ is produced at first via the reduction of the absorbed oxygen by photogenerated electron. But the produced •O$_2^-$ in water is very unstable, it would subsequently undergo facile disproportionation to produce other ROSs mainly including H$_2$O$_2$ and •OH (Ma et al., 2003). However, little H$_2$O$_2$ was detected involving in this photocatalytic disinfection process by the addition of Fe^{2+} in the reaction mixture. Therefore, during this AgBr-Ag-Bi$_2$WO$_6$ nanojunction mediated photocatalytic disinfection process, •OH generated by both of the oxidative pathway and reductive pathway is mainly responsible for the disinfection of *E. coli* K 12.

In order to clarify whether the disinfection of *E. coli* K 12 is caused by •OH

remaining bound to the surface or those diffusing into the solution bulk, isopropanol was employed as a diagnostic tool for the diffusing •OH because it is easily oxidized by •OH and has low affinity to semiconductor surfaces in aqueous media (Chen et al., 2005; Khodja et al., 2005). Interestingly, the addition of isopropanol could almost completely inhibit the photocatalytic disinfection of $E.\ coli$ K 12, which indicates that the free •OH the in the aqueous suspension other than the •OH absorbed on the photocatalyst plays an important role.

The previous study in Section 3.3.1 reveals that AgBr-Ag-Bi_2WO_6 nanojunction in neutral solution possesses negative charge, which is the same with surface charge of $E.\ coli$ K 12 (Hu et al., 2006). Thus, the electrostatic repulsion and the motility of bacteria result in that •OH remaining bound to the surface has little chance to disinfect the major portion of the bacteria. Therefore, the equilibrium adsorption time of $E.\ coli$ K 12 over AgBr-Ag-Bi_2WO_6 nanojunction before photocatalytic process has no significant effect on the photocatalytic disinfection efficiencies (Fig. 5.7).

Apart from the investigation on the effect of adsorption time, the modified partition setup as shown in Fig. 5.1 was utilized to further confirm the role of the diffusing •OH in the photocatalytic disinfection process. As shown in Fig. 5.1, a suspension of bacteria cells in saline was contained in the membrane packaged container and the photocatalyst particles dispersed in the saline outside of the container. Here, the semi-permeable membrane with the molecular weight cutoff (MWCO) of 12,000-14,000 Daltons also allows the free entry of smaller molecules such as water and bulky •OH, but prevents the passage of larger targets, such as the

AgBr-Ag-Bi$_2$WO$_6$ nanojunction with the diameter sizes of about 3 μm as shown in Fig. 3.1 and *E. coli* K 12 with molecular weight of about 2.6×10^6 Daltons. In this partition setup, the saline both inside and outside, the photocatalyst in the outer suspension and the light irradiation have no toxic effect on *E. coli* K 12 even after 1.5 h as demonstrated by the control experiments (Fig. 5.8). To our surprise, nearly complete disinfection has been achieved after 1.5 h when the outer system is visible-light irradiated AgBr-Ag-Bi$_2$WO$_6$ nanojunction. Since the visible-light irradiated AgBr-Ag-Bi$_2$WO$_6$ nanojunction and *E. coli* K 12 are separated by the semi-permeable membrane, only the diffusing reactive oxygen radicals, such as the diffusing •OH generated by VLD AgBr-Ag-Bi$_2$WO$_6$ nanojunction, can pass through the semi-permeable membrane to inactivate the bacterial cells inside of container. Fenton reagent is a well known kind of homogenous system to generate bulky •OH. When it is as outer system, complete disinfection of inside bacteria has been archived within 10 min, which further confirms that the bulky •OH can go through the membrane to inactivate the bacterial cells inside the container. Although the disinfection efficiency of *E. coli* K 12 by Fenton reagent was higher than that by the VLD AgBr-Ag-Bi$_2$WO$_6$ nanojunction, Fenton reagent would quickly lose its effect after the consumption of H$_2$O$_2$ (Zhang et al., 2006), while VLD AgBr-Ag-Bi$_2$WO$_6$ nanojunction is predicted to persist for long time due to its high stability confirmed by our previous study in Chapter 3.

The photocatalytic disinfection efficiency of *E. coli* K 12 in the partition system (Fig. 5.8) is lower than that in the non-separated system (Fig. 5.2B) because the

lifetime of •OH is short and some of them may annihilate during the diffusing process (Ishikawa, 2003). But of importance is that this fact directly proves that the direct contact between AgBr-Ag-Bi$_2$WO$_6$ nanojunction and bacterial cells is not a prerequisite for photocatalytic disinfection of microorganism.

5.4.2.2 The destruction mechanism of the bacteria

The TEM images clearly demonstrates that the photocatalytically untreated bacteria have a well-defined cell wall as well as the evenly rendered interior of the cell (Fig. 5.9A), which corresponds to the presence of proteins and DNA. Previous study indicates that that significant disorder in membrane permeability can be caused by the attack of photogenerated •OH (Cheng et al., 2007). During the photocatalytic process mediated VLD AgBr-Ag-Bi$_2$WO$_6$ nanojunction, the generation of an electron translucent region and the filament-like structure at the central of the cells (Fig. 5.9B) also results from the fact that the diffusing •OH attacks the outer membrane of the cell. Thus a leakage of the interior component such as K$^+$, a component virtually existing in bacteria and involving in the regulation of polysome content and protein synthesis occurs within 15 min (Fig. 5.10) during the PCO process. This leakage of the interiors directly results in the loss of cell viability (Saito et al., 1992; Ren et al., 2009) as shown in Figs. 5.2B and 5.4. Due to the powerful oxidative ability, the diffusing •OH can gradually degrade the other organic components of the cells, even the cell wall, which leads to the distortion of the bacteria shape (Figs. 5.9C and 5.9D). The rupture of the cell wall and the damage of

bacteria structure allow the entry of the outer solution containing large amount of diffusing •OH into the cells, facilitating the further degradation of the left intracellular components of the cells. Therefore, after 8 h of photocatalytic treatment, only a small portion of cell debris could be found (Fig. 5.9F), indicating the completely destruction of the *E. coli* K 12. Besides, these facts also confirm that the disinfection of *E. coli* K 12 results from the •OH generated during photocatalytic process instead of the Ag^+ eluted from catalyst and/or the Ag nanoshell in $AgBr-Ag-Bi_2WO_6$ nanojunction.

5.4.3 Photocatalytic disinfection of other bacteria

The $AgBr-Ag-Bi_2WO_6$ nanojunction mediated VLD photocatalysis can effectively inactivate different habited bacteria including freshwater bacteria *E. coli* BW 25113 and *P. fluorescens* 85070, and the marine bacterium *A. macleodii* (Fig.5.11). This fact reveals that the photocatalytic generated •OH can disinfect a variety of bacteria and has no selectivity. The photocatalytic inactivation efficiencies for these bacteria are a bit different, probably resulting from their different SOD activities and fatty acid profiles (Leung et al., 2008)

The two selected bacteria, freshwater bacterium *P. fluorescens* 85070, and marine bacterium *A. macleodii* also could be effectively inactivated in the partition setup when the outer system was $AgBr-Ag-Bi_2WO_6$ nanojunction mediated VLD photocatalysis (Fig.5.12), revealing that the •OH also can diffuse in to the container to inactivate kinds of bacteria.

5.5 Conclusions

In this work, we report an effective disinfection of bacteria including the freshwater bacteria such as *E. coli* K 12, *E. coli* BW 25113 and *P. fluorescens* 85070, and the marine bacterium *A. macleodii*, by using the $AgBr-Ag-Bi_2WO_6$ nanojunction as a photocatalyst under visible light irradiation. The VLD photocatalytic inactivation activity of $AgBr-Ag-Bi_2WO_6$ nanojunction is superior to other VLD photocatalysts such as Bi_2WO_6, $Ag-Bi_2WO_6$ and $AgBr-Ag-TiO_2$ composite. For the photochemical mechanism of bactericidal action, it has been found that the diffusing •OH generated both by the oxidative pathway and the reductive pathway play an important role in the $AgBr-Ag-Bi_2WO_6$ nanojunction mediated photocatalytic disinfection process. Moreover, a direct contact between $AgBr-Ag-Bi_2WO_6$ nanojunction and bacterial cells is directly proved to be unnecessary for the photocatalytic disinfection of bacteria by employing the partition setup. Finally, the photocatalytic destruction of the bacterial cells was observed by TEM images and further confirmed by the determination of K^+ leakage from the killed bacteria. Therefore, it is concluded that the $AgBr-Ag-Bi_2WO_6$ nanojunction has great potential for photocatalytic destruction of microorganisms.

6. General conclusions

Nowadays, the keen interests have been focused on the photocatalytic reactions occurring under solar illumination because of a tremendous set of environmental problems and energy crisis. Taking the sunlight into account, it is indispensable to develop highly effective visible-light-driven (VLD) photocatalysts. Up to date, many kinds of VLD photocatalysts such as doped TiO_2, complex oxides (Bi_2WO_6 and Calcium bismuthate ($CaBi_2O_4$)) and chalcogenides (Zinc sulfide (ZnS) and CdS) have been investigated. However, there are still some drawbacks hindering their practical application in the environmental protection. So it is still necessary to further develop highly effective VLD photocatalysts and to investigate the mechanism photocatalytic process.

In this work, I first report a new $AgBr-Ag-Bi_2WO_6$ nanojunction system by the facile deposition-precipitation method with Bi_2WO_6 superstructure as substrate, in which two visible-light active components ($AgBr$ and Bi_2WO_6) and the electron-transfer system (Ag) are spatially fixed. This $AgBr-Ag-Bi_2WO_6$ nanojunction exhibits an excellent photocatalytic activity for the degradation of an azo dye (Procion Red MX-5B) and pentachlorophenol, even for the disinfection of different kinds of bacteria including the freshwater bacteria - *E. coli* K 12, *E. coli* BW 25113 and *P. fluorescens* 85070, and the marine bacterium - *A. macleodii*. The physicochemical mechanism reveals that the excellent VLD photocatalytic performance of $AgBr-Ag-Bi_2WO_6$ nanojunction is derived from the broadened visible-light response and the synergic effect resulting from the vectorial electron

transfer of $Bi_2WO_6 \rightarrow Ag \rightarrow AgBr$ in visible-light excited $AgBr\text{-}Ag\text{-}Bi_2WO_6$ nanojunction.

In the Chapter 4, another kind of effective VLD photocatalyst, $Zn:In(OH)_yS_z$ solid solution nanoplates ($Zn:In(OH)_yS_z$-SSNs) were synthesized via the modified hydrothermal method. The band gap and redox potentials of conduction band and valence band can be efficiently controlled by adjusting the substitution of S^{2-} for OH^- and the doping of Zn^{2+} in $Zn:In(OH)_yS_z$ solid solution. Remarkably, $Zn:In(OH)_yS_z$-SSNs, which were prepared at $0.4 \leq X \leq 0.7$ (X represents the nominal atomic ratios between Zn^{2+} and In^{3+} in the synthesis solution), 45 mM thiourea and 26 mM SDS, have the highest photocatalytic activities, even exceeding 92% for the degradation of Rhodamine B (RhB) after 60 min under the irradiation of visible light.

$AgBr\text{-}Ag\text{-}Bi_2WO_6$ nanojunction is a kind of complex system including oxide, metal and halide, while the $Zn:In(OH)_yS_z$-SSNs are a kind of oxysulfide. These two photocatalysts have different properties and shows high performances in the photocatalytic degradation of different pollutants as discussed in Chapter 3 and Chapter 4. Thus my work reported some new ideas for the construction of effective VLD photocatalysts with novel structures and components, and these photocatalysts can be applied in the different situations in the environmental protection.

Moreover, a novel and simple partition setup was first constructed to assist the study of the fundamental mechanism of photocatalytic process. Two kinds of different mechanisms for photocatalytic processes were discovered in this study. (1) For $Zn:In(OH)_yS_z$ solid solution nanoplates mediated photocatalysis, the holes (h^+),

superoxide radical ($\cdot O_2^-$) and surficial hydroxyl radical ($\cdot OH_s$) existing on the surface of Zn:In(OH)$_y$S$_z$ solid solution nanoplates are the main reactive species for the photocatalytic degradation of RhB. Thus the direct contact between Zn:In(OH)$_y$S$_z$ solid solution nanoplates and RhB is a prerequisite for the degradation of RhB. (2) In contrast, for AgBr-Ag-Bi$_2$WO$_6$ nanojunction mediated photocatalysis, the bulky $\cdot OH$ plays important role for the disinfection of the bacteria, thus the direct contact between the AgBr-Ag-Bi$_2$WO$_6$ nanojunction and bacteria is unnecessary for the disinfection of bacteria.

Therefore, my work also provides some insight into the photocatalytic mechanism for enhancing the efficiency of photocatalytic oxidation process. Especially the findings: (a) The diffusing $\cdot OH$ plays important role in the disinfection process, and (b) no direct contact between the bacterial cells and photocatalyst was required, reveal the great potential application of the AgBr-Ag-Bi$_2$WO$_6$ nanojunction mediated PCO process in the destruction of biofilms that resist to disinfection because biofilms can provide shelter and substratum for microorganisms, store and trap nutrient, support microbial multiplication extracellularly.

7. References

Adams, C.D., Scanlan, P.A. and Secrist, N.S. 1994. Oxidation and biodegradability enhancement of 1, 4-dioxane using hydrogen peroxide and ozone. *Environmental Science & Technology* 28:1812–1818.

Alaton, I.A. 2003. A review of effects of dye-assisting chemicals on advanced oxidation of reactive dyes in wastewater. *Coloration Technology* 119:345–353.

Andreozzi, R., Caprio, V., Insola, A. and Marotta, R. 1999. Advanced oxidation processes (AOP) for water purification and recovery. *Catalysis Today* 53: 51–59.

Andrew, M.S. and Nie, S.M. 2010. Semiconductor nanocrystals: structure, properties, and band gap engineering. *Accounts of Chemical Research* 43:190–200.

Asahi, R., Morikawa, T., Ohwaki, T., Aoki, K. and Taga, Y. 2001. Visible-light photocatalysis in nitrogen-doped titanium oxides. *Science* 293:269–271.

Avivi, S., Mastai, Y. and Gedanken, A. 2000. Sonohydrolysis of In^{3+} ions: formation of needlelike particles of indium hydroxide. *Chemistry of Materials* 12:1229-1233.

Banat, I.M., Nigam, P., Singh, D. and Marchant, R. 1996. Microbial decolorization of textile-dye-containing effluents: A review. *Bioresource Technology* 58: 217–227.

Baux, N., Vannier, R.N., Mairesse, G. and Nowogrocki, G. 1996. Oxide ion conductivity in $Bi_2W_{(1-x)}ME_{(x)}O_{(6-x/2)}$ (ME=Nb,Ta). *Solid State Ionics* 91:243–248.

Belloni, J., Treguer, M., Remita, H. and Keyzer, R.D. 1999. Enhanced yield of photoinduced electrons in doped silver halide crystals. *Nature* 402: 865–867.

Bhatkhande, D.S., Pangarkar, V.G. and Beenackers, A.A. 2001. Photocatalytic degradation for environmental applications - A review. *Journal of Chemical Technology & Biotechnology* 77: 102–116.

Blake, D.M., Maness, P.C., Huang, Z., Wolfrum, E.J., Huang, J. and Jacoby, W.A. 1999. Application of the photocatalytic chemistry of titanium dioxide to disinfection and the killing of cancer cells. *Separation and Purification Methods* 28:1–50.

Centers for Disease Control and Prevention. 2005. *Preventing Bacterial Waterborne*

Diseases-Division of Bacterial Diseases. National Center for Immunization and Respiratory Diseases, Atlanta, USA.

Chen, F.N., Yang, X.D. and Wu, Q. 2009. Photocatalytic oxidation of *Escherischia coli*, *Aspergillus niger*, and formaldehyde under different ultraviolet irradiation conditions. *Environmental Science & Technology* 43:4606–4611.

Chen, F.N., Yang, X.D., Xu, F.F., Wu, Q. and Zhang, Y.P. 2009. Correlation of photocatalytic bactericidal effect and organic matter degradation of TiO_2 part I: Observation of phenomena. *Environmental Science & Technology* 43: 1180–1184.

Chen, X.B. and Mao, S.S. 2007. Titanium dioxide nanomaterials: Synthesis, properties, modifications, and applications. *Chemical Reviews* 107: 2891–2959.

Chen, Y.X., Yang, S.Y., Wang, K. and Lou, L.P. 2005. Role of primary active species and TiO_2 surface characteristic in UV-illuminated photodegradation of Acid Orange 7. *Journal of Photochemistry and Photobiology A: Chemistry* 172:47–54.

Cheng, Y.W., Chan, C.Y. and Wong, P.K. 2007. Disinfection of *Legionella pneumophila* by photocatalytic oxidation. *Water Research* 41:842–852.

Chhabra, V., Pillai, V., Mishra, B.K., Morrone, A. and Shah, D.O. 1995. Synthesis, characterization, and properties of microemulsion-mediated nanophase TiO_2 particles. *Langmuir* 11:3307–3311.

Chlorine Chemistry Division of the American Chemistry Council. 2003. *Drinking Water Chlorination: A Review of Disinfection Practices and Issues*. American Chemistry Council, Inc., Arlington, USA.

Choi, W., Kim, S., Cho, S., Yoo, H. and Kim, M.H. 2001. Photocatalytic reactivity and diffusing •OH radicals in the reaction medium containing TiO_2 particles. *Korean Journal of Chemical Engineering* 18: 898–902.

Cho, M., Chung, H., Choi, W.Y. and Yoon, J.Y. 2005. Different inactivation behaviors of MS-2 phage and *Escherichia coli* in TiO_2 photocatalytic disinfection. *Applied and Environmental Microbiology* 71:270–275.

Chung, C.J., Lin, H.I., Tsou, H.K., Shi, Z.Y. and He, J.L. 2008. An antimicrobial TiO_2 coating for reducing hospital-acquired infection. *Journal of Biomedical Materials Research Part B: Applied Biomaterials* 85B: 220–224.

Elahifard, M.R., Rahimnejad, S., Haghighi, S. and Gholami, M.R. 2007. Apatite-coated Ag/AgBr/TiO$_2$ visible-light photocatalyst for destruction of bacteria. *Journal of the American Chemical Society* 129: 9552-9553.

Erkan, A., Bakir, U. and Karakas, G. 2006. Photocatalytic microbial inactivation over Pd doped SnO$_2$ and TiO$_2$ thin films. *Journal of Photochemistry and Photobiology A: Chemistry* 184:313–321.

Esplugas, S., Giménez, J., Contreras, S., Pascual, E. and Rodríguez, M. 2002. Comparison of different advanced oxidation processes for phenol degradation. *Water Research* 36:1034–1042.

Finlayson, A.P., Tsaneval, V.N., Lyons L., Clark, M. and Glowacki, B.A. 2006. Evaluation of Bi–W-oxides for visible light photocatalysis. *Physica Status Solidi (a)* 203:327–335.

Fox, M.A. and Dulay, M.T. 1993. Heterogeneous photocatalysis, *Chemical Reviews* 93:341–357.

Frank, S.N. and Bard, A.J. 1977. Heterogeneous photocatalytic oxidation of cyanide and sulfite in aqueous solutions at semiconductor powders. *The Journal of Physical Chemistry* 81:1484–1488.

Fu, H.B., Pan, C.S., Yao W.Q. and Zhu, Y.F. 2005. Visible-light-induced degradation of Rhodamine B by nanosized Bi$_2$WO$_6$. *The Journal of Physical Chemistry B* 109:22432–22439.

Fujishima, A. and Honda, K. 1972. Electrochemical photolysis of water at a semiconductor electrode. *Nature* 238:37–38.

Fujishima, A., Rao, T.N. and Tryk, D.A. 2000. Titanium dioxide photocatalysis *Journal of Photochemistry and Photobiology C: Photochemistry Reviews* 1:1–21.

Gao, F., Chen, X.Y., Yin, K.B., Dong, S., Ren, Z.F., Yuan, F., Yu, T., Zou, Z.G. and Liu. J.M. 2007. Visible-light photocatalytic properties of weak magnetic BiFeO$_3$ nanoparticles. *Advanced Materials* 19:2889–2892.

Gopal, K., Tripathy, S.S., Bersillon, J.L. and Dubey, S.P. 2007. Chlorination byproducts, their toxicodynamics and removal from drinking water. *Journal of Hazardous Materials* 140:1–6.

Gopidas, K.R., Bohorquez, M. and Kamat, P.V. 1990. Photoelectrochemistry in semiconductor particles systems. 16. Photophysical and photochemical aspects

of coupled semiconductors-charge transfer processed in colloidal CdS-TiO$_2$ and CdS-AgI systems. *Journal of Physical Chemistry* 94: 6435–6440.

Hagfeldtt, A. and Grätzel, M. 1995. Light-induced redox reactions in nanocrystalline systems. *Chemical Reviews 95:* 49–68.

Hirakawa, T. and Kamat, P.V. 2005. Charge separation and catalytic activity of Ag/TiO$_2$ core-shell composite clusters under UV-irradiation. *Journal of American Chemical Society* 127: 3928–3934.

Hoffmann, M.R., Martin, S.T.; Choi, W. and Bahneman, D.W. 1995. Environmental applications of semiconductor photocatalysis. *Chemical Reviews* 95: 69–96.

Hoigéne, J. and Bader, H. 1983. Rate constants of reaction of ozone with organic and inorganic compounds in water. Part I. Non-dissociating organic compounds. *Water Research* 17:173–83.

Hu, C., Yu, J.C., Hao, Z.P. and Wong, P.K. 2003. Photocatalytic degradation of triazine-containing azo dyes in aqueous TiO$_2$ suspensions. *Applied Catalysis B: Environmental* 42:47–55.

Hu, C., Lan, Y.Q., Qu, J.H., Hu, X.X. and Wang, A.M. 2006. Ag/AgBr/TiO$_2$ visible light photocatalyst for destruction of azodyes and bacteria. *The Journal of Physical Chemistry B* 110:4066–4072.

Hu, C., Hu, X.X., Guo, J. and Qu, J.H. 2006. Efficient destruction of pathogenic bacteria with NiO/SrBi$_2$O$_4$ under visible light irradiation. *Environmental Science & Technology* 40:5508–5513.

Hu, X.L., Li, G.S. and Yu J.C. 2010. Design, fabrication, and modification of nanostructured semiconductor materials for environmental and energy applications. *Langmuir* 26:3031–3039.

Hua, G.H. and Reckhow, D.A. 2007. Comparison of disinfection byproduct formation from chlorine and alternative disinfectants. *Water Research* 41:1667–1678.

Inoue, T., Fujishima, A., Konishi, S. and Honda, K. 1979. Photoelectrocatalytic reduction of carbon dioxide in aqueous suspesions of semiconductor powders. *Nature* 277: 637–638.

Ireland, J.C., Dávila, B., Moreno, H., Fink, S.K. and Tassos, S. 1995. Heterogeneous photocatalytic decomposition of polyaromatic hydrocarbons over titanium dioxide. *Chemosphere* 30: 965-984.

Ishikawa, Y., Matsumoto, Y., Nishida, Y., Taniguchi, S. and Watanabe, J. 2003. Surface treatment of silicon carbide using TiO_2(IV) photocatalyst. *Journal of the American Chemical Society* 125:6558-6562.

Jin, R.C., Gao, W.L., Chen, J.X., Zeng, H.S., Zhang, F.X., Liu, Z.G. and Guan, N.J. 2004. Photocatalytic reduction of nitrate ion in drinking water by using metal-loaded $MgTiO_3$-TiO_2 composite semiconductor catalyst. *Journal of Photochemistry and Photobiology A-Chemistry* 162:585–590.

Jorens, P.G. and Schepens, P.J.C. 1993. Human pentachlorophenol poisoning. *Human & Experimental Toxicology* 12:479–495.

Kabra, K., Chaudhary, R. and Sawhney R.L. 2004. Treatment of hazardous organic and inorganic compounds through aqueous-phase photocatalysis: A review. *Industrial & Engineering Chemistry Research* 43:7683–7696.

Kale, B.B., Baeg, J.O., Lee, S.M., Chang, H.J., Moon, S.J. and Lee, C.W. 2006. $CdIn_2S_4$ nanotubes and "marigold" nanostructures: A visible-like photocatalyst. *Advanced Functional Materials* 16:1349-1354.

Kamat, P.V. and Fox, M.A. 1983. Photosensitization of TiO_2 colloids by Erythrosin B in acetonitrile. *Chemical Physics Letters* 102: 379–384.

Kamat, P.V. 1993. Photochemistry on nonreactive and reactive (semiconductor) surfaces. *Chemical Reviews* 93: 207–300.

Kamat, P.V. and Meisel, D. 1997. *Semiconductor Nanoclusters-Physical, Chemical, and Catalytic Aspects.* Elsevier press, The New York, USA.

Khodja, A.A., Boulkamh, A. and Richard, C. 2005. Phototransformation of metobromuron in the presence of TiO_2. *Applied Catalysis B: Environmental* 59:147–154.

Kim, H.G., Borse, P.H., Choi, W. and Lee, J.S. 2005. Photocatalytic nanodiodes for visible-light photocatalysis. *Angewandte Chemie International Edition* 44: 4585–4589.

Kim, H.G., Hwang, D.W. and Lee, J.S. 2004. An undoped, single-phase oxide photocatalyst working under visible light. *Journal of the American Chemical Society* 126:8912–8913.

Kim, N., Vannier, R.N. and Grey, C.P. 2005. Detecting different oxygen-ion jump pathways in Bi_2WO_6 with 1-and 2-dimensional O-17 MAS NMR spectroscopy *Chemical of Materials* 17:1952–1958.

Kohno, M., Kaneko, T., Ogura, S., Sato, K. and Inoue, Y. 1998. Dispersion of ruthenium oxide on barium titanates ($Ba_6Ti_{17}O_{40}$, $Ba_4Ti_{13}O_{30}$, $BaTi_4O_9$ and $Ba_2Ti_9O_{20}$) and photocatalytic activity for water decomposition. *Journal of the Chemical Society-Faraday Transactions* 94: 89-94.

Kudo, A., Sayama, K., Tanaka, A., Asakura, K., Domen, K., Maruya, K. and Onishi T. 1989. Nickel-loaded $K_4Nb_6O_{17}$ photocatalyst in the decomposition of H_2O into H_2 and O_2: Structure and reaction mechanism. *Journal of Catalysis* 120: 337-352.

Kudo, A. and Hijii, S. 1999. H_2 or O_2 evolution from aqueous solutions on layered oxide photocatalysts consisting of Bi^{3+} with 6s(2) configuration and d(0) transition metal ions. *Chemistry Letters* 1103-1104.

Kudo, A., Omori, K. and Kato, H. 1999. A novel aqueous process for preparation of crystal form-controlled and highly crystalline $BiVO_4$ powder from layered vanadates at room temperature and its photocatalytic and photophysical properties. *Journal of the American Chemical Society* 121:11459-11467.

Kudo, A. 2007. Recent progress in the development of visible-light-driven powdered photocatalysts for water splitting. *International Journal of Hydrogen Energy* 32: 2673-2678.

Kuo, C.H. and Huang, M.H. 2008. Facile synthesis of Cu_2O nanocrystals with systematic shape evolution from cubic to octahedral structures. *The Journal of Physical Chemistry C* 112: 18355-18360.

Kühn, K.P., Chaberny, I.F., Massholder, K., Stickler, M., Benz, V.W., Sonntag, H.G. and Erdinger, L. 2003. Disinfection of surfaces by photocatalytic oxidation with titanium dioxide and UVA light. *Chemosphere* 53:71-77.

Lei, Z.B., Ma, G., Liu, M., You, W., Yan, H., Wu, G., Takata, T., Hara, M., Domen, K. and Li, C. 2006. Sulfur-substituted and zinc-doped $In(OH)_3$: A new class of catalyst for photocatalytic H_2 production from water under visible light illumination. *Journal of Catalysis* 237:322-329.

Leung, T.Y., Chan, C.Y., Hu, C., Yu, J.C. and Wong, P.K. 2008. Photocatalytic disinfection of marine bacteria using fluorescent light. *Water Research* 42: 4827-4837.

Li, F.B., Li, X.Z. and Hou, M.F. 2004. Photocatalytic degradation of 2-mercaptobenzothiazole in aqueous La^{3+}-TiO_2 suspension for odor control. *Applied Catalysis B: Environmental* 48:185-194.

Li, G.T., Wong, K.H., Zhang, X.W., Hu, C., Yu, J.C., Chan, C.Y. and Wong, P.K. 2009. Degradation of Acid Orange 7 using magnetic AgBr under visible light: The roles of oxidizing species. *Chemosphere* 76: 1185–1191.

Li, Q., Li, Y.W., Wu, P.G., Xie, R.C. and Shang, J.K. 2008. Palladium oxide nanoparticles on nitrogen-doped titanium oxide: accelerated photocatalytic disinfection and post-illumination catalytic "memory". *Advanced Materials* 20: 3717–3723.

Li, Z.H., Dong, T.T., Zhang, Y.F., Wu, L., Wang, J.Q., Wang, X.X. and Fu, X.Z. 2007. Studies on $In(OH)_yS_z$ solid solutions: Syntheses, characterizations, electronic structure, and visible-light-driven photocatalytic activities. *The Journal of Physical Chemistry C* 111:4727–4733.

Liu, S.X., Qu, Z.P., Han, X.W. and Sun, C.L. 2004. A mechanism for enhanced photocatalytic activity of silver-loaded titanium dioxide. *Catalysis Today* 93: 877–884.

Liu, Y., Chen, X., Li, J. and Burda, C. 2005. Photocatalytic degradation of azo dyes by nitrogen-doped TiO_2 nanocatalysts. *Chemosphere* 61:11–18.

Liu, Z.F., Zhao, Z.G. and Miyauchi, M. 2007. Efficient visible light active $CaFe_2O_4/WO_3$ based composite photocatalysts: Effect of interfacial modification. *The Journal of Physical Chemistry C* 113:17132–17137.

Ma, W., Huang, Y., Li, J., Chen, M., Song, W. and Zhao, J. 2003. An efficient approach for the photodegradation of organic pollutants by immobilized iron ions at neutral pHs. *Chemical Communications* 1582–1583.

Machado, A.E.H., Furuyama, A.M., Falone, S.Z., Ruggiero, R., Perez, D.D. and Castellan, A. 2000. Photocatalytic degradation of lignin and lignin models, using titanium dioxide: the role of the hydroxyl radical. *Chemosphere* 40:115-124.

Maness, P.C., Smolinski, S., Blake, D.M., Huang, Z., Wolfrum, E.J. and Jacoby, W.A. 1999. Bactericidal activity of photocatalytic TiO_2 reaction: Toward an understanding of its killing mechanism. *Applied and Environmental Microbiology* 65:4094–4098.

Matsunaga, T., Tomada, R., Nakajima, T. and Wake, H. 1985. Photoelectrochemical sterilization of microbial cells by semiconductor powders. *FEMS Microbiology Letters* 29:211–214.

Moulder, J.F., Stickle, W.F., Sobol, P.E. and Bomben, K.D. 1992. *Handbook of X-ray Photoelectron Spectroscopy*, Perkin Elmer Corporation Physical Electronics Division, Waltham, USA.

Nasr, C., Vinodgopal, K., Fisher, L., Hotchandani, S., Chattopadhyay, A.K. and Kamat, P.V. 1996. Environmental photochemistry on semiconductor surfaces. Visible light induced degradation of a textile diazo dye, naphthol blue black, on TiO_2 nanoparticles. *The Journal of Physical Chemistry* 100: 8436-8442.

Ollis, D. 1993. Comparative aspects of advanced oxidation processes. In: *Emerging Technologies in Waste Management II, ACS Symposium Series 518*. Washington, USA.

Ollis, D.F., Pelizzetti, E. and Serpone, N. 1989. *Photocatalysis: Fundamentals and applications*. Wiley Press, New York, USA.

O'Regan, B. and Grätzel, M. 1991. A low-cost, high-efficiency solar cell based on dye sensitized colloidal TiO_2 films. *Nature* 353: 737-739.

Pal, S., Tak, Y.K. and Song, J.M. 2007. Does the antibacterial activity of silver nanoparticles depend on the shape of the nanoparticle? A study of the Gram-negative bacterium *Escherichia coli. Applied and Environmental Microbiology* 73:1712-1720.

Pandey, A., Singh, P. and Iyengar, L. 2007. Bacterial decolourization and degradation of azo dyes. *International Biodeterioration and Biodegradation* 59: 73-84.

Pang, K.M., Ng, S., Chung, W.K. and Wong, P.K. 2007. Removal of pentachlorophenol by adsorption on magnetite-immobilized chitin. *Water, Air and Soil Pollution* 183:355-365.

Parson, S. 2004. *Advanced Oxidation Process for Water and Wastewater Treatment*. CRC Press, London, UK.

Pignatello, J.J. 1992. Dark and photoassisted Fe^{3+}-catalyzed degradation of chlorophenoxy herbicides by hydrogen peroxide. *Environmental Science & Technology* 26: 944-951.

Pinheiro, H.M., Touraud, E. and Thomas, O. 2004. Aromatic amines from azo dye reduction: status review with emphasis on direct UV spectrophotometic detection in textile industry wastewaters. *Dye and Pigment* 61: 121-139.

Platzek, T., Lang, C., Grohmann, G., Gi, U.S. and Baltes, W. 1999. Formation of a carcinogenic aromatic amine from an azo dye by human skin bacteria *in vitro*.

Human and Experimental Toxicology 18: 552-559.

Pradhan, D. and Leung, K.T. 2008. Controlled growth of two-dimensional and one-dimensional ZnO nanostructures on indium tin oxide coated glass by direct electrodeposition. *Langmuir* 24:9707-9716.

Prairie, M.R., Evans, L.R., Stange, B.M. and Martinez, S.L. 1993. An investigation of TiO_2 photocatalysis for the treatment of water contaminated with metals and organic chemicals. *Environmental Science & Technology* 27:1776-1782.

Prousek, J. 1996. Advanced oxidation processes for water treatment. Photochemical processes. *Chemicke Listy* 90: 307–315.

Rawat, S.S. and Chattopadhyay, A. 1999. Structural transition in the micellar assembly: A fluorescence study. *Journal of Fluorescence* 9:233-244.

Ray, R.S., Singh, S.K., Hans R.K. and Joshi, P.C. 2002. Identification of new photoreduction products of pentachlorophenol. *Journal of Environmental Monitoring* 4:449–451.

Ren, C., Wang, W.Z., Zhang, L., Chang, J. and Sheng, H. 2009. Photocatalytic inactivation of bacteria by photocatalyst Bi_2WO_6 under visible light. *Catalysis Communications* 10:1940–1943.

Safarzadeh-Amiri, A., Bolten, J.R. and Cater, S.R. 1996. The use of iron in advance oxidation processes. *Journal of Advanced Oxidation Technologies* 1:18–26.

Saritha, P., Aparna, C., Himabindu, V. and Anjaneyulu. Y. 2007. Comparison of various advanced oxidation processes for the degradation of 4-chloro-2 nitrophenol. *Journal of Hazardous Materials* 149: 609–614.

Sato, S. 1986. Photocatalytic activity of NO_x-doped TiO_2 in the visible-light region. *Chemical Physics Letters* 123:126-128.

Saito, T., Iwase, T., Horie, J. and Morioka, T. 1992. Mode of photocatalytic bactericidal action of powdered semiconductor TiO_2 on mutans *streptococci*. *Journal of Photochemistry and Photobiology B: Biology* 14:369–379.

Sciacca, S. and Conti, G.O. 2009. Mutagens and carcinogens in drinking water. *Mediterranean Journal of Nutrition and Metabolism* 2:157-162.

Serpone, N., Terzian, R., Minero, C. and Pelizzetti, E. 1993. Heterogeneous photocatalyzed oxidation of phenol, cresols, and fluorophenols in aqueous suspensions. *Photosensitive Metal-Organic Systems: Mechanistic Principles and Applications*. American Chemical Society Press, New York, USA.

Shannon, M.A., Bohn, P.W., Elimelech, M., Georgiadis, J.G. Mariñas, B.J. and Mayes, A.M. 2008. Science and technology for water purification in the coming decades. *Nature* 452:301–310.

Siegel, R.W., Hu, E. and Roco, M.C. 1999. *Nanostructure Science and Technology: A Worldwide Study*, WTEC, Loyola College, Baltimore, Maryland, USA.

So, C.M., Cheng, M.Y., Yu, J.C. and Wong, P.K. 2002. Degradation of azo dye Procion Red MX-5B by photocatalytic oxidation. *Chemosphere* 46: 905–912.

Subramanian, V., Wolf, E.E. and Kamat. P.V. 2004. Catalysis with TiO_2/gold nanocomposites. Effect of metal particle size on the Fermi level equilibration. *Journal of American Chemical Society* 126:4943-4950.

Sunada, K., Kikuchi, Y., Hashimoto, K. and Fujishima, A. 1998. Bactericidal and detoxification effects of TiO_2 thin film photocatalysts. *Environmental science & Technology* 32: 726-728.

Stolz, A. 2001. Basic and applied aspects in the microbial degradation of azo dyes. *Applied Microbiology and Biotechnology* 56: 69-80.

Tada, H., Mitsui, T., Kiyonaga, T., Akita, T. and Tanaka, K. 2006. All-solid-state Z-scheme in $CdS-Au-TiO_2$ three-component nanojunction system. *Nature Materials* 10:782-786.

Tanaka, K., Padermpole, K. and Hisanaga, T. 2000. Photocatalytic degradation of commercial azo dyes. *Water Research* 34:327–333.

Tang, J.W., Zou, Z.G. and Ye J.H. 2004. Efficient photocatalytic decomposition of organic contaminants over $CaBi_2O_4$ under visible-light irradiation. *Angewandte Chemie International Edition* 43:4463–4466.

Tang, J.W., Zou, Z.G. and Ye J.H. 2004. Photocatalytic decomposition of organic contaminants by Bi_2WO_6 under visible light irradiation. *Catalysis Letters* 92:53-56.

Tierno, P. and Goedel, W.A. 2006. Using electroless deposition for the preparation of micron sized polymer/metal core/shell particles and hollow metal spheres. *The Journal of Physical Chemistry B* 110:3043-3050.

Titus, M.P., Molina, V.G., Baños, M.A., Giménez, J. and Esplugas, S. 2004. Degradation of chlorophenols by means of advanced oxidation processes: a general review. *Applied Catalysis B: Environmental* 47: 219–256.

Umbuzeiro, G.D.A., Freeman, H.S., Warren, S.H., de Oliveira, D.P., Terao, Y., Watanabe, T. and Claxton, L.D. 2005. The contribution of azo dyes to the mutagenic activity of the Cristais River. *Chemosphere* 60: 55-64.

United Stated Environmental Protection Agency, 2006. *Consumer Factsheet on: Pentachlorophenol*. United Stated Environmental Protection Agency. Washington, D.C., USA.

Usui, H. 2007. Influence of surfactant micelles on morphology and photoluminescence of zinc oxide nanorods prepared by one-step chemical synthesis in aqueous solution. *The Journal of Physical Chemistry C* 111: 9060-9065

Vinodgopal, K., Wynkoop, D.E. and Kamat, P.V. 1996. Environmental photochemistry on semiconductor surfaces: Photosensitized degradation of a textile azo dye, acid orange 7, on TiO_2 particles using visible light. *Environmental Science & Technology* 30:1660-1666.

Vlachopoulos, N., Liska, P., Augustynski, J. and Grätzel, M. 1988. Very efficient visible-light energy harvesting and conversion bu spectral sensitization of high surface-area polycrystalline titanium-dioxide films. *Journal of the American Chemical Society* 110: 1216-1220.

Wagner, C. and Muilenberg, G. 1979. *Handbook of X-ray photoelectron spectroscopy*. Physical Electronics Division; Perkin-Elmer Corp., Eden Prairie, USA.

Wang, W.Z., Zhu, W. and Xu H.L. 2008. Monodisperse, mesoporous $Zn_xCd_{1-x}S$ nanoparticles as stable visible-light-driven photocatalysts. *The Journal of Physical Chemistry C* 112: 16754–16758.

Wang, X.C., Yu, J.C., Ho, C.M., Hou, Y.D. and Fu, X.Z. 2005. Photocatalytic activity of a hierarchically macro/mesoporous titania. *Langmuir* 21:2552–2559.

World Health Organization. 2004. *The Environment: Where's the Risk, and Where are Children Safe?* World Health Organization, Geneva, Switzerland.

Wolfe, R.L. 1990. Ultraviolet disinfection of potable water-current technology and research and research needs. *Environmental Science & Technology* 24: 768-772.

Wu, J., Duan, F., Zheng, Y. and Xie, Y. 2007. Synthesis of Bi_2WO_6 nanoplate-built hierarchical nest-like structures with visible-light-induced photocatalytic activity. *The Journal of Physical Chemistry C* 111:12866–12871.

Yan, X.L., Ohno, T., Nishijima, K., Abe, R. and Ohtani, B. 2006. Is methylene blue an appropriate substrate for a photocatalytic activity test? A study with visible-light responsive titania. *Chemical Physics Letters* 429:606–610.

Yang, J., Dai, J., Chen, C.C. and Zhao, J.C. 2009. Effects of hydroxyl radicals and oxygen species on the 4-chlorophenol degradation by photoelectrocatalytic reactions with TiO_2-film electrodes. *Journal of Photochemistry and Photobiology A: Chemistry* 208: 66–77.

Yu, H.T., Quan, X., Zhang, Y.B., Ma, N., Chen, S. and Zhao H.M. 2008. Electrochemically assisted photocatalytic inactivation of *Escherichia coli* under visible light using a $ZnIn_2S_4$ film electrode. *Langmuir* 24: 7599–7604.

Yu, J.C., Yu, J.G., Ho, W.K., Jiang, Z.T. and Zhang, L.Z. 2002. Effects of F- doping on the photocatalytic activity and microstructures of nanocrystalline TiO_2 powders. *Chemcal Materials* 14: 3808–3816.

Yu, J.C., Ho, W., Yu, J.G.; Yip, H.Y., Wong, P.K. and Zhao, J.C. 2005. Efficient visible-light-induced photocatalytic disinfection on sulfur-doped nanocrystalline titania. *Environmental science & Technology* 39:1175–1179.

Yu, J.G., Xiong, J.F., Cheng, B., Yu, Y. and Wang J.B. 2005. Hydrothermal preparation and visible-light photocatalytic activity of Bi_2WO_6 powders. *Journal of Solid State Chemistry* 178:1968–1972.

Zang, L., Liu, C.Y. and Ren, X.M. 1995. Photochemistry of semiconductor particles 3. Effects of surface charge on reduction rate of methyl orange photosensitized by ZnS sols. *Journal of Photochemistry and Photobiology A: Chemistry* 85:239–245.

Zhang, C. and Zhu, Y.F. 2005. Synthesis of square Bi_2WO_6 nanoplates as high-activity visible-light-driven photocatalysts. *Chemical of Materials* 17:3537-3545.

Zhang, L.S., Li, J.L., Chen, Z.G., Tang, Y.W. and Yu, Y. 2006. Preparation of Fenton reagent with H_2O_2 generated by solar light-illuminated nano-Cu_2O/MWNTs composites. *Applied Catalysis A: General* 299: 292–297.

Zhang, L.S., Wang, W.Z., Chen, Z.G., Zhou, L., Xu, H.L. and Zhu, W. 2007. Fabrication of flower-like Bi_2WO_6 superstructures as high performance visible-light-driven photocatalysts. *Journal of Material Chemistry* 17:2526–2532.

Zhang, L.S., Wang, W.Z., Zhou, L. and Xu, H.L. 2007. Bi_2WO_6 Nano and

microstructures: Shape control and associated visible-light-driven photocatalytic activities. *Small* 3:1618– 1625.

Zhang, L.S., Wong, K.H., Chen, Z.G., Yu, J.C., Zhao, J.C., Hu, C., Chan, C.Y. and Wong, P.K. 2009. AgBr-Ag-Bi$_2$WO$_6$ nanojunction system: A novel and efficient photocatalyst with double visible-light active components. *Applied Catalysis A: General* 363:221–229.

Zhang, L.S., Wong, K.H., Zhang D.Q., Hu, C., Yu , J.C., Chan, C.Y. and Wong, P.K. 2009. Zn:In(OH)$_y$S$_z$ solid solution nanoplates: synthesis, characterization, and photocatalytic mechanism. *Environmental science & Technology* 43: 7883–7888.

Zhang, L.S., Wong, K.H., Yip, H.Y., Hu, C., Yu, J.C., Chan, C.Y. and Wong P.K. 2010. Effective photocatalytic disinfection of *E. coli* K-12 using AgBr-Ag-Bi$_2$WO$_6$ nanojunction system irradiated by visible light: The role of diffusing hydroxyl radicals. *Environmental science & Technology* 44: 1392–1398.

Zhang, L.Z., Djerdj, I., Cao, M.H. Antonietti, M. and Niederberger M. 2007. Nonaqueous sol–gel synthesis of a nanocrystalline InNbO$_4$ visible-light photocatalyst. *Advanced Materials* 19:2083–2086.

Zhang, M., Chen, C.C., Ma, W.H. and Zhao, J.C. 2008. Visible-light-induced aerobic oxidation of alcohols in a coupled photocatalytic system of dye-sensitized TiO$_2$ and TEMPO. *Angewandte Chemie International Edition* 47:9730–9733.

Zhao, J. and Yang, X. 2003. Photocatalytic oxidation for indoor air purification: A literature Review. *Building and Environment* 38: 645–654.

Zhao, X., Wu, Y., Yao, W.Q. and Zhu, Y.F. 2007. Photoelectrochemical properties of thin Bi$_2$WO$_6$ films. *Thin Solid Films* 515:753–4757.

Zhou, M. and He, J. 2007. Degradation of azo dye by three clean advanced oxidation processes: wet oxidation, electrochemical oxidation and wet electrochemical oxidation-a comparative study. *Electrochimica Acta* 53:1902–1910.

Zou, Z.G., Ye, J.H., Sayama, K. and Arakawa, H. 2001. Direct splitting of water under visible light irradiation with an oxide semiconductor photocatalyst. *Nature* 414: 625-627.